

Power scaling and mode quality of an acetylene mid-infrared hollow-core optical fiber gas laser

by

Hewa Walpitage Kushan Madushanka Weerasinghe

B.S., University of Colombo, 2011

AN ABSTRACT OF A DISSERTATION

submitted in partial fulfillment of the requirements for the degree

DOCTOR OF PHILOSOPHY

Department of Physics
College of Arts and Sciences

KANSAS STATE UNIVERSITY
Manhattan, Kansas

2019

Abstract

This thesis explores the power scalability and the mode quality of mid-IR acetylene filled Hollow-core Optical Fiber Gas LASer (HOFGLAS). The mid-IR lasing mechanism is based on the population inversion in acetylene molecules within the hollow-core of the hypocycloidal kagome structured fiber. The acetylene gas is optically pumped with 1 ns pulses near 1.5 μm using an optical parametric amplifier (OPA). The acetylene molecules absorb pump light via rotational-vibrational overtone transitions and can lase in 3 μm region through dipole allowed transitions. Since hollow-core fiber provides long interaction length and tight confinement for gas and light, higher gain is achieved by single pass configuration. In this work, the effect of fiber length, gas pressure, pump wavelength, and pump pulse duration on the mid-IR laser is experimentally studied in order to scale the laser system to higher mid-IR energies. By studying combinations of fiber length with different acetylene gas pressures, we were able to remove the laser signal saturations that have been observed in previous studies. Furthermore, the produced mid-IR laser energy linearly depends on the absorbed near-IR pump energy, and it is only limited by the available near-IR pump energy. Moreover, the highest mid-IR pulse energy of 2.56 μJ is measured when the acetylene filled HOFGLAS system is pumped via the P(9) line, which is the highest ever mid-IR pulse energy that has been measured to our knowledge. Mid-IR laser efficiency is independent of acetylene gas pressure and for the gas pressure region we worked on, a shorter pump pulse width is preferred. An experiment is designed and performed based on the M^2 to study the beam quality of the produced mid-IR beam. The mid-IR laser output shows near diffraction-limited performance with an M^2 value of 1.15. Finally, a numerical model based on the saturated absorption for inhomogeneous line profile is proposed to estimate the absorbed near-IR pump energy only by acetylene gas.

Power scaling and mode quality of an acetylene mid-infrared hollow-core optical fiber gas laser

by

Hewa Walpitage Kushan Madushanka Weerasinghe

B.S., University of Colombo, 2011

A DISSERTATION

submitted in partial fulfillment of the requirements for the degree

DOCTOR OF PHILOSOPHY

Department of Physics
College of Arts and Sciences

KANSAS STATE UNIVERSITY
Manhattan, Kansas

2019

Approved by:

Major Professor
Dr. Brian R. Washburn

Copyright

© Hewa Walpitage Kushan Weerasinghe 2019.

Abstract

This thesis explores the power scalability and the mode quality of mid-IR acetylene filled Hollow-core Optical Fiber Gas LASer (HOFGLAS). The mid-IR lasing mechanism is based on the population inversion in acetylene molecules within the hollow-core of the hypocycloidal kagome structured fiber. The acetylene gas is optically pumped with 1 ns pulses near 1.5 μm using an optical parametric amplifier (OPA). The acetylene molecules absorb pump light via rotational-vibrational overtone transitions and can lase in 3 μm region through dipole allowed transitions. Since hollow-core fiber provides long interaction length and tight confinement for gas and light, higher gain is achieved by single pass configuration. In this work, the effect of fiber length, gas pressure, pump wavelength, and pump pulse duration on the mid-IR laser is experimentally studied in order to scale the laser system to higher mid-IR energies. By studying combinations of fiber length with different acetylene gas pressures, we were able to remove the laser signal saturations that have been observed in previous studies. Furthermore, the produced mid-IR laser energy linearly depends on the absorbed near-IR pump energy, and it is only limited by the available near-IR pump energy. Moreover, the highest mid-IR pulse energy of 2.56 μJ is measured when the acetylene filled HOFGLAS system is pumped via the P(9) line, which is the highest ever mid-IR pulse energy that has been measured to our knowledge. Mid-IR laser efficiency is independent of acetylene gas pressure and for the gas pressure region we worked on, a shorter pump pulse width is preferred. An experiment is designed and performed based on the M^2 to study the beam quality of the produced mid-IR beam. The mid-IR laser output shows near diffraction-limited performance with an M^2 value of 1.15. Finally, a numerical model based on the saturated absorption for inhomogeneous line profile is proposed to estimate the absorbed near-IR pump energy only by acetylene gas.

Table of Contents

List of Figures	ix
List of Tables	xviii
Acknowledgments.....	xix
Dedication	xxi
Chapter 1 - Introduction.....	1
1.1 A review of different HOFGLAS system	4
1.2 Importance of this thesis	11
1.3 Thesis outline	12
Chapter 2 - The acetylene ($^{12}\text{C}_2\text{H}_2$) filled HOFGLAS system.....	14
2.3 The optical parametric amplifier for acetylene HOFGLAS system	27
2.4 Experimental setup of acetylene filled HOFGLAS system	30
Chapter 3 - Power scaling of the acetylene filled HOFGLAS system.....	32
3.1 Laser signal saturation in previous acetylene filled HOFGLAS system	32
3.2 Effect of fiber length.....	36
3.2.1 Quantitative study of laser optical properties	38
3.3 Effect of the pump wavelength.....	52
3.3.1 Experimental results and discussion	53
3.4 Effect of pump pulse duration on laser performance.....	59
Chapter 4 - Mode quality of acetylene filled HOFGLAS system.....	63
4.1 Free space propagation modes	64
4.1.2 Higher-order propagation modes in Cartesian coordinates	67
4.2 Guided modes in step-index and hollow fibers	71

4.2.1 Guided modes in a step-index fiber	71
4.2.2 Guided modes in kagome structured HCPCF	75
4.3 M^2 measurement	76
4.3.1 M^2 for Corning SMF28 fiber.....	78
4.3.2 M^2 measurement for mid-IR output beam of acetylene filled HOFGLS system.....	81
Chapter 5 - Saturated absorption in acetylene	85
5.1 Linear and nonlinear absorption	86
5.1.1 Absorption line profile.....	87
5.1.2 Saturation in population difference and absorption by optical pumping.....	91
5.1.3 Saturation and power broadening of homogeneous line profile	95
5.1.4 Saturation of the inhomogeneous line profile	97
5.2 Numerical model to estimate the pump absorbed energy by gas for the HOFGLAS system	102
5.2.1 Saturation power for acetylene $\nu_1 + \nu_3$ absorption band.....	104
5.2.2 Numerical calculation to estimate the absorbed energy by gas	107
Chapter 6 - New near-IR pump source	118
6.1 Optical parametric amplification	118
6.2 Two-stage OPA.....	128
6.2.1 Phase matching condition of bulk KTP crystal for near-IR OPA operation.....	131
6.2.2 Numerical calculation to predict the gain of two-stage OPA	134
6.2.3 Experimental setup of two stage near-IR OPA.....	135
6.2.4 The alignment procedure and preliminary results of two stage OPA	137
Chapter 7 - Summary and outlook	139

7.1 Summary	139
7.2 Outlook	140
References	144
Appendix A - Abbreviations	153
Appendix B - Python codes	155
B.1 Python code to check the validity of saturation power of 23 mW for acetylene	155
B.2 Python code to calculate absorbed near-IR pump power by acetylene gas in CW HOFGLAS system	159
B.3 Python code to calculate absorbed near-IR energy by acetylene gas in HOFGLAS system	163
B.4 Python code to calculate phase matching angles for KTP crystal	168
Appendix C - Copyright permissions	170
C.1 From The Optical Society	170
C.2 From the AAAS	173
C.3 From the SPIE	174

List of Figures

Figure 1.1 Main components of a HOFGLAS system. An optical pump source, a hollow-core photonic crystal fiber (HC-PCF) and molecular gas.....	4
Figure 1.2 The modulated, amplified, tunable pump diode setup of the Ref. [23]. PMF: Polarization-maintaining fiber; FPC: Fiber polarization controller; SOA: Semiconductor optical amplifier; WDM: Wavelength division multiplexer; LD: Laser diode. Adapted with permission from Ref. [23],[The Optical Society].	6
Figure 1.3 Experimental setup for Ref. [26]. Ring cavity geometry is formed by adding feedback fiber into the system. Adapted with permission Ref. [26],[The Optical Society].....	8
Figure 2.1 The normal modes of acetylene, $^{12}\text{C}_2\text{H}_2$. The relative motions of each atom are indicated by the black arrows (not to scale). The respective vibrational frequencies are shown at upper-middle of each normal mode.....	16
Figure 2.2 Absorption spectrum of acetylene ($^{12}\text{C}_2\text{H}_2$) molecules assuming molecules are in a 5 cm long cell with the gas pressure of 50 torr. This absorption spectrum shows the R and P-branch transition between the vibrational ground state and $\nu_1 + \nu_3$ vibrational manifold. Absorption spectrum was obtained with Spectralcalc simulations [37].	19
Figure 2.3 A simplified energy level diagram of acetylene P(13) transition. When acetylene molecules are pumped via P(13) line, they can make transitions from rotational state $J=13$ of the vibrational ground state to rotational state $J=12$ of the $\nu_1 + \nu_3$ vibrational manifold. The excited molecules can make radiative transitions from $J=12$ rotational state of the $\nu_1 + \nu_3$ vibrational manifold to $J=13$ or $J=11$ rotational states in the ν_1 vibrational manifold. These radiative transitions are labeled as P(13) and R(11) and have wavelengths of $3.16 \mu\text{m}$ and $3.12 \mu\text{m}$ respectively.....	20

Figure 2.4 In a conventional solid-core fiber, light is confined to the core due to total internal reflection (TIR). The core has a slightly higher refractive index (n_2) than the cladding (n_1). This enables condition for TIR. 22

Figure 2.5 The photonic band gap (PBG) guidance supported by (a) frustrated tunneling, (b) Bragg condition. Reproduced with permission from Ref. [40]. 23

Figure 2.6 The cross-sectional view obtained with a scanning electron microscope of (a) 19-cell defect kagome-structured HC-PCF with a core diameter of $\sim 48 \mu\text{m}$ and pitch of $12 \mu\text{m}$ (b) 1-cell defect kagome-structured HC-PCF with a core diameter of $15 \mu\text{m}$ and pitch of $5 \mu\text{m}$. Figure (a) reprinted with permission from Ref. [48], [The Optical Society]. Figure (b) Reprinted with permission from Ref.[45], [AAAS]. 24

Figure 2.7 Scanning electron microscopic images of 7-cell defect core and three-ring kagome cladding HC-PCF with (a) conventional circular core and (b) a hypocycloid core. Reprinted with permission from Ref. [55], [The Optical Society]. 25

Figure 2.8 Hypocycloidal kagome-structured HC-PCF with 7-cell defect, 3-ring kagome cladding, a core diameter of $60/72 \mu\text{m}$ (a) cross section and (b) near-IR loss spectrum. Both the picture of the cross-section and loss spectrum data are provided by Ref. [59]..... 27

Figure 2.9 A schematic of the optical parametric amplifier (OPA). A 5 cm long MgO doped PPLN crystal is used to mix the pump and signal beams. I_1 is a free space faraday isolator and I_2 is fiber coupled isolator. PC- paddle polarizer controllers. DM- Long wavelength pass dichroic mirror. PBS- polarizing beam splitter. PM EDFA- Polarization maintain Erbium doped fiber amplifier. 28

Figure 2.10 A simple schematic of the OPA pumped acetylene HOFGLAS system. All the optics in the input end are made with BK7, and all the optics in the output end are made with CaF2.

The length of the HC-PCF is 7.6 m. HWP- Half wave plate, PBS – Polarizing beam splitter, M – silver mirrors, DM- dichroic mirror, FM- silver mirrors on flipper mount, L1 – BK7 lens with focal length $f = 7.5$ cm, L2 – CaF₂ lens with focal length $f = 15$ cm, P_{in}- input near-IR OPA pump pulse energy, P_{laser} – Produced mid-IR pulse energy. Adapted with permission from Ref. [64], [SPIE]. 31

Figure 3.1 The measured mid-IR pulse energy at different acetylene gas pressures as a function of absorbed near-IR pump pulse energy for an 1.46 m long kagome-structured HC-PCF with the core diameter of 85-94 μm . Adapted from Ref. [60]...... 33

Figure 3.2 The measured mid-IR pulse energy at different acetylene gas pressures as a function of absorbed near-IR pump pulse energy by acetylene molecules for an 11 m long hypocycloidal kagome-structured HC-PCF with the core diameter of 60-72 μm . Adapted from Ref. [65].35

Figure 3.3 The measured mid-IR pulse energy at different acetylene gas pressures as a function of coupled near-IR pump pulse energy for an 11 m long hypocycloidal kagome-structured HC-PCF with the core diameter of 60-72 μm . Adapted from Ref. [65]...... 36

Figure 3.4 Simplified ro-vibrational energy level diagram of acetylene. The lasing wavelengths 3.11 μm and 3.17 μm correspond to the R(11) and P(13) transitions when pumped via P(13) line..... 39

Figure 3.5 Simplified experimental setup of acetylene filled HOFGLAS system showing where the near-IR pump energies and produced mid-IR energies are measured. E_{Pin} and E_{Pout} are the incident and transmitted pump pulse energies measured with pyroelectric energy meter. E_{Lout} is the measured mid-IR pulse energy using the same energy meter. L1 is an AR coated BK7 plano-convex lens with a focal length of 7.5 cm and L2 is a CaF₂ plano-convex lens with a focal length of 15 cm. FM 1 and FM 2 are flipper mounts which are used to direct the beam

towards the energy meter head. A 5mm thick germanium filter is used to filter out the produced mid-IR energy from the residue pump energy. 40

Figure 3.6 A simple schematic of the experimental setup that is used to verify the on-resonance condition of OPA signal wavelength with P(13) absorption line of acetylene. FC is a 99:1 fiber coupler and PD is a large area photodiode. 42

Figure 3.7 Produced mid-IR pulse energy as a function of coupled near-IR pump pulse energy into the fiber with coupling lens of focal length $f = 7.5$ cm. The portion of near-IR pump pulse energy lost due to the fiber guidance also included in the coupled near-IR pump pulse energy. Each pulse energy is obtained averaging over 500 pulses, and error bars indicate the standard deviation of each individual measurements. Acetylene molecules are pumped via P(13) absorption line. 43

Figure 3.8 The summary of two calculation routes to estimate the near-IR pump pulse energy only by acetylene gas. The blue, red and green text stand for estimated values using measured data and the black color quantities are experimentally measured values. The average value between two routes is taken, to estimate the absorbed near-IR pump pulse energy only by acetylene gas. 47

Figure 3.9 Mid-IR laser output energy as a function of estimated absorbed pump pulse energy only by acetylene molecules at a given pressure. Acetylene molecules are excited via P(13) absorption line. Each pulse energy is obtained averaging over 500 pulses, and error bars indicate the standard deviation of each individual measurements. 48

Figure 3.10 Maximum mid-IR pulse energy (a) and absorbed maximum near-IR pump pulse energy only by acetylene gas (b) as a function of acetylene gas pressure inside the fiber.

Acetylene molecules are pumped with P(13) absorption line. Maximum coupled near-IR pump pulse energy $\sim 12.5 \mu\text{J}$	49
Figure 3.11 Laser's optical-to-optical conversion efficiency as a function of acetylene gas pressure inside the fiber. Acetylene molecules are excited via P(13) absorption line.	51
Figure 3.12 Simplified ro-vibrational energy level diagram of acetylene. The lasing wavelengths $3.12 \mu\text{m}$ and $3.16 \mu\text{m}$ correspond to the R(7) and P(9) transitions when pumped via P(9) line.	54
Figure 3.13 Produced mid-IR pulse energy as a function of coupled near-IR pump pulse energy into the fiber with coupling lens of focal length $f = 7.5 \text{ cm}$. The portion of near-IR pump pulse energy lost due to the fiber guidance also included in the coupled near-IR pump pulse energy. Each pulse energy is obtained averaging over 500 pulses, and error bars indicate the standard deviation of each individual measurements. Acetylene molecules are pumped via P(9) absorption line.....	55
Figure 3.14 Mid-IR laser output energy as a function of estimated absorbed pump pulse energy only by acetylene molecules at a given pressure. Acetylene molecules are excited via P(9) absorption line. Each pulse energy is obtained averaging over 500 pulses, and error bars indicate the standard deviation of each individual measurements.....	56
Figure 3.15 Maximum mid-IR pulse energy (a) and absorbed maximum near-IR pump pulse energy only by acetylene gas (b) as a function of acetylene gas pressure inside the fiber. Acetylene molecules are pumped with P(9) absorption line. Maximum coupled near-IR pump pulse energy $\sim 13 \mu\text{J}$	57
Figure 3.16 Laser's optical-to-optical conversion efficiency as a function of acetylene gas pressure inside the fiber. Acetylene molecules are pumped at P(9) absorption line.....	58

Figure 3.17 The optical-to-optical conversion efficiency as a function of gas pressure compared for an OPA pumped acetylene filled HOFGLAS system with the pump pulse duration of 1 ns and a diode-pumped HOFGLAS system with the pump pulse duration of 20 ns.....	59
Figure 3.18 The calculated mean free paths for pressure region 0.1 torr to 14 torr as a function of acetylene gas pressure. Inset shows the calculated mean free paths for acetylene pressure form 1 torr to 14 torr.	60
Figure 3.19 The calculated mean intermolecular collisional time as a function of acetylene gas pressures. Inset zoomed in to the pressure region of 1-14 torr.	62
Figure 4.1 Divergence of lowest order Gaussian beam.	66
Figure 4.2 Rayleigh range of a Gaussian beam.	67
Figure 4.3 Transverse mode patterns for free space propagating Hermite-Gaussian modes. Numerically generated using a Python code.....	69
Figure 4.4 Transverse mode patterns of Laguerre-Gaussian modes. Numerically generated using a Python code.....	70
Figure 4.5 The geometry of a step-index fiber. Here the geometry of commercial SMF28 fiber is considered, which has core radius $a = 4.5 \mu\text{m}$ with a refractive index $n_1 = 1.466$ at wavelength 1550 nm. Cladding radius of $62.5 \mu\text{m}$ with a refractive index of 1.45 at the same wavelength.	72
Figure 4.6 Intensity distribution of a few LP modes in step-index fiber. Numerically obtained using a Python code.	74
Figure 4.7 Simple schematic of the experimental setup that used to obtain the beam profiles of light coming out from a SMF28 fiber.	79
Figure 4.8 A beam profile of the beam coming out from a single-mode fiber.	79

Figure 4.9 The beam width of the SMF 28 output measured using 60 μm slit.	80
Figure 4.10 A series of beam profile obtained at the highest mid-IR laser output energy. A fixed 20 μm slit is used to scan across the beam.....	82
Figure 4.11 Experimentally determined beam width as a function of axial position. The laser is worked at the highest output energy. Error bars stand for fluctuations in the averages of 50 pulses.....	83
Figure 4.12 Measured M^2 values as a function of produced mid-IR pulse energy. The acetylene gas pressure inside the fiber was kept at 10 torr when measuring each data point.....	84
Figure 5.1 Laser with initial power P_0 travel through an absorbing medium with length Z	86
Figure 5.2 Absorption coefficient α as a function of frequency ω near to center frequency ω_0 .	88
Figure 5.3 Voigt profile as a convolution of Lorentzian line shape with Gaussian profile.	90
Figure 5.4 Additional broadening and shift of a Lorentzian line profile due to pressure and collisions.	91
Figure 5.5 Two-level system with no relaxation mechanism to other levels.....	91
Figure 5.6 Saturation of absorption coefficient α and population density of level one as a function of saturation parameter S	95
Figure 5.7 Broadening of homogeneous line profile due to saturation or power.	97
Figure 5.8 The Bennet hole and Bennet peak in the lower and upper state population densities.	99
Figure 5.9 Simplified experimental configuration to determine the peak absorbance. A 6.35 m long HC-PBG fiber is coiled with 6 cm diameter and both ends are inside a vacuum chamber. W1 and W2 are 1 mm thick sapphire windows. $\lambda/4$ is a quarter wave plate and $\lambda/2$ is a half wave plate. PBS is a polarizing beam splitter. The EDFA is seeded with extended cavity diode laser	

and EDFA operated at 60 mW output power. PD is $5 \times 5 \text{ mm}^2$ Ge photo diode and two 6 mm convex lens are used couple in/out the light to/from fiber.....	105
Figure 5.10 Peak Optical depth (top) for the 6.35 m fiber filled with 10 Pa acetylene and saturation power (bottom) as a function of off-resonance transmitted power. (Reproduced with permission from Ref [89], [The Optical Society].).....	107
Figure 5.11 Calculated optical depth by solving Eq. 5.42 numerically for the 6.35 m long fiber filled with 10 Pa (0.075 torr) acetylene gas as a function of input power.	109
Figure 5.12 EDFA spectrum measured when output power is at 9.6 W. Approximately 50% of the total output power lies within a 3 nm bandwidth around the seed wavelength. (Reproduced with permission from Ref [28],[The Optical Society])......	111
Figure 5.13 Comparison between numerical results and experimental results for absorbed power by acetylene gas as a function of coupled power (a) for gas pressure of 0.6 mbar (b) for gas pressure of 4.23 mbar.....	112
Figure 5.14 Comparison between numerical result and the experimental result of absorbed power by acetylene gas as a function of gas pressure. Input (coupled) power to the system is 4.3 W for all the data points.....	113
Figure 5.15 Comparison between numerical result and the experimental result of absorbed energy only by acetylene gas as a function of gas pressure for pulsed acetylene HOFGLAS system with fiber length 10.9 m. Coupled pulse energy to the system is $\sim 7.5 \mu\text{J}$ for all the data points.	115
Figure 5.16 Comparison between numerical result and the experimental result of absorbed energy only by acetylene gas as a function of gas pressure for pulsed acetylene HOFGLAS system	

with fiber length 10.9 m. Here numerical results were obtained by scaling the saturation power by factor of 25. Coupled pulse energy to the system is $\sim 7.5 \mu\text{J}$ for all the data points. 116

Figure 6.1 Schematic of various frequency conversion processes involving the second-order nonlinear process. 119

Figure 6.2 Optical parametric amplification. The interaction beams 120

Figure 6.3 Parametric gain for different phase matching conditions as a function of normalized propagation distance along the nonlinear crystal. This is numerically generated using solutions available in Ref. [93]. 121

Figure 6.4 Wave propagation in biaxial crystal's coordinate system. 126

Figure 6.5 A schematic of a periodically poled material with the orientation of crystalline axes changes between each segment. 128

Figure 6.6 The schematic of the tunable, high-power near-IR two stage OPA using two KTP crystals. Adapted from Ref. [100]. 130

Figure 6.7 Input and output intensities from SNLO calculation for signal beam (top) and pump beam (bottom). The pump beam is depleted, and signal beam is amplified. 135

Figure 6.8 A simple schematic of the two-stage OPA. The existing OPA is used as the pre-amplifier in the first stage of the OPA and the bulk 2.5 cm long KTP crystal is used in the second stage as the power-amplifier. 136

Figure 6.9 Alignment of KTP crystal respect to the laser beams. Rotate around B-axis to match polarizations and rotate around A-axis to achieve phase matching angles. 137

List of Tables

Table 2.1 Fundamental frequencies for all normal modes of acetylene ($^{12}\text{C}_2\text{H}_2$).....	17
Table 6.1 Various polarization combination for type I and type II phase matching.	123

Acknowledgments

I would like to thank my advisor Professor Brian Washburn, for his guidance and support throughout the past six years. He is one of the best teachers I have ever met, who constantly inspires me to learn novel concepts in the field. He always has time to listen to our good and bad stories in the lab, despite of busy schedule. His patience, motivation, and advices encouraged me to pursue my graduate research well at Kansas State University. I also thank Professor Kristan Corwin for her helpful advices and insightful discussions on every part of this thesis. She is one of the nicest and kindest people I have ever met. I would like to acknowledge my supervisory committee members as well: Professor Daniel Rolles, Professor Shuting Lei, and Professor Stacey Kulesza.

I would like to thank Dr. Fetah Benabid for providing the hollow-core photonic crystal fibers which are essential for this work. I also thank Professor Wolfgang Rudolph and Dr. Vasudevan Nampoothiri from University of New Mexico for their useful tips and discussions.

I would like to thank Professor Micheal O'Shea for advising me for the first two years in grad school. Also, I thank all the James R. Macdonald Laboratory staff, especially Chris Aikens and Justin Millette. And, I would like to thank Dr. Kanaka Raju Pandiri and Dr. Adam Summers for giving me useful experimental tips.

I would like to acknowledge my past and current lab mates, especially Dr. Neda Dadashzadeh for teaching me how to use the experimental setup, Dr. Manasadevi Thirugnanasambandam for helpful discussions and numerous supports in the lab, Sajed Hosseini-Zavareh and Lindsay Hutcherson for giving me moral support and much needed social interaction.

Finally, I would like to thank my family and friends for all of their love, help and encouragement, especially my wife Dimuthu and my daughter Nuvee.

This work was supported by the Air Force Office of Scientific Research (FA9550-14-1-0024) and Air Force Research Laboratory (FA9451-17-2-0011).

Dedication

This thesis is dedicated to my mother (Piyasili Dias), my father (Panasiri Weerasinghe), my two brothers (Sahan and Heshan), and my in-laws (Lalitha and Weerawardana) who have always provided me encouragement and support throughout my life. Finally, to my loving wife Dimuthu for her everlasting love and support, to my lovely daughter Nuvee, whose smiling face always gives me joy.

Chapter 1 - Introduction

Lasers that operate in the mid-IR wavelength region from 2 to 10 μm have recently gained much attention due to their potential applications in spectroscopy, medical, and free space communication. The strong rotational-vibrational transitions of many important molecules like H_2O , CO_2 , CH_4 , CO , and NO_2 lie in the mid-IR region. These transitions are usually few orders of magnitude stronger than the transitions that lie in the near-IR or visible regions. Therefore, a mid-IR laser source provides a path to detect the trace gases, greenhouse gases and medically important gases [1]. Furthermore, the mid-IR spectral region has two high atmospheric transmission windows at 3-5 μm and 8-13 μm , making mid-IR laser source to be an ideal candidate to use in applications like free space communications, and range finding [2]. Moreover, biomolecules like proteins, amides, and lipids have strong vibrational transitions in the mid-IR region. Due to this mid-IR lasers have been used in many biomedical applications [3]. Also, the spectral peaks of the thermal emissions associated with most biological and mechanical objects with temperatures between 200 K and 1400 K lie in the mid-IR region. Therefore, mid-IR laser sources have potential applications in security and defense which require thermal imaging and night vision techniques [4]. Due to these interesting applications, extensive researches have been done to develop new laser sources in the mid-IR region.

The gain medium of common mid-IR lasers are either a gas, a semiconductor structure or a rare-earth doped dielectric. Quantum cascade lasers (QCLs), which are based on semiconductor structures, have gained a lot of interest as the promising mid-IR laser sources over the past decades. The lasing mechanism of QCL is based on the propagation of electrons through the multiple quantum wells. Multiple layers of semiconductor materials like GaAs and InP are stacked to form quantum well heterostructures, and center wavelength and the tuning capability of the QCL varies

with the material type and the layer thickness [5, 6]. QCLs have demonstrated broader spectral coverage from 3-25 μm region with the potential for large tunability [7]. Furthermore, multi-Watt output power, continuous wave (CW) mid-IR lasing by QCLs is observed with wall-plug efficiencies up to 21% at room temperature. QCLs have been successfully used in applications like environmental monitoring, security and biomedical sensing [8]. Even though single frequency and relatively high-power QCLs are commercially available, cryogenical cooling is necessary to achieve narrow bandwidth laser operation which is essential for spectroscopic applications. Also, they tend to have multimode beam quality at high output powers [9].

In the past decade mid-IR fiber lasers have gained much attention among researchers and in contrast to QCLs they offer attractive features like compactness, near-diffraction-limited beam quality, high efficiency, and convenient heat management. The gain medium of mid-IR laser usually consists with a rare-earth-ion-doped fiber and these rare earth ions are doped to the fibers that are made with fluoride glasses [10, 11]. Even though rare-earth-ion-doped silica glass fibers are used in near-IR fiber lasers, they cannot be used in the mid-IR region due to silica glass absorbs light above 2 μm region. The lasing mechanism of the aforementioned rare-earth-ion-doped mid-IR fiber lasers depends on the electronic transitions between the stark shifted energy levels of the doped ions. These ion-doped fibers are usually pumped with diode lasers at the IR region. Recently, mid-IR lasing at 3.4 μm is observed with 38.6% efficiency from erbium doped fluoride fiber [10]. Moreover, a holmium-doped fluoride fiber laser demonstrated mid-IR lasing at 3.9 μm when pumped with 888 nm diode laser [12]. Particularly, with rare-earth ions doped into ZBLAN ($\text{ZrF}_4\text{-BaF}_2\text{-LaF}_3\text{-AlF}_3\text{-NaF}$) fibers show mid-IR lasing close to 4 μm . The mid-IR output power of 24 W at 3 μm was demonstrated by Tokita *et al.* by using an erbium-doped ZBLAN fiber with an optical-optical conversion efficiency of 14.5% [11]. Also, a tunable mid-IR erbium-doped

ZBLAN fiber laser is demonstrated a near diffraction limited mid-IR output beam with a power of 1.4 W [13]. The mid-IR laser output power of 2.5 W at 2.94 μm is obtained with a slope efficiency of 32% by pumping ZBLAN fiber which is co-doped with Ho^{3+} and Pr^{3+} ions [14]. Even though these fiber lasers are commercially available nowadays, they have practical limitations due to fragileness, unnecessary nonlinear effects at higher powers and low damage thresholds.

On the other hand, traditional molecular gas lasers offer high damage threshold values, which is an essential feature to achieve MW level powers. More importantly, optically pumped gas lasers have demonstrated mid-IR lasing with molecular gases like CO_2 , CO , HCN , C_2H_2 , and HBr . Lasing at 10.6 μm was observed with an optically pumped CO_2 laser as early as the 1970s [15]. Mid-IR lasing near 4.6 μm is observed with CO laser when CO molecules are optically pumped via rotational-vibrational overtone transitions at 2.3 μm [16, 17]. Millijoule level of mid-IR pulse energy at 4 μm is obtained by exciting HBr molecules through first-order rotational-vibrational overtone transition at 2 μm , and overall conversion efficiency of 24% is achieved [18]. Furthermore, mid-IR lasing at 3 μm with HCN and C_2H_2 are also demonstrated by pumping the molecules with nanosecond pulses from an optical parametric oscillator (OPO) [19]. Even though optically pumped gas lasers inherently offer higher damage thresholds, relatively large gain-coefficient, and easy thermal managing options, they have limited use due to some practical drawbacks. Traditional gas lasers usually have shorter interaction lengths, and longer gas cells are needed to achieve higher power levels. This makes them bulky, cumbersome and fragile for field applications.

With the advent of hollow-core photonic crystal fibers (HC-PCF) a new class of laser is introduced by Jones *et al.* in 2011 by confining gas molecules and light inside the core of a kagome structured HC-PCF[20]. This laser type is named as Hollow-core Optically Pumped Fiber Gas

LASer (HOFGLAS), and several HOFGLAS systems have emerged up to now. This new type of laser system can have advantages of both fiber lasers and gas lasers. More importantly, since the light is guided in hollow-core of the fiber, estimated damage thresholds and threshold values for undesired nonlinear processes are higher than the solid core fibers [19, 21]. Also, by properly selecting suitable HC-PCFs with atomic or molecular gases and proper pump sources HOFGLAS systems have the potential to deliver a wide range of emission wavelengths spanning from ultraviolet (UV) to IR. As shown in Fig. 1.1, most of the HOFGLAS systems have three main components, an optical pump source, a hollow-core photonic crystal fiber, and molecular gas.

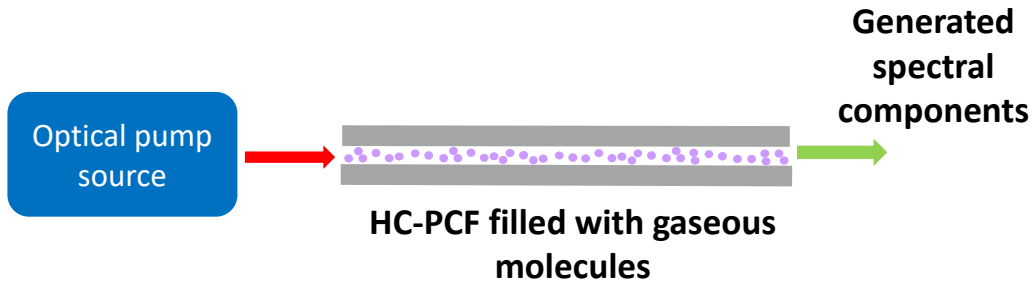


Figure 1.1 Main components of a HOFGLAS system. An optical pump source, a hollow-core photonic crystal fiber (HC-PCF) and molecular gas.

1.1 A review of different HOFGLAS system

The first mid-IR HOFGLAS system was filled with acetylene gas ($^{12}\text{C}_2\text{H}_2$), and kagome structured HC-PCF was used as the waveguide [20]. The acetylene gas was pumped with 5 ns pulses at $1.52\ \mu\text{m}$, and OPO was used as the pump source. The pump wavelength was overlapped with the acetylene's R(7) ro-vibrational overtone transition and two mid-IR lasing transitions at $3.123\ \mu\text{m}$, and $3.162\ \mu\text{m}$ were observed. The maximum mid-IR laser pulse energy of 6 nJ was measured at the gas pressure of 7 torr. Only a few percents of laser conversion efficiency was achieved due to

higher fiber loss of 20 dB/m at lasing wavelength and the broader linewidth (~ 2 GHz) of the pump source.

After the first mid-IR HOFGLAS demonstration, improved mid-IR laser performance was reported using an OPA pumped acetylene filled HOFGLAS system [22]. There 1 ns pulses at 1.53 μm from an OPA was used as the pump source. Also, fiber loss at lasing wavelength was improved to 5 dB/m by optimizing the fiber structure. Here, acetylene molecules which were confined in the hollow-core of the 1.46 m long kagome-structured HC-PCF were excited along the P(13) ro-vibrational overtone transition using the OPA pulses at 1.53 μm . Two mid-IR lasing wavelengths at 3.114 μm and 3.172 μm were observed. More importantly, the mid-IR laser efficiency of 20% was obtained thanks to lower fiber losses and narrow linewidth (~ 440 MHz) pump source. The maximum mid-IR laser pulse energy of 0.56 μJ was measured with the acetylene gas pressure of 2 torr. Furthermore, mid-IR lasing by HCN molecules was demonstrated by using the same experimental setup. For that, HCN molecules inside of a 45 cm long kagome structured HC-PCF were pumped at P(10) ro-vibrational overtone transition at 1.541 μm . The same aforementioned OPA system was used as the pump source, and mid-IR lasing at 3.092 μm and 3.146 μm were observed.

Wang *et al.* demonstrated mid-IR lasing by acetylene filled HOFGLAS system with a power conversion efficiency of 30%, with respect to absorbed pump power by acetylene gas [23]. There, a 10.5 m long low loss antiresonant HC-PCF was used as the waveguide and amplified, modulated, narrowband, tunable diode laser at 1.5 μm was used as the pump source. Figure 1.2 shows the schematic of the near-IR pump source. First, the output from the tunable diode laser was modulated using two Mach-Zehnder intensity modulators and semiconductor optical amplifier. Then two-staged erbium-doped fiber amplifiers were used to amplify the modulated light. Finally,

the pump source was operated with 10 kHz modulation frequency and pulse duration of 20 ns. The estimated linewidth of the pump source was < 100 MHz. The mid-IR lasing at $3.12 \mu\text{m}$ and $3.16 \mu\text{m}$ were observed when the acetylene molecules were pumped via the P(9) ro-vibrational overtone transition and this transitions corresponds to the pump wavelength of 1530.37 nm . The maximum mid-IR laser pulse energy of $0.8 \mu\text{J}$ was measured with acetylene gas pressure of 0.52 torr (0.7 mbar). Even though this HOFGLAS system demonstrated 30% optical-optical conversion efficiency; the conversion efficiency was degraded with increasing acetylene gas pressure.

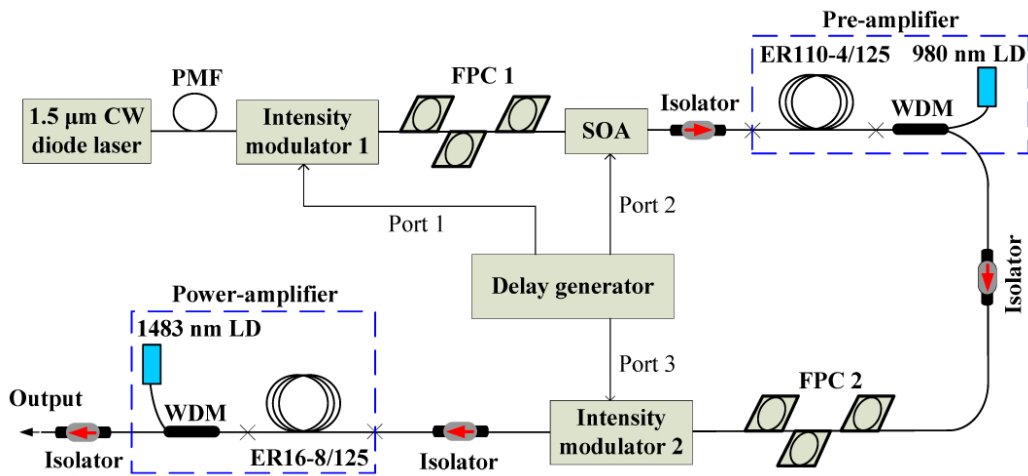


Figure 1.2 The modulated, amplified, tunable pump diode setup of the Ref. [23]. PMF: Polarization-maintaining fiber; FPC: Fiber polarization controller; SOA: Semiconductor optical amplifier; WDM: Wavelength division multiplexer; LD: Laser diode. Adapted with permission from Ref. [23],[The Optical Society].

The first CW lasing HOFGLAS system was demonstrated by Nampoothiri *et al.* by using molecular iodine inside the hollow-core of a hypocycloidal kagome structured HC-PCF [24]. The lasing in the $1280\text{-}1340 \text{ nm}$ region was observed when iodine was optically pumped at 532 nm . Here, cavity mirrors were used to get enough gain required for CW lasing. The maximum near-IR output power of 8 mW was measured with 250 mW of input pump power. The maximum optical-

to-optical conversion efficiency was only about 4% mainly due to the high fiber loss (42 dB/m) at the pump wavelength. Furthermore, CW lasing at visible wavelengths using an I₂ filled HOFGLAS system by the same author [25]. Here, a 20 cm long lower loss hypocycloidal kagome structured HC-PCF is used in the setup with I₂ vapor pressure of 300 mtorr. The HC-PCF has loss of 0.35 dB/m at the pump wavelength (532 nm) and loss of ~ 0.55 dB/m at lasing wavelengths (576-605 nm). The experimental setup was identical to that of in Ref. [24] except the HC-PCF and the cavity mirrors. The I₂ vapors were pumped with 80 mW of CW power at 532 nm, and three laser lines at 576.6 nm, 590.3 nm and 605 nm were observed with 7 mW of combined power and the conversion efficiency of 11%.

Hassan *et al.* demonstrated the first CW mid-IR HOFGLAS system by adding feedback fiber to the acetylene filled HOFGLAS system [26]. The experimental setup was based on two HC-PCFs. A 10 m HC-PCF was used to contain the light and the acetylene gas. The second fiber was used as the feedback fiber (3 m for CW operation and 100 m for pulsed operation) with a ring cavity geometry as shown in Fig. 1.3. Acetylene molecules were pumped with the CW laser light from the tunable diode laser, and diode laser was tuned to be on-resonance with one of the strong absorption lines of acetylene around 1530 nm. The pump beam and feedback beam were combined using a dichroic mirror and uncoated CaF₂ window, or a coated custom-made component was used as the output coupler, and these provide 7% and 70% output coupling efficiencies respectively.

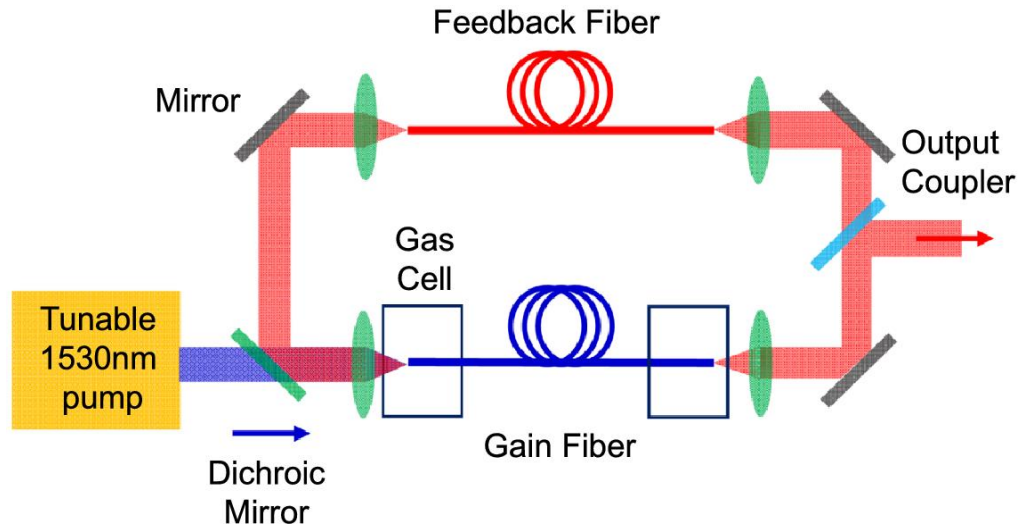


Figure 1.3 Experimental setup for Ref. [26]. Ring cavity geometry is formed by adding feedback fiber into the system. Adapted with permission Ref. [26],[The Optical Society].

By pumping along the P(9) transition, authors were able to obtain CW lasing at 3.1 μm with the threshold pump power of 34 mW and slope efficiency of 6.7% with 70% of output coupling. Also, no saturation in output power was observed up to maximum available pump power (75 mW). Furthermore, threshold pump power was reduced to 16 mW by using 7% output coupler, and maximum mid-IR power of 2.5 mW was observed with acetylene gas pressure 0.22 torr. Pulsed mid-IR lasing was also demonstrated by modulating the pump into a train of 80 ns pulses and replacing the feedback fiber with a 100 m long fiber.

The output beam quality of an acetylene-filled mid-IR HOFGLAS system was investigated for the first time by Dadashzadeh *et al.* by performing an M^2 measurement [27]. The laser output was near-diffraction limited with $M^2 = 1.15$. Same acetylene filled HOFGLAS setup as in Ref. [22] was used but with different HC-PCF. A low loss 11 m long hypocycloidal kagome structured fiber was used in the setup and fiber loss was measured to be 0.08 dB/m at the pump wavelength and 1.13 dB/m at the mid-IR lasing wavelength. The maximum mid-IR pulse energy of 1.4 μJ was measured with acetylene gas pressure of 9.8 torr, and the highest slope efficiency of 17% was

obtained. More importantly, unlike in Ref. [20] laser signal saturation have not seen in this work, and this behavior is encouraging for further power scaling of such a system.

Following the work done by Hassan *et al.* [26], 1 W output power at mid-IR was demonstrated with a CW acetylene filled HOFGLAS system by Xu *et al.* in 2017 [28]. There, a custom made high-power EDFA (10 W) seeded with a diode laser was used as the pump source. Authors have demonstrated a maximum of 1.12 W output power at 3 μm with 33% of optical-to-optical conversion efficiency by pumping the acetylene molecules along the P(9) transition near 1.53 μm . And the acetylene molecules were inside of a 15 m long anti-resonant HC-PCF at a gas pressure of 0.45 torr. More importantly, this mid-IR laser was based on a single-pass configuration, and a no laser signal saturation was observed. The design of this system provides a way to achieve a compact high-power mid-IR HOFGLAS system.

High-power tunable mid-IR acetylene filled HOFGLAS system was reported by Zhou *et al.* in 2018 [29]. There, both CW and pulsed step-tunable mid-IR laser output were observed in the range of 3.09-3.21 μm . A maximum CW laser output power of 0.77 W was observed with 13% optical-to-optical conversion efficiency, and a maximum output pulse energy of 0.6 μJ was observed for pulsed operation with 16% conversion efficiency. A high-power EDFA seeded with tunable CW laser at 1.5 μm was used as the pump source for the CW mid-IR laser operation. For the pulsed mid-IR laser operation, the output from the CW tunable laser at 1.5 μm was modulated using an acousto-optic-modulator (AOM) and amplified by the high power EDFA to use as the pump source. In both CW and pulsed mid-IR laser operation, a 10 m anti-resonant HC-PCF was used with acetylene gas pressures of 0.67 - 1.12 torr for optimum mid-IR laser operation. A 500 kHz pulse train with 50 ns pulse width provided the optimum pump laser performance for pulse mid-IR laser operation. For gas pressures above 1.65 torr mid-IR laser efficiency was decreased

due to intermolecular collisions. And this mid-IR laser design provides the platform for an all-fiber HOFGLAS system, which is compact and robust. In fact, an all-fiber mid-IR HOFGLAS system was demonstrated by the same authors [30]. Basically, the experimental setup was identical to that of Ref. [29]. Only the pump coupling mechanism was changed to make the system an all-fiber device. The pump power was delivered through a solid-core single mode fiber (SMF). First, SMF was tapered using heating and pulling technique until the tapered fiber has a waist diameter of 45 μm . Then the tapered SMF was inserted into the core of anti-resonant HC-PCF with a core diameter of 70 μm . The connection was carefully sealed with epoxy glue to ensure perfect airtightness. Both CW and pulsed mid-IR lasing were demonstrated by employing acetylene gas inside the HC-PCF. A 10 m HC-PCF was used for CW operation while a 2 m HC-PCF was used for the pulsed operation. A maximum pulse energy of 205 nJ was observed for the pulse mid-IR laser operation, and 185 mW of maximum mid-IR output power was observed for the CW laser operation with acetylene gas pressure of 0.82 torr. Even though this all-fiber design is promising for a compact and robust design, power scaling could be limited due to the damage threshold of the SMF.

Recently, mid-IR lasing at 4.6 μm was observed from an N_2O filled HOFGLAS system [31]. A 45 cm long hypocycloidal kagome structured HC-PCF was used contain the N_2O molecules and fiber has measured loss of 0.03 dB/m at the pump wavelength (1.517 μm) and estimated fiber loss of 33.6 dB/m at lasing wavelength. An OPO at 1.517 μm with a pulse width of 8 ns was used as the pump source. The maximum mid-IR pulse energy of ~ 80 nJ was measured with the optimum gas pressure of 80 torr. The attained maximum optical-to-optical conversion efficiency was about 9% due to higher fiber loss at the lasing wavelength. Here, the lasing mechanism depends on the rotational-vibrational transition of the N_2O molecules. The pump wavelength 1.517 μm

corresponds to the R(15) ro-vibrational transition and two mid-IR lasing wavelengths near 4.6 μm corresponding to the P(17) and R(15) transitions. In this work, the authors did not optimize the fiber length for optimal mid-IR laser output. Optimizing the fiber length and fiber loss at lasing wavelength could result in higher mid-IR energies with better efficiencies. Furthermore, this work suggests that it is possible to extend the HOFGLAS systems to longer wavelength part of the mid-IR region, by optimizing the fiber structure and using appropriate gaseous molecules.

1.2 Importance of this thesis

The main contribution of this thesis was understanding power scaling and determining the mode quality of an acetylene-filled HOFGLAS system. A goal was to remove the laser signal saturation that was seen in the previous acetylene mid-IR HOFGLAS systems and power scale the HOFGLAS system for higher mid-IR output energies (powers). For that, the effect of fiber length, gas pressure, and pump powers are studied. As a result, we were able to remove the laser signal saturation by optimizing the HC-PCF length. Also, highest mid-IR pulse energy of 2.56 μJ was measured, which is the highest ever mid-IR pulse energy that has been measured with an acetylene-filled HOFGLAS system. Moreover, the produced mid-IR pulse energy shows a linear dependence with absorbed near-IR pump energy by gas and is only limited by the available near-IR pump energy. We also showed that the mid-IR output beam is near diffraction-limited by performing a mode quality measurement. Furthermore, a numerical model is established and solved to estimate the absorbed near-IR pump energy by acetylene gas in the HOFGLAS system. Finally, a new near-IR pump source is designed and the construct based on a two-stage OPA to power scale the acetylene HOFGLAS system.

1.3 Thesis outline

Chapter 2 describes the main components of the acetylene filled mid-IR HOFGLAS system. First, vibrational and rotational motions of the acetylene molecule will be discussed and relate them to transitions near 1.5 μm and 3 μm regions. Then, the light guidance mechanisms in HC-PCF are discussed. Furthermore, the design and the operation of current OPA are discussed. Finally, the whole experimental setup for the acetylene filled mid-IR HOFGLAS system is presented.

In Chapter 3, the power scaling of the acetylene filled HOFGLAS system will be discussed. First, the laser signal saturation observed with the previous systems is discussed. Then, the effect of fiber length on the mid-IR laser performance is discussed, and a quantitative study of the laser performance presented. Effect of the pump wavelength on the mid-IR laser performance will also be discussed. Finally, the mid-IR laser performances of two acetylene filled HOFGLAS systems are compared based on the pump pulse widths.

Chapter 4 is dedicated to the discussion of the mode quality of the output mid-IR beam of the acetylene filled HOFGLAS system. The propagation modes for free space and fibers are discussed. Then the M^2 measurement is introduced to quantify the beam quality. First, the proposed experimental procedure is implemented for the output beam of the SMF fiber and then, the experimental procedure and results of the M^2 measurement for the mid-IR output beam of acetylene filled HOFGLAS system is discussed.

Chapter 5 describes the saturation absorption in acetylene. There, a numerical model is proposed to estimate the absorb near-IR pump energy/power by acetylene gas inside the HOFGLAS system. The proposed numerical model is solved for three different acetylene filled HOFGLAS systems and compared with the experimental results.

Chapter 6 focuses on the design and construction of a new near-IR pump based on a two-stage OPA. First, the operation principles of OPA will be discussed. Then, phase matching conditions for uniaxial crystals and biaxial crystals are introduced. Numerical calculations for the OPA process based on the two-stage OPA design also are presented and finally, the experimental results of two-stage OPA will be discussed.

Chapter 7 includes the summary of this thesis work. Finally, the possible future directions of with HOFGLAS systems will be discussed.

Chapter 2 - The acetylene ($^{12}\text{C}_2\text{H}_2$) filled HOFGLAS system

In this chapter, I will discuss the main components of the acetylene filled HOFGLAS system. Acetylene gas at different pressures is used as the gain medium for the HOFGLAS system. Therefore, a brief discussion about molecular physics of acetylene is included in the first section of this chapter. In the first section I will focus on the acetylene's absorptions lines near $1.5\ \mu\text{m}$ which correspond to rotational-vibrational overtone transitions and mid-IR lasing in acetylene. Since we use hollow-core photonic crystal fibers as the waveguide for the HOFGLAS system, light guidance mechanisms in HC-PCFs are briefly discussed in the second section of the chapter. A homemade optical parametric amplifier (OPA) is used as the optical pump source for the acetylene filled HOFGLAS system. The main components of the OPA is discussed in the third section of this chapter and working mechanisms of Nd:YAG laser, tunable diode laser, and tunable fiber laser are briefly discussed. In the final section of this chapter the experimental setup for the acetylene filled HOFGLAS system is introduced with the specific optics that are used in the setup.

2.1 Mid-IR lasing in acetylene ($^{12}\text{C}_2\text{H}_2$)

The mid-IR lasing in the acetylene filled HOFGLAS system relies on the population inversion in acetylene gas inside the hollow-core fiber. The population inversion in acetylene gas is achievable by exciting the acetylene molecules with a strong optical signal at near-IR. Acetylene molecules can make transitions from vibrational ground state to higher vibrational states via vibrational overtone transitions once they are excited with the near-IR optical signal. Then, they can spontaneously relax into the lower vibrational manifold by radiating light at the mid-IR region. To understand these processes, we need to look at fundamental modes and energies (frequencies) that are associated with the rotational-vibrational motion of the acetylene molecule.

Like any other molecule, acetylene has the ability to rotate and vibrate. As the first level, vibrational motion can be studied by treating acetylene molecules as a collection of harmonic oscillators. However, the harmonic motions of nuclei are usually described in terms of normal coordinates, which are linear combinations of coordinate systems that generally describe the displacements of the nucleus. By assuming that the nuclei will act as simple harmonic oscillators for small perturbations around the equilibrium, one can determine the vibrational frequencies and normal modes for acetylene. The procedure for finding the normal modes and frequencies are discussed in Ref. [32] and Ref. [33]. According to Ref. [32], acetylene has five distinct normal modes, and they are depicted in Fig. 2.1. Moreover, those five normal modes comprise three stretching modes and two bending modes. As indicated in Fig. 2.1 the ν_1 and ν_3 normal modes refer to the C-H symmetric and C-H antisymmetric stretches respectively; the ν_4 and ν_5 modes correspond to the symmetric and antisymmetric C-H bend, and the ν_2 normal mode refers to the C-C symmetric stretch. The respective frequency values (energies) are reported in Ref. [33] and summarized in Table 2.1.

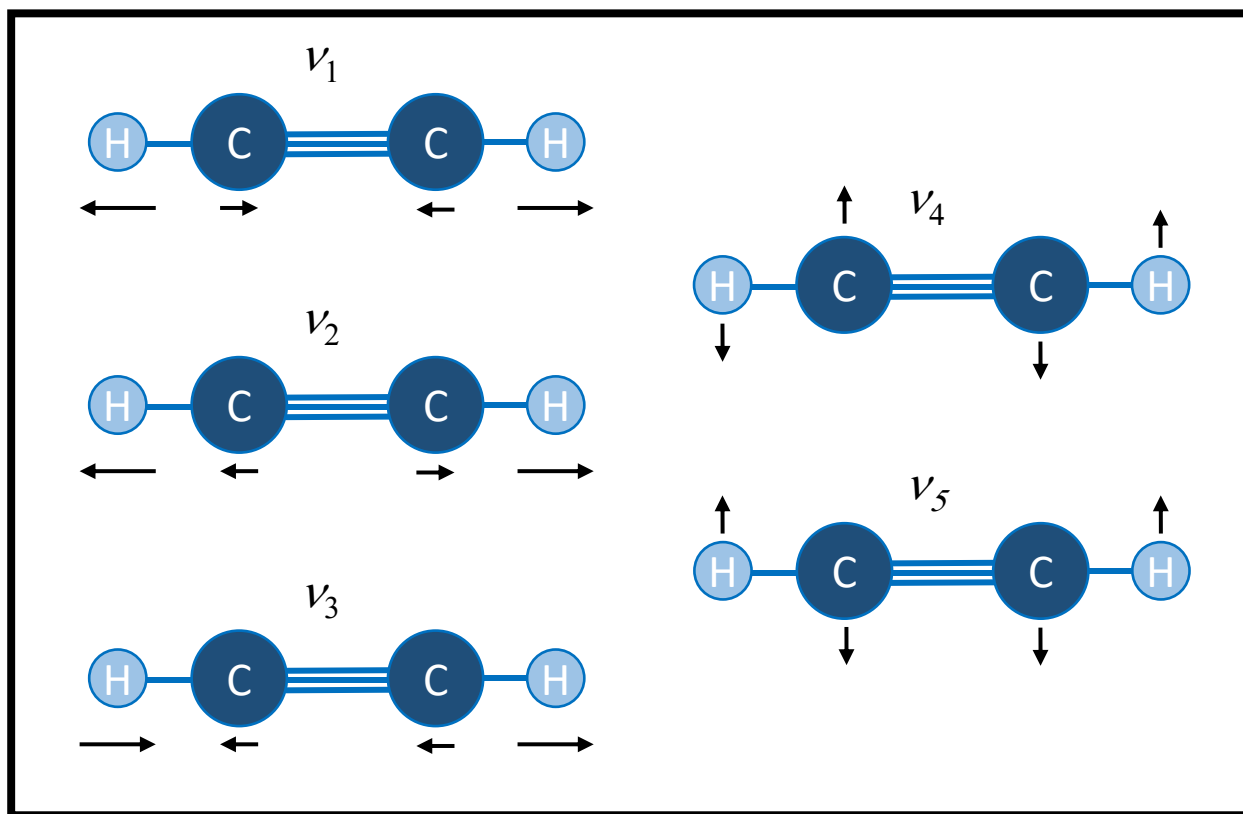


Figure 2.1 The normal modes of acetylene, $^{12}\text{C}_2\text{H}_2$. The relative motions of each atom are indicated by the black arrows (not to scale). The respective vibrational frequencies are shown at upper-middle of each normal mode.

The rotational motion of the acetylene molecule gives additional energy to the vibrational modes, and this creates additional energy states for a given vibrational manifold. The total energy associated with a rotational state J in a given vibrational manifold ν can be written as Eq. 2.1. In Eq. 2.1, $E_{vib}(\nu)$ is the energy of vibrational motion, $E_{rot}(J)$ is the energy of rotational motion and are given by Eq. 2.2 and Eq. 2.3 respectively [34].

$$E_{total}(\nu, J) = E_{vib}(\nu) + E_{rot}(J) \quad 2.1$$

$$E_{vib}(\nu) = h\nu_e \left(\nu + \frac{1}{2} \right) \quad 2.2$$

$$E_{rot}(J) = B_v J(J + 1) \quad 2.3$$

In Eq. 2.2 ν_e is the frequency of the normal mode and in Eq. 2.3 B_v is a constant depend on the vibrational state and can be written as,

$$B_v = B_e - \alpha_e \left(v + \frac{1}{2} \right) \quad 2.4$$

where B_e and α_e depends on the specification of the molecule. For acetylene molecules, these values are reported in Ref. [33].

Table 2.1 Fundamental frequencies for all normal modes of acetylene ($^{12}\text{C}_2\text{H}_2$)

Vibrational normal mode	Description	Frequency (cm^{-1})
ν_1	Symmetric C-H stretch	3397.12
ν_2	Symmetric C-C stretch	1981.80
ν_3	Asymmetric C-H stretch	3316.86
ν_4	Symmetric C-H bend	608.73
ν_5	Asymmetric C-H bend	729.08

A molecule that sits in a specific vibrational- rotational state can make transitions to other states by absorbing or emitting a photon. However, the final state is determined by the dipole selection rules that govern the vibrational-rotational transitions. The transitions between rotational states of neighboring vibrational manifolds are subjected to following selection rules [34].

$$\Delta v = \pm 1 \quad 2.5$$

$$\Delta J = \pm 1, 0 \quad 2.6$$

When a molecule makes a transition between rotational states of adjacent vibrational manifolds the transitions are usually categorized into three branches based on the difference between J value of initial state and the final state. The three branches as follows.

$$\begin{aligned} \text{P branch : } & \Delta J = -1, & J_{final} &= J_{initial} - 1 \\ \text{Q branch : } & \Delta J = 0, & J_{final} &= J_{initial} \\ \text{R branch : } & \Delta J = +1, & J_{final} &= J_{initial} + 1 \end{aligned} \quad 2.7$$

For acetylene molecule the Q branch is not present since no angular momentum is associated with any of the normal modes in Fig. 2.1 and only P and R branches are present. To name the respective transitions usually shorthand notation is used. The transitions are named as $P(J')$, $Q(J')$, and $R(J')$ where P , Q , and R defined in Eq. 2.7, while J' stands to indicate the rotational quantum number of the state with the lowest total energy.

The dipole selection rule $\Delta v = \pm 1$ in Eq. 2.5 is valid for pure simple harmonic oscillator like molecular vibrations. However, if the vibrational motion happens due to a hydrogen stretching in relatively light molecules, the amplitude of the vibration will be larger. As a result, energy associates with vibrational motion cannot be described by simple harmonic motion as in Eq. 2.2 and we should add some degree of anharmonicity to the vibrational potential well. Then we can write anharmonic vibrational energy as,

$$E_{vib}(v) = hv_e \left(v + \frac{1}{2} \right) - hv_e x_e \left(v + \frac{1}{2} \right)^2 + \dots \quad 2.8$$

where, x_e is a measured constant that depends on the electronic state of a given molecule. This anharmonicity allows molecules to make transitions that violate the selection rule in Eq. 2.5 and these transitions called as overtone transitions. These overtone transitions are usually 100 times weaker than the fundamental resonance transitions that follow the selection rule in Eq. 2.5 [35]. If a molecule absorbs or emits light during vibrational transition its dipole moment changes during the transition. These transitions are called infrared active simply because they interact with light at in the frared region. The $\nu_1 + \nu_3$ overtone band of acetylene ($^{12}\text{C}_2\text{H}_2$) is an infrared active band. It has \sim a 50 absorption line from 1510 nm to 1545 nm [36]. This band is divided into R and P-branches as in Fig. 2.2. Since R-branch is for $\Delta J = +1$, those transitions happen at higher energies than the P-branch. Then R-branch transitions absorb or emit light at shorter wavelengths than the P-branch transitions.

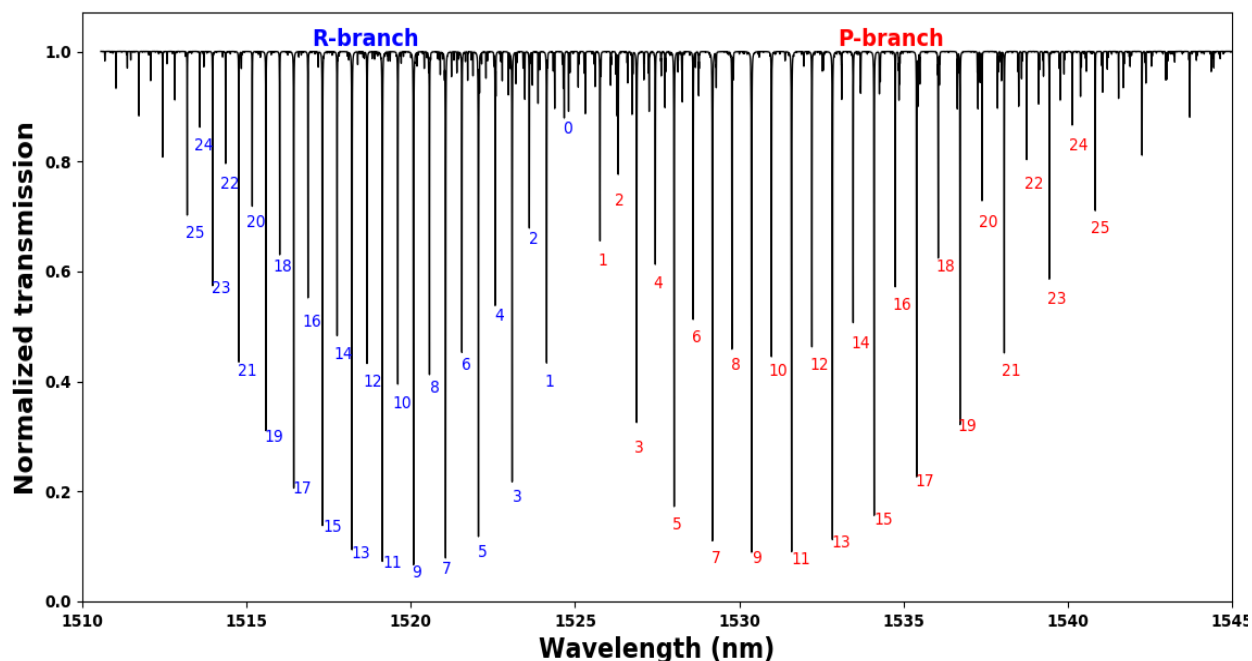


Figure 2.2 Absorption spectrum of acetylene ($^{12}\text{C}_2\text{H}_2$) molecules assuming molecules are in a 5 cm long cell with the gas pressure of 50 torr. This absorption spectrum shows the R and P-branch transition between the vibrational ground state and $\nu_1 + \nu_3$ vibrational manifold. Absorption spectrum was obtained with Spectralcalc simulations [37].

When acetylene molecules excited from the vibrational ground state to $\nu_1 + \nu_3$ vibrational state along any of the stronger absorption line in Fig. 2.2 acetylene molecules can make radiative transitions from the $\nu_1 + \nu_3$ vibrational manifold to ν_1 vibrational manifold. The wavelengths of these radiative transitions lie in the mid-IR region, specifically near to $3.1 \mu\text{m}$ [21]. As an example, previous work have shown mid-IR lasing by acetylene molecules when they were excited along the R(7) absorption line [19, 20]. In our work, we excited the acetylene molecules via P(9) and P(13) absorption lines. Figure 2.3 shows a simplified version of acetylene ro-vibrational levels and transitions that are associated with the P(13) pump line.

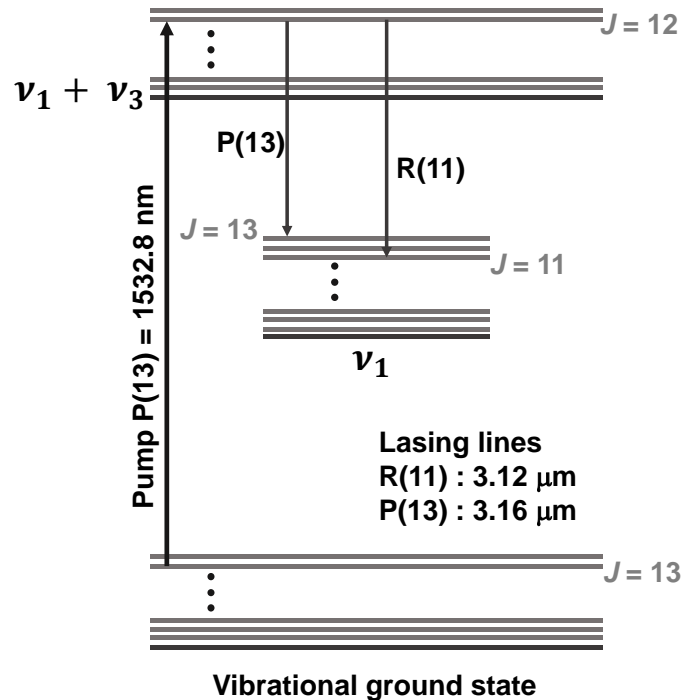


Figure 2.3 A simplified energy level diagram of acetylene P(13) transition. When acetylene molecules are pumped via P(13) line, they can make transitions from rotational state $J=13$ of the vibrational ground state to rotational state $J=12$ of the $\nu_1 + \nu_3$ vibrational manifold. The excited molecules can make radiative transitions from $J=12$ rotational state of the $\nu_1 + \nu_3$ vibrational manifold to $J=13$ or $J=11$ rotational states in the ν_1 vibrational manifold. These radiative transitions are labeled as P(13) and R(11) and have wavelengths of $3.16 \mu\text{m}$ and $3.12 \mu\text{m}$ respectively.

The $\nu_1 + \nu_3$ overtone band of acetylene is extensively studied among the researchers and their spectroscopic properties are well understood [33, 36, 38]. Also, the transitions associated with the $\nu_1 + \nu_3$ overtone band overlap well with the Erbium-doped fiber-based laser systems, and amplifiers operate in the telecommunication C-band. These reasons make the transition between the vibrational ground state and the $\nu_1 + \nu_3$ vibrational manifold to be strong candidates for mid-IR laser pumping. In this work, we used acetylene P(13) and P(9) lines to pump the acetylene filled HOFGLAS system, and these absorption lines are two of the strongest absorption lines in the P-branch as can be seen in Fig. 2.2.

2.2 Hollow-core photonic crystal fibers

Hollow-core photonic crystal fibers (HC-PCF) potentially can replace the gas cells inside traditional molecular gas lasers due to multiple reasons. HC-PCF's hollow-core can hold molecular gases for long time, and its relatively small cross-sectional area provides higher optical intensities. Furthermore, HC-PCF provides a longer interaction length between gas and light. Moreover, since the light can be trapped inside the hollow-core of HC-PCF, they can handle more optical powers than conventional step-index fibers made with fused silica (SiO_2) without introducing unnecessary nonlinear optical and thermal effects, like stimulated raman scattering (SRS), stimulated brillouin scattering (SBS), thermal lensing and material damage. Fused silica has strong material absorption near $2 \mu\text{m}$ due to lattice vibration [39], and this limit the use of solid-core fused silica fiber in mid-IR wavelength applications. Therefore, absent of silica molecules in core opens new applications for HC-PCFs in the mid-IR region. The first HC-PCF was demonstrated in 1999 [40], and since then two major branches of HC-PCFs have developed, Photonic Band Gap Fibers (PBGF) and

kagome-structured fibers. Regardless of fiber type, the fabrication process of HC-PCFs follows the same common core-procedure; the stack and draw technique [41].

The light guidance mechanism in conventional solid-core fiber depends on the total internal reflection (TIR). As shown in Fig. 2.4, light is confined in the core by reflection from the surrounding cladding part. To TIR to happen, the core should have a higher refractive index than the cladding [42]. However, for HC-PCFs TIR is not possible since the core has a lower refractive index than the cladding.

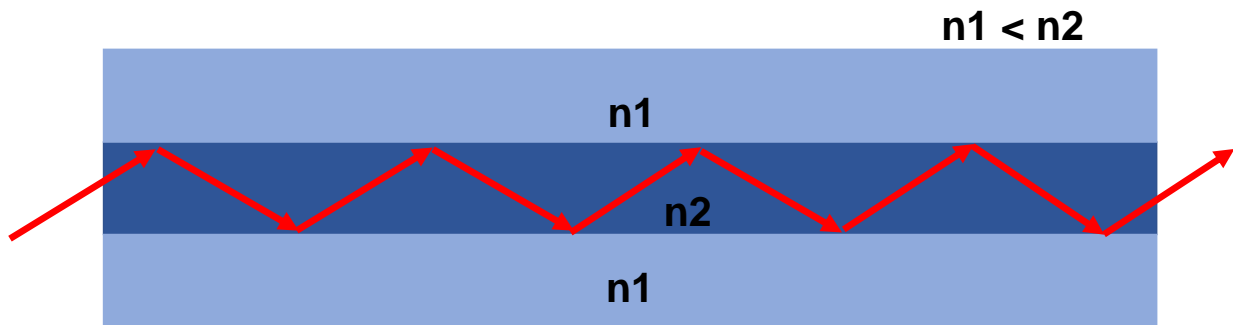


Figure 2.4 In a conventional solid-core fiber, light is confined to the core due to total internal reflection (TIR). The core has a slightly higher refractive index (n_2) than the cladding (n_1). This enables condition for TIR.

As obvious from the name, the light guiding mechanism in the hollow-core of PBGF depends on the photonic bandgap effect [40]. In the hollow-core of the PBGF light in certain well-defined wavelength regions can be guided employing the two-dimensional photonic bandgap effect. These allowed wavelength regions strictly depend on the cladding structure. There are two major types of PBG guidance. These guidance mechanisms are shown in Fig. 2.5. In the first guidance mechanism (Fig 2.5 (a)) the light guidance depends on the frustrated tunneling form. There, light travels in the high index region can leak into the low index region. Then evanescent light can leak into the adjacent high-index region as long as it supports the guidance. The width of these adjacent high-index regions is created in such a way that they are non-resonant with each

other's propagation modes. So, the light leakage by tunneling will be frustrated and hence creates a PBG effect. As shown in Fig 2.5 (b), other PBG guidance depends on the Bragg condition. Here, light is allowed to propagate in all layers and can scatter and interfere depending on the wavelength and the cladding structure. Then, certain bands of wavelength can be confined into the hollow-core by achieving Bragg condition, hence creating the PBG effect [40]. Even though PBGFs have shown fiber loss of 0.012 dB/m at 1550 nm [43] and narrow-band guidance near 3 μm [44], the spectral bandwidth of the band gap region is not enough to cover the octave we need for our acetylene filled HOFGLAS system.

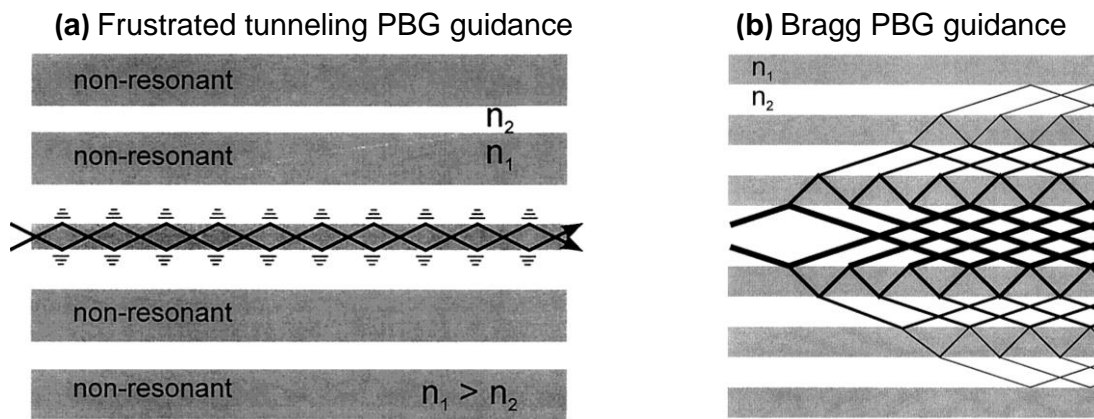


Figure 2.5 The photonic band gap (PBG) guidance supported by (a) frustrated tunneling, (b) Bragg condition. Reproduced with permission from Ref. [40].

On the other hand, kagome-structure HC-PCFs have shown multi-octave guidance with low loss [45]. Unlike in PBGFs, kagome-structured HC-PCFs guide light based on the inhibited coupling between core and cladding modes. This guidance is described in detail in Ref. [46] and Ref. [47]. More generally, evanescent core mode into the cladding is minimized by achieving a small spatial overlap and a modal mismatch of core and cladding modes [47]. The transmission loss and supported spectral bandwidth for these HC-PCFs mostly depend on the design parameters like air-filling fraction, cladding structure's pitch Λ , core diameter, number of rings and number

of cell defects in the core. The air-filling factor is the ratio of the air holes to the total area and the pitch Λ is the spacing between two adjacent microstructures. To name a few, a kagome-structured HC-PCF with 19-cells defect, core diameter of 47.8/68.3 μm and pitch of 12 μm has demonstrated optical transmission windows at visible region (450-700 nm) and the near-IR region (> 1100 nm) [48] while a kagome-structured fiber with 1-cell defects, a core diameter of ~ 15 μm and a pitch of 5 μm has shown guidance of a three-octave spectral comb, spanning from 325 nm to 2300 nm [45]. Figure 2.6 shows cross sections of the aforementioned kagome-structured HC-PCFs. Due to kagome-structured HC-PCFs possess the ability to confine both gas and light inside its core, they have used in many applications like saturated absorption spectroscopy (SAS) [49-51] and nonlinear optics [52, 53]. Furthermore, simultaneous near-IR and mid-IR guidance have observed inside the core of kagome-structured fibers [21, 54] and this makes kagome-structured fiber to be an excellent waveguide and a gas container for our application.

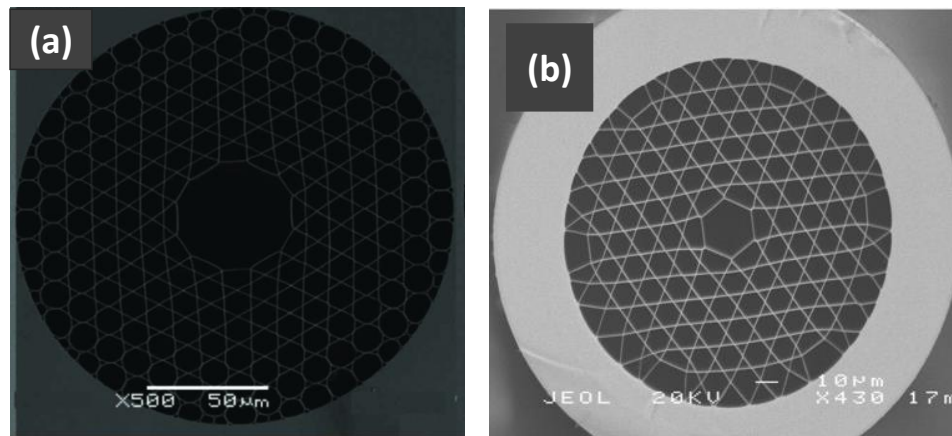


Figure 2.6 The cross-sectional view obtained with a scanning electron microscope of (a) 19-cell defect kagome-structured HC-PCF with a core diameter of ~ 48 μm and pitch of 12 μm (b) 1-cell defect kagome-structured HC-PCF with a core diameter of 15 μm and pitch of 5 μm . Figure (a) reprinted with permission from Ref. [48], [The Optical Society]. Figure (b) Reprinted with permission from Ref.[45], [AAAS].

After the advent of kagome-structured HC-PCF researches have put much effort to minimize the loss associated with these fibers. As a result, a new type of HC-PCF called hypocycloidal kagome-structured has emerged. By introducing negative curvature core shape rather than the conventional circular core shape, Wang *et al.* were able to reduce the fiber loss by a factor of 3 for the spectral region of 1050 to > 1750 nm [55]. A comparison between core shapes of hypocycloidal kagome-structure HC-PCF and conventional kagome-structure HC-PCF is shown in Fig. 2.7. There, both fibers are 7-cell defect, three-ring kagome cladding structure with a similar pitch of $18 \mu\text{m}$ but the core surrounded-design is different. As seen in Fig. 2.7 conventional circular-core kagome HC-PCF has a flat core-cladding boundary, and hypocycloidal kagome HC-PCF has a curved core-cladding boundary. Due to this hypocycloidal kagome-structure HC-PCFs also called as negative-curvature HC-PCFs.

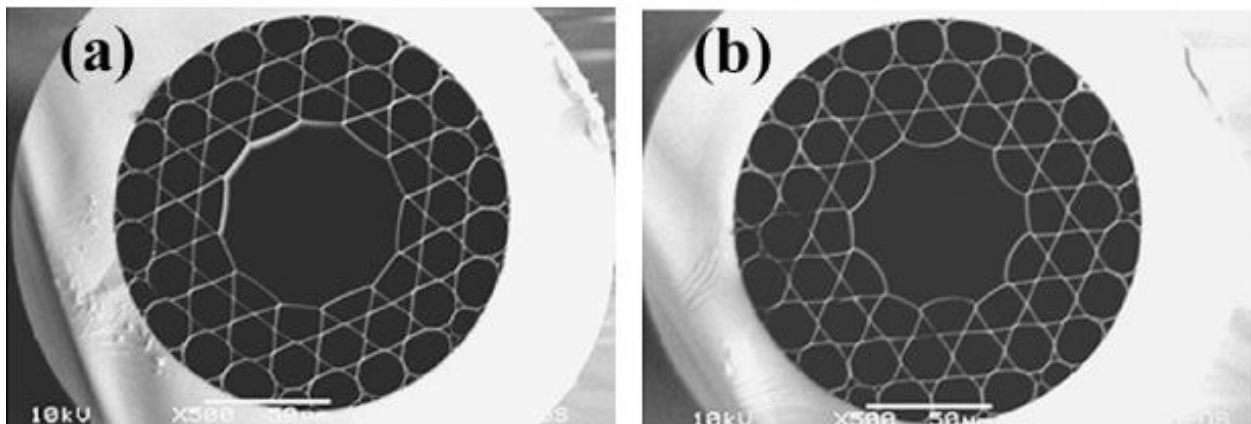


Figure 2.7 Scanning electron microscopic images of 7-cell defect core and three-ring kagome cladding HC-PCF with (a) conventional circular core and (b) a hypocycloid core. Reprinted with permission from Ref. [55], [The Optical Society].

Later, Debord *et al.* numerically and experimentally studied the impact of the aforementioned negative curvature on the transmission loss in hypocycloidal kagome structured HC-PCF and have shown that the confinement loss and the optical power overlap between core and cladding modes can be reduced by increasing the negative curvature [56]. Also, they were able

to demonstrate nearly single-mode guidance with optimized hypocycloidal kagome-structured HC-PCFs. Furthermore, researchers have developed larger core size hypocycloidal kagome structured fibers to handle high power laser beams, and these fibers demonstrate low propagation loss (0.1 dB/m) over broad transmission range [57]. Also, mid-IR guidance inside the core of hypocycloidal kagome HC-PCF has been demonstrated by Yu *et al.* [58], and simultaneous near-IR and mid-IR guidance were observed in Ref. [31]. Due to high power handling ability, multi-octave guidance with low propagation loss and near single-mode guidance we used a hypocycloidal kagome-structured HC-PCF to power scale our mid-IR laser setup. The HC-PCF used in this work is fabricated by Gas-Phase Photonic and Microwave Materials group (GPPMM) in xlim research institute in France and is generously provided by our collaborator Dr. Fetah Benabid. Figure 2.8 shows the cross-section and the near-IR loss spectrum for this HC-PCF. The fiber has a hypocycloidal core shape with 7-cell defect and surrounded by the 3-ring kagome – structured cladding. The inner-core diameter is 60/72 μm and out fiber diameter $\sim 360 \mu\text{m}$. The fiber has measured losses of 0.08 dB/m near 1532 nm and 1.13 dB/m near 3 μm .

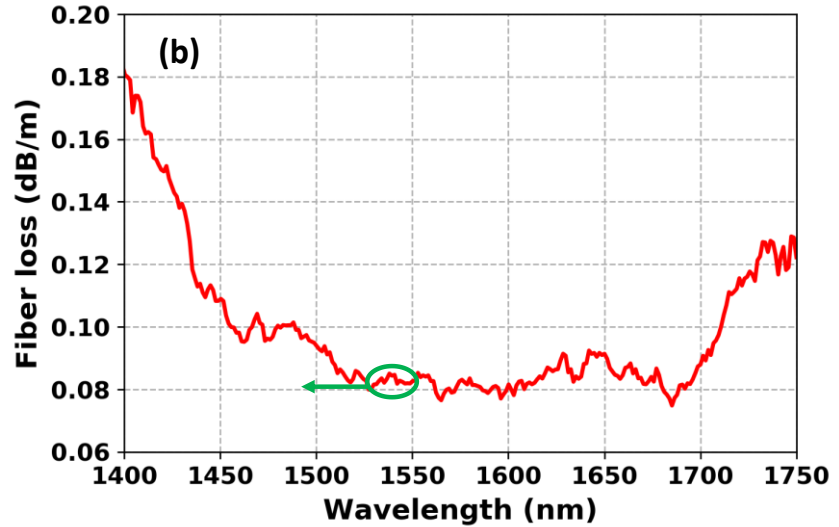
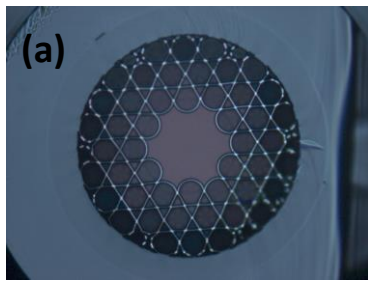


Figure 2.8 Hypocycloidal kagome-structured HC-PCF with 7-cell defect, 3-ring kagome cladding, a core diameter of 60/72 μm (a) cross section and (b) near-IR loss spectrum. Both the picture of the cross-section and loss spectrum data are provided by Ref. [59]

2.3 The optical parametric amplifier for acetylene HOFGLAS system

As discussed in Section 2.1 the mid-IR lasing in acetylene depends on the population inversion in the lasing states. To achieve a significant population inversion, a strong, tunable coherent optical source near 1.5 μm is needed. One way to fulfill the above-mentioned requirement is an optical parametric amplifier (OPA). The working mechanism of the OPA will be discussed in Chapter 6. The OPA works at near-IR is used to excite the acetylene molecules in the HOFGLAS system. This OPA is designed and built by Dr. Andrew Jones and reported in Ref. [60]. Figure 2.14 shows the schematic of the OPA that is used as the pump source for the acetylene filled HOFGLAS system. The OPA consists of three main components. A high power/energy pump laser, a low power/energy seed laser, and a nonlinear crystal to mix both pump and seed laser beam.

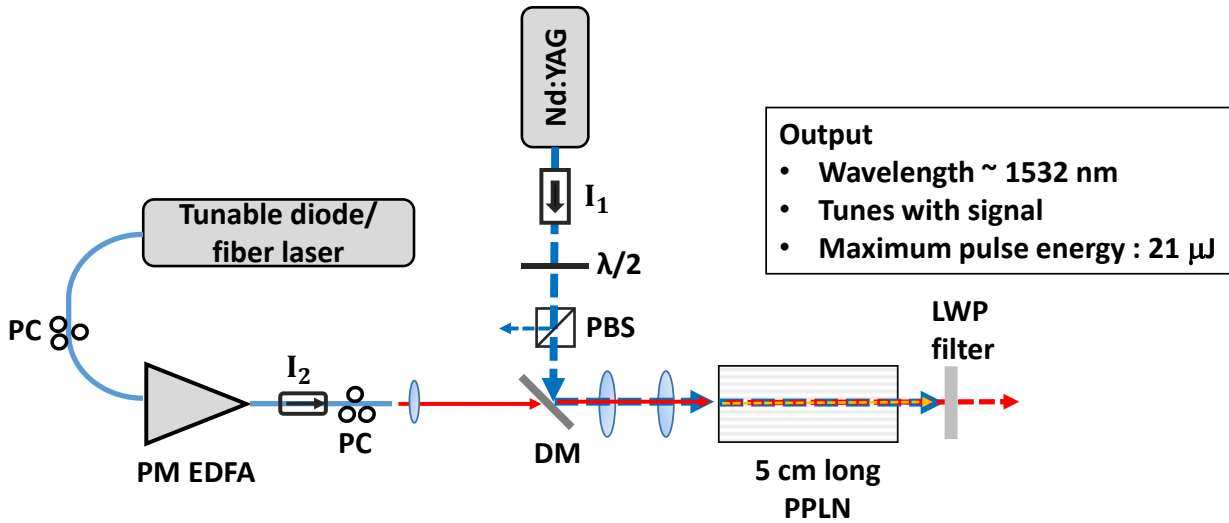


Figure 2.9 A schematic of the optical parametric amplifier (OPA). A 5 cm long MgO doped PPLN crystal is used to mix the pump and signal beams. I_1 is a free space faraday isolator and I_2 is fiber coupled isolator. PC- paddle polarizer controllers. DM- Long wavelength pass dichroic mirror. PBS- polarizing beam splitter. PM EDFA- Polarization maintain Erbium doped fiber amplifier.

A pulsed Nd: YAG laser is used as the pump source. Inside this laser Nd:YAG rod is pumped with a continuous wave (CW) diode laser at 800 nm and lases at 1064 nm. Pulsed laser operation is achieved by a technique called Q-switching. Here, high energy short pulses (typically few hundreds of picoseconds or longer) are obtained by modulating the intracavity loss of the laser. To generate the Q-switched pulse, initially the laser's cavity losses are kept at a higher level (usually by controlling the feedback from the cavity to the gain medium), so the population inversion keeps building up inside the gain medium. Then the optical losses are suddenly dropped to a small value and allow the low loss feedback with the gain medium so that the energy stored in the gain medium due to the population inversion is rapidly dumped by producing a short pulse with high energy. There are two types of Q-switching: active Q-switching and passive Q-switching. In active Q-switching, an active control element like acoustic-optic modulator (AOM) or electro-optic modulator (EOM) is used to control the losses. In passive Q-switching, saturable

absorber is used inside the optical cavity. Here, the absorption coefficient is intensity dependent and have a higher value for low optical intensities and a negligible amount for higher intensities. Then, saturable absorber preferably absorbs more light with low intensities and becomes transparent for the higher optical intensities. This way saturable absorber acts as an intensity dependent switch and controls the cavity losses. Usually, doped glass or crystals (like Cr⁴⁺: YAG, Co²⁺: ZnSe) are used to made saturable absorbers [61]. For a saturable absorber with a homogeneous line broadening mechanism, the saturated absorption coefficient α can be written as [62],

$$\alpha = \frac{\alpha_0}{1 + I/I_s} \quad 2.20$$

where α_0 is the unsaturated absorption coefficient, and I_s is the saturation intensity.

The Nd: YAG laser (CryLas-2STA-240) used in the OPA operates at 1064 nm, capable of producing pulses in 1 ns pulse duration (FWHM) with 3 mJ of pulse energy and have an adjustable repetition rate of 1-100 Hz. Moreover, the pulsed operation achieved via the passive Q-switching [60]. For typical OPA operation, the Nd:YAG laser is externally triggered at 30 Hz with TTL pulses from Stanford research systems delay generator and Dr. Andrew Jones observed instability in laser's output with higher rep rates [60].

An extended cavity diode laser (Santec TSL-210) or narrow linewidth CW fiber laser (Orbits Lightwave) is used along with a polarization maintaining Erbium-doped fiber amplifier (PM-EDFA) from IPG Photonics (model number: EAR-0.5-C-LP) as the near-IR seed source the OPA. In external cavity diode laser, a laser diode with relatively large output bandwidth is pointed to a grating to narrow the linewidth, and retroreflected with a mirror. To select the required

wavelength between 1505 – 1585 nm, the grating which is mounted on a rotational stage can be rotated using PZT controllers. On the other hand, the cavity of the narrow linewidth CW fiber laser consists of a fiber where a part of the fiber is doped to the attain gain. The fiber is optically pumped using a laser diode. A PZT is glued to a section of the fiber so that the cavity length can be changed by applying high voltages to the PZT and this allows the tunability of the center wavelength [63]. For the OPA, PM-EDFA is seeded with ~ 5 mW optical power at 1532 nm by using either the extended cavity diode laser or narrow band CW fiber laser and the EDFA output set to 300 mW.

A 5 cm long magnesium oxide doped congruently grown periodically poled lithium niobate (MgO:PPLN) crystal is used to mix the pump and signal laser beams. This PPLN crystal consists of four separate poling periods: 30 μm , 30.5 μm , 31 μm , and 31.5 μm . The poling period of 30 μm is used for the required OPA process, and crystal is heated up to 105 °C to achieve the phase matching. Only 200 μJ Nd:YAG energy is used as the pump energy due to the damage threshold of PPLN crystal. The pump pulses are mixed along the 30 μm poling period with 300 mW of CW power at 1532 nm, and energy from the pump beam is transferred to the signal beam through the DFG. Also, the idler beam at 3 μm with moderate energy is generated to conserve the photon energy. Then the amplified signal beam is filtered out with a long pass filter and have a maximum pulse energy of 21 μJ with a pulse duration of 1 ns and a repetition rate of 30 Hz.

2.4 Experimental setup of acetylene filled HOFGLAS system

A simple schematic of the mid-IR laser setup is shown in Fig. 2.15. A 7.6 m long hypocycloidal kagome-structured HC-PCF serves as the laser cavity by containing acetylene molecules and guiding both pump and laser light. Both ends of the HC-PCF are terminated inside two vacuum chambers, and fiber ends are accessible through vacuum windows. The optics used in the input

end of the fiber are made with BK7 and anti-reflection (AR) coated for maximum near-IR pump transmission. A plano-convex lens with focal length $f = 7.5$ cm is used to couple near-IR pump pulses from OPA into the fiber. This specific focal length $f = 7.5$ cm is chosen by matching the mode field diameter of fiber with the mode and beam size of the OPA beam. The coupling efficiency of 65% is obtained using the aforementioned focal length. A combination half-wave plate and the polarizing beam splitter is used to control the input pump pulse energy to the acetylene filled HC-PCF. CaF₂ optics are used at the output end of the fiber so that both near-IR pump and generated mid-IR laser pulses are transmitted effectively. The output beams are collimated using a CaF₂ with a focal length $f = 15$ cm. A 5 mm thick germanium filter is used to filter the residue pump energy from the produced mid-IR energy. The input and output pulse energies are measured with a sensitive pyroelectric sensor.

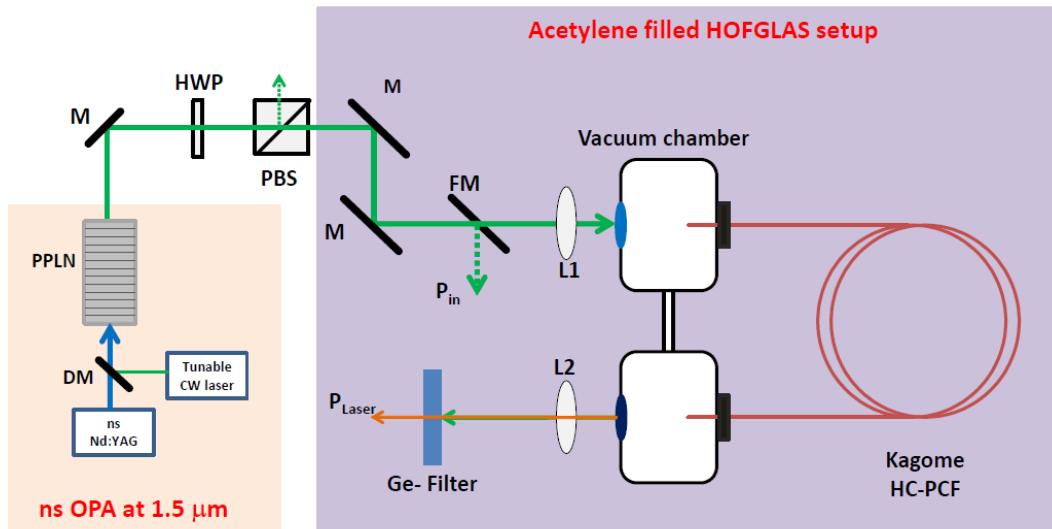


Figure 2.10 A simple schematic of the OPA pumped acetylene HOFGLAS system. All the optics in the input end are made with BK7, and all the optics in the output end are made with CaF₂. The length of the HC-PCF is 7.6 m. HWP- Half wave plate, PBS – Polarizing beam splitter, M – silver mirrors, DM- dichroic mirror, FM- silver mirrors on flipper mount, L1 – BK7 lens with focal length $f = 7.5$ cm, L2 – CaF₂ lens with focal length $f = 15$ cm, P_{in} - input near-IR OPA pump pulse energy, P_{laser} – Produced mid-IR pulse energy. Adapted with permission from Ref. [64], [SPIE].

Chapter 3 - Power scaling of the acetylene filled HOFGLAS system

In this chapter, I will discuss how we work towards power scaling the acetylene filled HOFGLAS system. Effects of fiber length, acetylene gas pressure, pump pulse energy and pump wavelength on laser performance are studied and will be discussed in the following sections. To power scale a laser system it is important to remove the laser signal saturation. For a given laser system output, the laser signal depends on the net gain inside the laser cavity. This net cavity gain depends on all the losses and gain inside the cavity. The gain is proportional to the population difference on the lasing transition. For a given system aforementioned population difference depends on the available number of absorbers and the pump power. If the population difference is no longer changing due to the limited number of absorbers, the gain and the net cavity gain also saturated. Hence, the laser signal is saturated. In the following sections, I will discuss the laser signal saturation observed in previous acetylene filled HOFGLAS system and how we reduced it using a combination of different fiber lengths and acetylene gas pressures. Some of the data that are presented in this chapter are published in Ref. [64] and reproduced with permission from SPIE.

3.1 Laser signal saturation in previous acetylene filled HOFGLAS system

In 2011 Andrew Jones [60] used a 1.46 m long 18.75 μm pitch and the core diameter of 85-94 μm kagome-structured HC-PCF in the HOFGLAS system with different acetylene gas pressures to study the mid-IR laser performance. The kagome-structured HC-PCF has a loss of 0.1 dB/m at 1.5 μm , in the regions of pump wavelengths. The fiber loss between 3.1 and 3.2 μm is approximately 5 dB/m. Acetylene molecules inside the fiber were pumped at a wavelength of 1532.8 nm which corresponds to the P(13) rotational-vibrational overtone transition. The measured mid-IR pulse energy at different acetylene gas pressures are depicted in Fig. 3.1 as a function of

absorbed near-IR pump pulse energy only by gas. Even though the maximum mid-IR energy of 0.5 μJ was obtained with acetylene pressure of 29.8 torr laser signal output is saturated at all acetylene gas pressures that were studied. The laser saturation normally happens when the total population inversion is achieved. Once the total population inversion is reached the ground state population is totally depleted, and further pump absorption is unlikely. Also, since the total inversion is reached laser output should remain the same. However, according to Fig. 3.1 acetylene molecules have absorbed the near-IR pump pulse energy even after saturation is achieved.

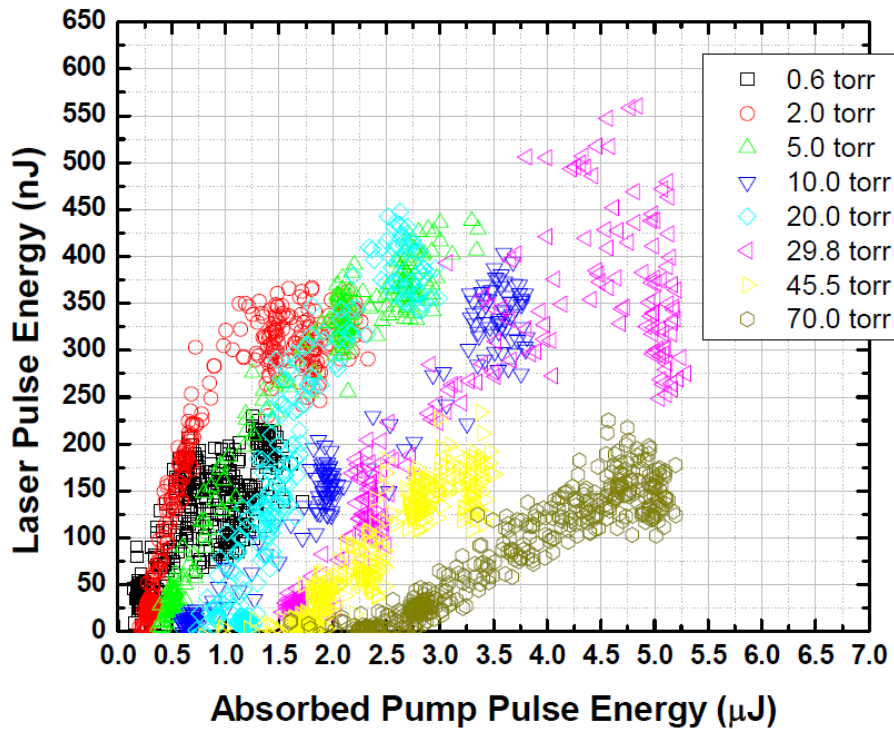


Figure 3.1 The measured mid-IR pulse energy at different acetylene gas pressures as a function of absorbed near-IR pump pulse energy for an 1.46 m long kagome-structured HC-PCF with the core diameter of 85-94 μm . Adapted from Ref. [60].

As per Ref. [60], additional pump absorption by already excited acetylene molecules may cause the aforementioned laser signal saturation like effect without contributing to the mid-IR lasing. This suggests that to eliminate laser signal saturation, more absorbers need to be in the

ground state in order to interact with higher pump energies. There is a couple of ways to add more acetylene molecules into the fiber; higher gas pressure with shorter fiber and lower gas pressure with longer fiber. At high gas pressure, the absorption line profile gets wider due to intermolecular-collisions, and limits overlap with the optical pump beam. Also, these collisions reduce the number of molecules in the excited state without contributing to mid-IR lasing. Therefore higher gas pressure with a shorter fiber is not an effective route to eliminate the laser signal saturation in acetylene filled HOFGLAS system. The effective way to remove the laser signal saturation in the acetylene HOFGLAS system could be using a low loss longer fiber with lower acetylene gas pressures inside the fiber.

In 2017 Neda Dadashzadeh [65] used an 11 m long hypocycloidal kagome-structured HC-PCF with the core diameter 60-72 μm in the acetylene HOFGLAS system. The hollow-core fiber used in above work has loss of 0.08 dB/m at pump wavelength 1532.8 nm and loss of 1.13 dB/m at the lasing wavelength near 3.1 μm . There, HC-PCF was filled with different acetylene gas pressures ranging from 1 torr to 14 torr to study the mid-IR laser performance. The measured mid-IR laser energy in the above work at different gas pressures is shown in Fig. 3.2 as a function of absorbed gas pressure only by acetylene gas.

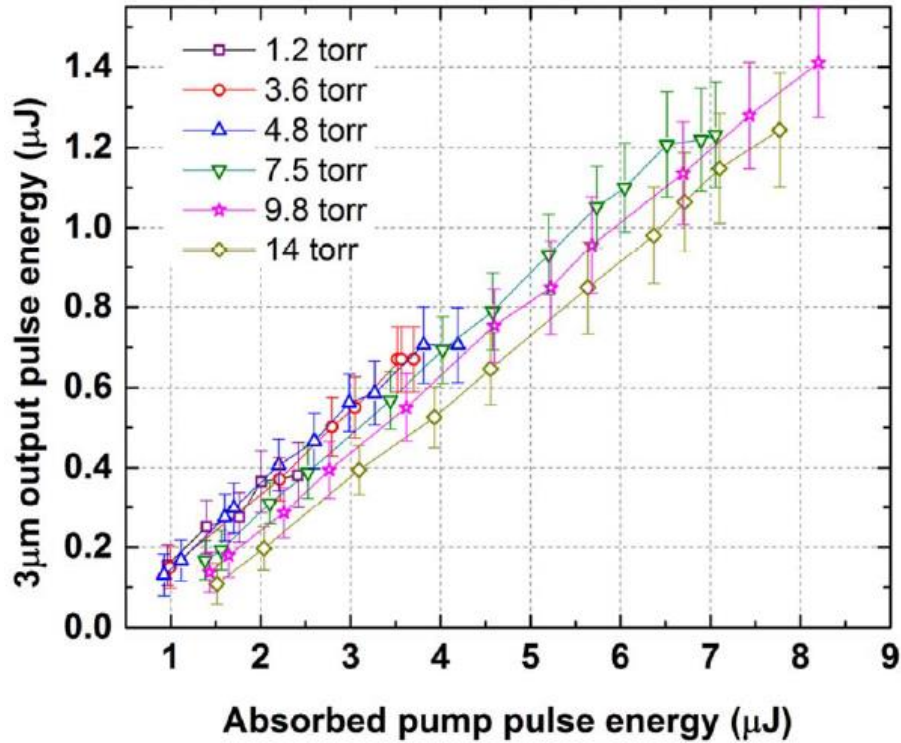


Figure 3.2 The measured mid-IR pulse energy at different acetylene gas pressures as a function of absorbed near-IR pump pulse energy by acetylene molecules for an 11 m long hypocycloidal kagome-structured HC-PCF with the core diameter of 60-72 μm . Adapted from Ref. [65].

By using the longer, lower loss hollow-core fiber, the laser signal saturation was removed for acetylene gas pressures above 7.5 torr. Even though the highest mid-IR energy of 1.4 μJ was obtained with acetylene gas pressure of 9.8 torr, still the mid-IR laser output suffered laser signal saturation at lower acetylene gas pressures. Figure 3.3 shows the produced mid-IR energy as a function of coupled near-IR pump pulse energy into the HC-PCF. In Fig. 3.2, for a given laser operation with lower gas pressure, a similar amount of near-IR pump energy was absorbed by the acetylene molecules once the laser signal saturation is reached. This can be seen when the lower pressure data in Fig. 3.2 and Fig. 3.3 are compared. It is an indication that at lower pressure limit the number of absorbers is still not enough to absorb the near-IR pump energy to contribute to

lasing transition effectively. Also, at lower gas pressure limit, the total fiber loss at lasing wavelength equals to 12.4 dB and may dominate the total gain once the total population is reached. This suggests that the combination of acetylene gas pressure and fiber length is still not optimized and lays the foundation to the current study.

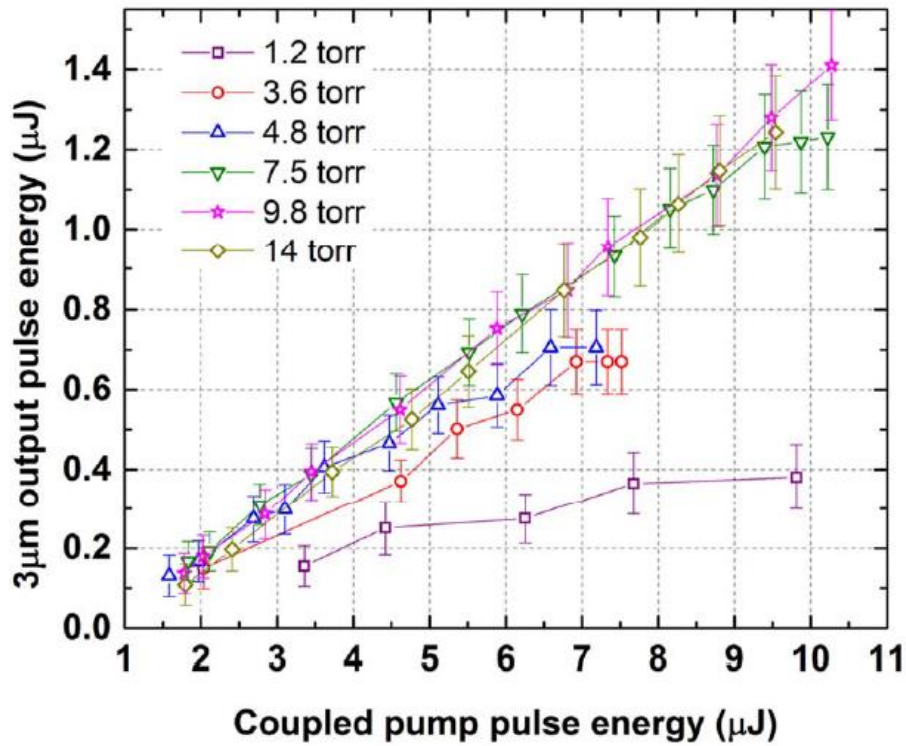


Figure 3.3 The measured mid-IR pulse energy at different acetylene gas pressures as a function of coupled near-IR pump pulse energy for an 11 m long hypocycloidal kagome-structured HC-PCF with the core diameter of 60-72 μm . Adapted from Ref. [65].

3.2 Effect of fiber length

As discussed in the previous section, the fiber length was not optimized for acetylene filled HOFGLAS system, so thus a better systematic study on the fiber length is needed. In this section, I discuss how we study the effect of fiber length on the acetylene filled HOFGLAS system and how we work towards power scaling the system by removing the laser signal saturation that was observed in the previous work.

To study the fiber length effect, a 7.6 m long hypocycloidal-kagome-structured fiber is used in the acetylene filled HOFGLAS system. The fiber has similar specifications as the one reported in Ref. [65]. The experimental setup which has been discussed in section 2.4, is used to perform the experiment. Similar acetylene gas pressures are tried inside the hollow-core fiber to make a better comparison with Ref. [65]. Furthermore, the same near-IR pump wavelength is used to excite the acetylene molecules. The seed laser for the nanosecond OPA is scanned around the wavelength of 1532.8 nm. By doing this, we were able to tune the OPA near-IR signal output to be on and off resonance with P(13) absorption line of acetylene $\nu_1 + \nu_3$ overtone transition.

As in Fig. 2.15 both ends of the hollow-core fiber are terminated inside the vacuum chamber. Both ends of the fiber are cleaved properly to maximize the pump and laser coupling in and out from the fiber. The fiber ends are secured inside vacuum chambers as mentioned in Ref. [65] to isolate from the atmosphere. Vacuum chambers are filled up to the desired acetylene gas pressure (1.4-14 torr) once the fiber ends are securely inserted into them. According to Ref. [65], acetylene molecules take few hours to reach the equilibrium pressure inside a longer fiber (10.9 m). Since the fiber used in the current work is relatively long (7.6 m), we waited approximately two hours until the equilibrium pressure is obtained. Once the system is equilibrated in terms of acetylene gas pressure inside the fiber, acetylene molecules are excited with near-IR OPA pulses. The OPA operation is discussed in section 2.3. As a note, a CW tunable narrow linewidth (~ 100 kHz) extended cavity diode laser with an EDFA (Manlight) is used as the seed for the OPA. The abovementioned tunable diode laser can cover the wavelength region from 1510 nm to 1560 nm and this wavelength region coincides with acetylene molecules' P and R branches at near-IR absorption spectrum. The poling period of $30.5 \mu\text{m}$ on the PPLN crystal is used to mix the ns-pump laser at 1064 nm with near-IR seed signal, and the crystal temperature is tuned to 105°C to

achieve appropriate phase-matching. A combination of half-waveplate (Thorlabs WPH05M-1550) and polarizing beam splitter (Thorlabs PBS254) is used to vary the input pump energy to the HOFGLAS system. All the optics that are used couple pump light into the fiber AR coated, in order to maximize the pump coupling. An AR coated plano-convex lens with a focal length of $f=7.5$ cm is used to couple the near-IR pump light into the fiber. This lens is chosen by matching the mode and beam size of the OPA beam with the mode field diameter of the hollow-core fiber. By doing this, we were able to improve the average coupling efficiency up to 65%. At the output end of the hollow-core fiber, optics made with CaF_2 are used to transmit the produced mid-IR energy and residue pump energy efficiently. The produced mid-IR laser beam is collimated by using CaF_2 lens with a focal length of 15 cm. The near-IR input pump energy, produced mid-IR pump energy and residue of near-IR pump energy are measured at relevant points using a sensitive pyroelectric energy meter.

3.2.1 Quantitative study of laser optical properties

Before moving into the detailed discussion of laser optical properties, it is important to discuss the mid-IR lasing mechanism by acetylene molecules when they are excited with the near-IR optical beam. The mid-IR laser mechanism can be explained by using a 3-level system as in Fig. 3.4. As discussed in section 2.1 acetylene has around 50 absorption lines in the wavelength region of 1510 – 1560 nm. In this work, acetylene molecules are excited along P(13) absorption line which corresponds to the wavelength of 1532.8 nm. This wavelength corresponds to the transition of acetylene molecules from the vibrational ground state to the $\nu_1 + \nu_3$ vibrational state. The ν_1 vibrational mode corresponds to the symmetric C-H stretch, and ν_3 vibrational mode

corresponds to the anti-symmetric C-H stretch of the acetylene molecule. The normal modes of the acetylene molecules are shown in Fig. 2.1.

When the acetylene molecules are excited along the P(13) line, the $J = 12$ rotational state of $\nu_1 + \nu_3$ the vibrational state is populated with molecules from $J = 13$ rotational state of the vibrational ground state. Once the population in $J = 12$ rotational state of $\nu_1 + \nu_3$ vibrational manifold exceeds the population in the ν_1 vibrational manifold, acetylene molecules can make dipole rule allowed radiative transitions to $J = 13$ or $J = 11$ rotational states of the ν_1 vibrational manifold. These radiative transitions are classified as P(13) and R(11), have wavelengths of 3.17 μm and 3.11 μm respectively [21, 27]. In addition to these radiative transitions, excited molecules can exchange their energy non-radiatively by intermolecular collisions and collisions with fiber wall. These nonradiative process can potentially reduce the overall laser efficiency, and these effects will be discussed in a later section.

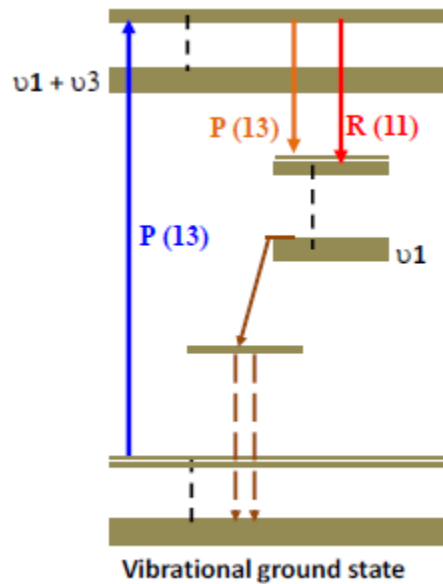


Figure 3.4 Simplified ro-vibrational energy level diagram of acetylene. The lasing wavelengths 3.11 μm and 3.17 μm correspond to the R(11) and P(13) transitions when pumped via P(13) line.

Figure 3.5 shows a simplified version of acetylene filled HOFGLAS system with the relevant points to do each measurement. In Fig. 3.5 green lines indicate the pump beam and red line indicates mid-IR laser output.

The most critical physical quantities to describe the laser properties and dynamics are the produced mid-IR pulse energy and the absorbed near-IR pump pulse energy only by acetylene gas. The produced mid-IR energy is a straightforward measurement. We can simply estimate the produced mid-IR energy by measuring it just after the germanium filter and then correct for optical losses due to various optics in the setup. Since acetylene molecules absorb near-IR pump energy nonlinearly, we cannot measure the absorbed near-IR pump energy as a direct measurement.

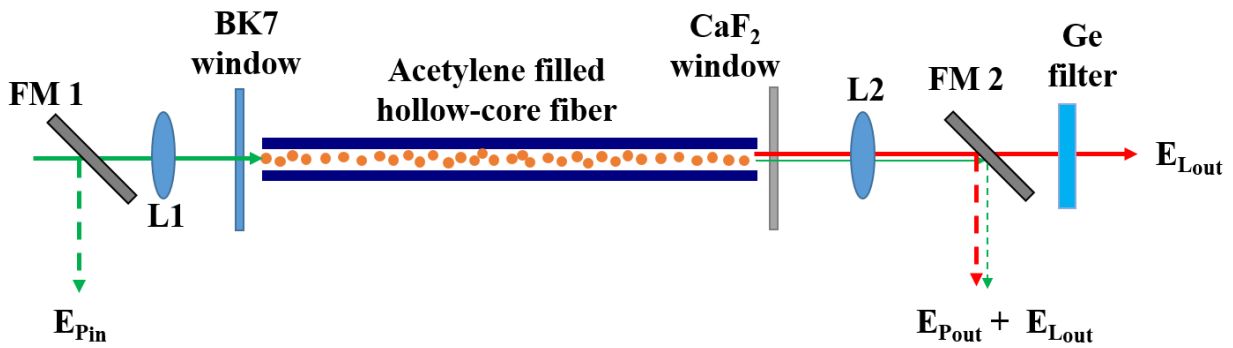


Figure 3.5 Simplified experimental setup of acetylene filled HOFGLAS system showing where the near-IR pump energies and produced mid-IR energies are measured. E_{Pin} and E_{Pout} are the incident and transmitted pump pulse energies measured with pyroelectric energy meter. E_{Lout} is the measured mid-IR pulse energy using the same energy meter. L1 is an AR coated BK7 plano-convex lens with a focal length of 7.5 cm and L2 is a CaF_2 plano-convex lens with a focal length of 15 cm. FM 1 and FM 2 are flipper mounts which are used to direct the beam towards the energy meter head. A 5mm thick germanium filter is used to filter out the produced mid-IR energy from the residue pump energy.

Before taking any significant data with the setup, the near-IR pump coupling efficiency is determined for each input near-IR pump energies. After confirming there is no power dependent coupling into the hollow-core fiber, it is filled with acetylene molecules up to desired gas pressure.

Again the pump coupling efficiencies are checked by tuning the OPA to be off resonance with P(13) absorption line. For this purpose, the seed laser is tuned to be at least 1 GHz away from the center frequency of the P(13) absorption line. Once the OPA is on-resonance with the P(13) line, input near-IR pump pulse energy ' E_{Pin} ,' residue pump pulse energy ' E_{Pout} ' and the produced mid-IR pulse energy ' E_{Lout} ' are measured as in Fig. 3.5. Since the energy meter reading depends on the wavelength of the optical beam, care has to be taken while measuring the residue pump energy along with produced laser pulse energy. First the produced mid-IR laser output energy is measured by selecting the 3 μm as the wavelength setting in the energy meter. Then the same measurement is done by selecting the 1.5 μm as the wavelength setting. All the other measurements are done with the 1.5 μm setting on the energy meter. To find the residue near-IR pump energy after the hollow-core fiber the measured mid-IR energy under 1.5 μm scaling is used. To make sure that the OPA signal output is on-resonance with acetylene P(13) absorption line, a small portion (1%) of seed laser for the OPA is send through a 5 cm long 50 torr acetylene cell as in Fig. 3.6 and, transmission through the acetylene cell is observed with a large area photodiode (New Focus Model: 2033). The on-resonance condition is made sure by observing a minimum laser transmission through the acetylene cell, *i.e.* observing the lowest reading on the voltmeter in Fig. 3.6.

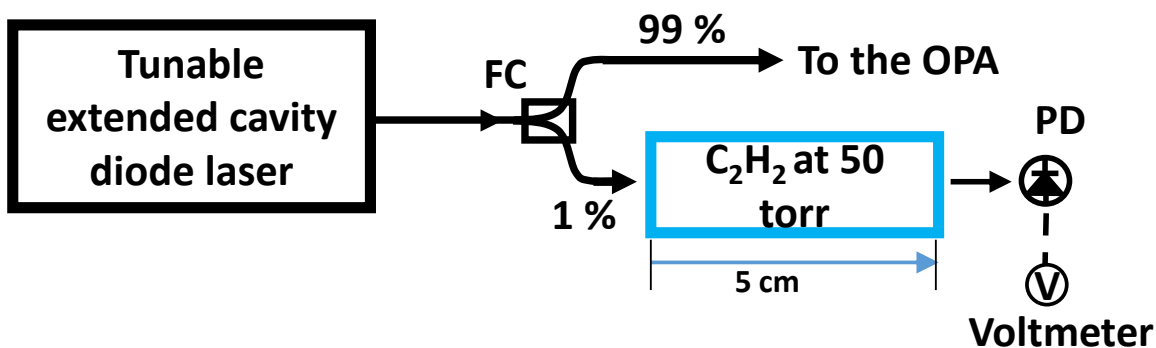


Figure 3.6 A simple schematic of the experimental setup that is used to verify the on-resonance condition of OPA signal wavelength with P(13) absorption line of acetylene. FC is a 99:1 fiber coupler and PD is a large area photodiode.

Figure 3.7 shows the produced mid-IR pulse energy as a function of coupled near-IR pump pulse energy into the fiber. The off-resonance near-IR pump coupling efficiencies into the fiber are used to estimate the on-resonance coupled near-IR pump pulse energies. Also, any near-IR pump pulse energy lost due to imperfect fiber guidance is included in the coupled pump pulse energy. Assuming linear pump power absorption in the fiber the total pump losses due to the fiber is 0.6 dB. Each data point is taken by averaging 500 pulses to get more reliable data, In Fig. 3.7 the error bars stand for the standard deviation of each measurement. Figure 3.7 shows a laser signal saturation like effect at acetylene gas pressure of 1.4 torr. This saturation like effect is mainly due to the limited number of acetylene molecules in the system at that pressure, and that limits the amount of pump absorption hence saturates the mid-IR lasing. Even though laser signal saturation like effect is observed at lowest pressure, no saturation like effect is observed at higher acetylene gas pressures. The highest mid-IR pulse energy of 2.3 μJ is obtained at 14 torr acetylene gas pressure by coupling 12.3 μJ of near-IR pump pulse energy into the fiber. The laser efficiency for each acetylene gas pressure with respect to the coupled near-IR pump energy is found by fitting the relevant data to a linear line. The maximum laser efficiency of 20% with respect to coupled near-IR pump pulse energy is observed at the acetylene gas pressure of 14 torr. In comparison to

previous work done by Neda Dadashzadeh [65], we were able to increase the mid-IR laser output pulse energy by approximately 1 μJ with a shorter fiber length. Moreover, laser signal saturation like effect is removed for most of the acetylene gas pressures that are studied.

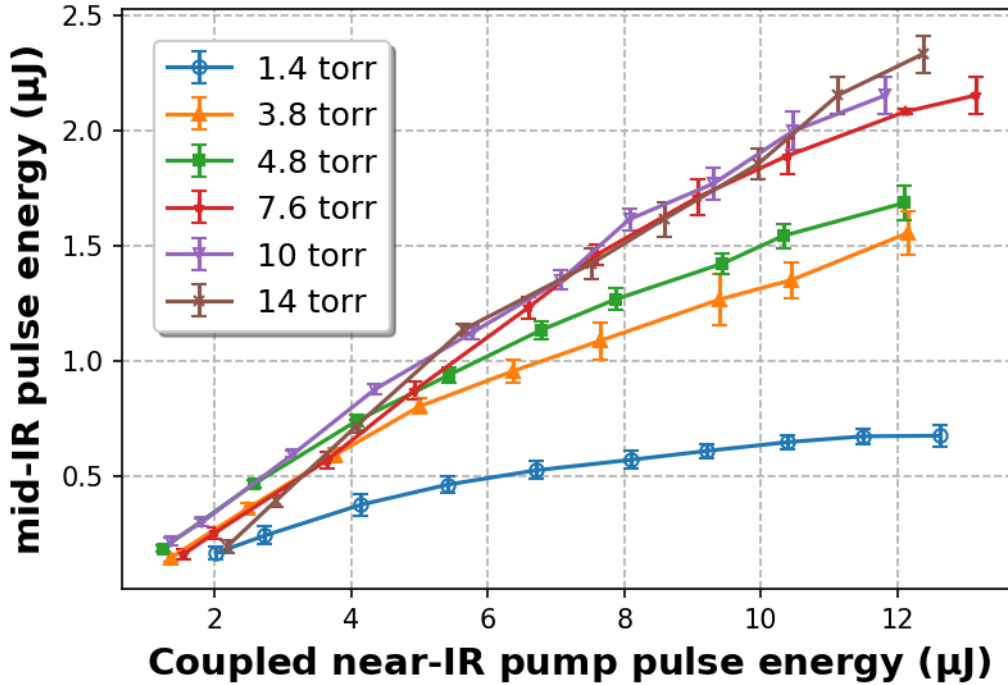


Figure 3.7 Produced mid-IR pulse energy as a function of coupled near-IR pump pulse energy into the fiber with coupling lens of focal length $f = 7.5$ cm. The portion of near-IR pump pulse energy lost due to the fiber guidance also included in the coupled near-IR pump pulse energy. Each pulse energy is obtained averaging over 500 pulses, and error bars indicate the standard deviation of each individual measurements. Acetylene molecules are pumped via P(13) absorption line.

Even though we can get some insight about the laser operation by looking at mid-IR laser output energy as a function of coupled near-IR pump pulse energy, it is critical to study the mid-IR laser output energy as a function of absorbed near-IR pump pulse energy only by acetylene molecules. The procedure described in Ref. [65] is followed to estimate the absorbed near-IR pump pulse energy only by gas. First, we need to find the actual amount of near-IR pulse energy coupled

into the fiber. According to Fig. 3.6, the input near-IR pump pulse energy E_{Pin} is measured before the BK7 lens and the BK7 window by directing the beam towards energy meter using a flipper mirror. So, the measured near-IR pump pulse energy should be multiplied by a factor of 0.99 to find the actual pump pulse energy. On the other hand, the measured mid-IR pulse energy E_{Lout} at the other side of the fiber is lower than actual produced mid-IR pulse energy due to losses that are associated with the CaF₂ window, the CaF₂ collimating lens, and the germanium filter. The respective transmission efficiencies are 88% (combined transmission efficiency for CaF₂ window and lens) and 94%. These losses are taken into account when estimating actual produced mid-IR pulse energies. The residue near-IR pump energy E_{Pout} is measured along with produced mid-IR energy in between the CaF₂ lens and Germanium filter. The actual amount is higher than the measured amount due to losses that are associated with the CaF₂ window, the CaF₂ lens, and the flipper mirror. To find out the actual amount of energy transmission efficiencies of 99% (for the flipper mirror) and 88% (for the combination of CaF₂ window and lens) are used.

After correcting the measured pulse energies, the next step is to find input and output coupling efficiencies of the fiber. We assume that any pulse energy that is just after the output end of the fiber is equal to the pulse energy that is just inside the fiber. *i.e.*, 100% output coupling is assumed for each wavelength at the output end of the fiber. As discussed earlier, off-resonance data are taken to estimate the coupling efficiency at the input end, and same coupling efficiencies are assumed for on-resonance data. To estimate the input near-IR pump coupling efficiency OPA is tuned to be off-resonance with P13 line. Then output near-IR pump energy E_{Pout} is measured for each input pump energy E_{Pin} . Since a portion of the near-IR pump pulse energy is lost due to imperfect fiber guidance, Eq. 3.1 is used to find out the actual coupled pump pulse energy. Using

Beer-Lambert law, we can write output pump pulse energy E_{Pout} in terms of coupled off-resonance pump pulse energy E'_{Pin} , fiber loss α and fiber length L as,

$$E_{Pout} = E'_{Pin} \exp(-\alpha L) \quad 3.1$$

Then the coupling efficiency, which is the ratio between E_{Pin} and E'_{Pin} equals to,

$$\text{Coupling efficiency} = \frac{E'_{Pin}}{E_{Pin}} = \frac{E_{Pout}}{E_{Pin}} \exp(\alpha L) \quad 3.2$$

Once the coupling efficiencies are estimated using off-resonance measurements, coupled on-resonance near-IR pump pulse energy. ' E_{Pcp} ' is estimated using Eq. 3.3 and no change in coupling efficiency is assumed when the OPA is tuned to on-resonance wavelength.

$$E_{Pcp} = \text{coupling efficiency} \times E_{Pin} \quad 3.3$$

The absorbed near-IR pump pulse energy E_{Pabs} can be written as,

$$E_{Pabs} = E_{Pcp} - E_{Pout} - E_{Pfiber} \quad 3.4$$

where, E_{Pfiber} is the amount of near-IR pump pulse energy that is lose due to imperfect fiber guidance. In Eq. 3.4 all the quantities are measured when the OPA is on-resonance with P13 absorption line. The quantity E_{Pfiber} fiber can be written as,

$$E_{Pfiber} = E_{Pcp} (1 - \exp(-\alpha L)) \quad 3.5$$

Substituting this into Eq. 3.4 we have,

$$E_{Pabs} = E_{Pcp} \exp(-\alpha L) - E_{Pout} \quad 3.6$$

Then the absorbed near-IR pump pulse energy only by gas is estimated using Eq. 3.6 along with Eq. 3.3.

Since the acetylene gas does not absorb the near-IR pump energy linearly but non-linearly, the estimated amount of near-IR pulse energy using Eq. 3.6 is an overestimation. To overcome this, absorbed pump energy only by gas is calculated following two routes through the fiber and finally, outcomes are averaged to get the absorbed pump pulse energy. In the first route, the coupled near-IR pump pulse energy is used to estimate the output pump pulse energy by assuming there are no acetylene molecules in the fiber. The absorbed near-IR pump energy only by gas is obtained by taking the difference between the estimated output pump energy and the measured residue output near-IR pump energy at a given acetylene gas pressure. In the second route, the measured on-resonance residual pump pulse energy at the output end of the fiber is used to estimate the coupled pump pulse energy at the input fiber end. The difference between estimated and measured values is used as the absorbed near-IR pump pulse energy and the average between both routes is used as the final estimated absorbed near-IR pump pulse energy. Figure 3.8 explains these two routes more clearly.

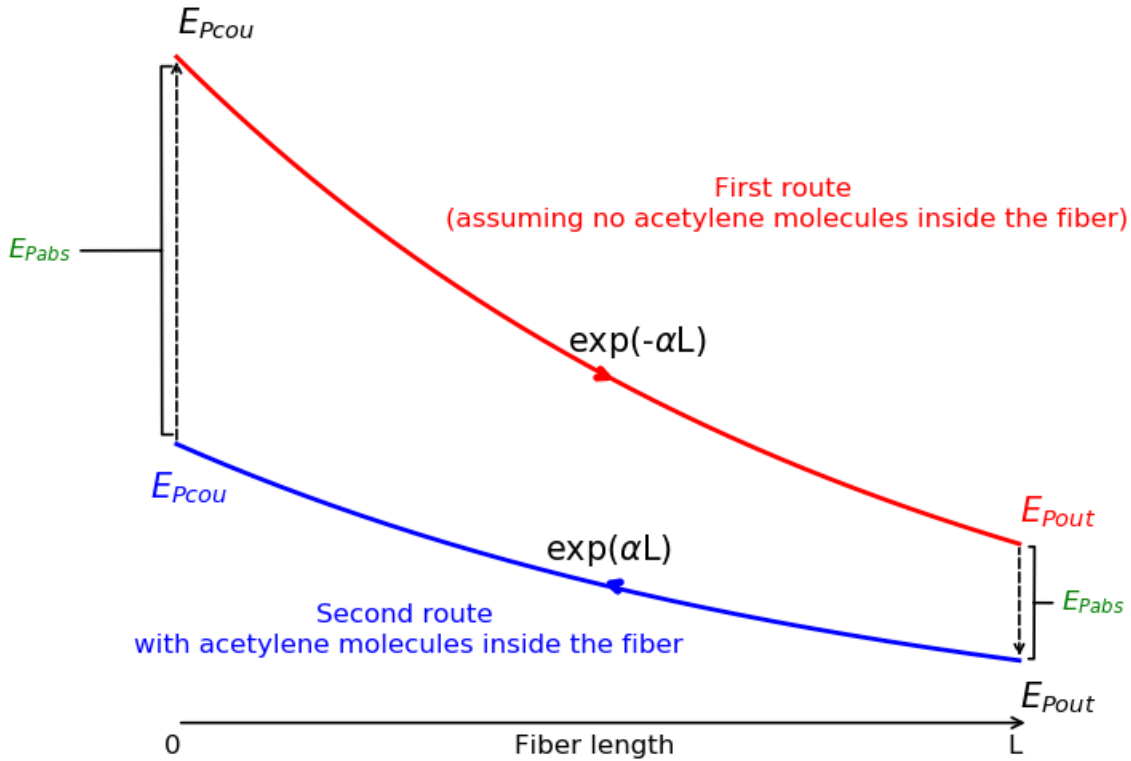


Figure 3.8 The summary of two calculation routes to estimate the near-IR pump pulse energy only by acetylene gas. The blue, red and green text stand for estimated values using measured data and the black color quantities are experimentally measured values. The average value between two routes is taken, to estimate the absorbed near-IR pump pulse energy only by acetylene gas.

Once the absorbed near-IR energy only by gas is estimated as above, the produced mid-IR energy is plotted as a function of absorbed near-IR pulse energy and shown in Fig. 3.9. The mid-IR laser output does not show laser signal saturation like effect for most of the acetylene gas pressures. At the lowest acetylene gas pressure mid-IR laser output still shows signal saturation like effect reflecting a limited number of absorbers inside the fiber. However, at other acetylene gas pressures, mid-IR laser output increases with the increase of absorbed near-IR pump pulse energy. This behavior is an encouragement for power scaling the acetylene filled HOFGLAS system. The near-IR pump energy of 9.9 μJ is absorbed by acetylene molecules at 14 torr to

produce the maximum mid-IR pulse energy of 2.33 μJ . The maximum optical-to-optical efficiency of 28% is obtained with acetylene gas pressure of 7.6 torr.

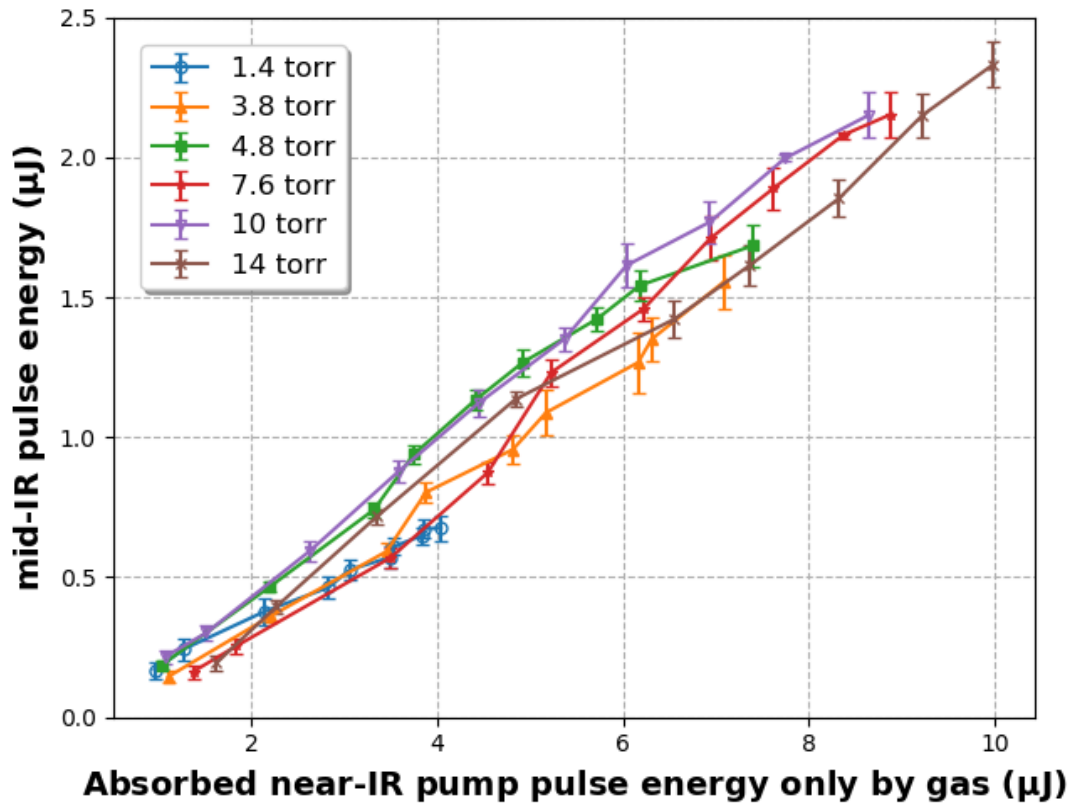


Figure 3.9 Mid-IR laser output energy as a function of estimated absorbed pump pulse energy only by acetylene molecules at a given pressure. Acetylene molecules are excited via P(13) absorption line. Each pulse energy is obtained averaging over 500 pulses, and error bars indicate the standard deviation of each individual measurements.

Figure 3.10(a) shows the measured highest mid-IR pulse energy at each acetylene pressure as a function of gas pressure inside the fiber. The mid-IR laser output pulse energy initially increases with acetylene gas pressure and then saturates at higher pressures. Since the produced mid-IR energy depends on the absorbed near-IR pump energy by acetylene molecules, it is crucial to look at the absorbed near-IR pump pulse energy as a function of acetylene gas pressure. As shown in Fig.3.10 (b), the absorbed near-IR pump pulse energy only by acetylene gas shows similar behavior as the mid-IR pulse energy.

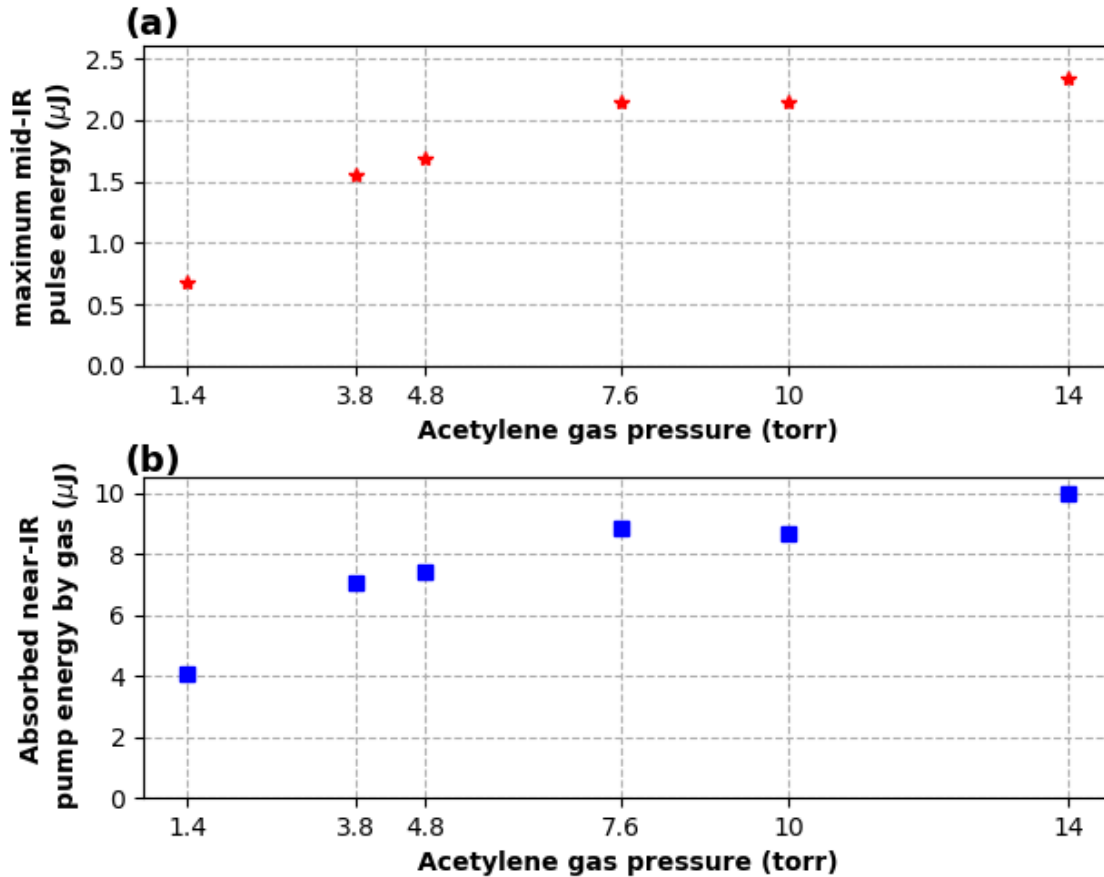


Figure 3.10 Maximum mid-IR pulse energy (a) and absorbed maximum near-IR pump pulse energy only by acetylene gas (b) as a function of acetylene gas pressure inside the fiber. Acetylene molecules are pumped with P(13) absorption line. Maximum coupled near-IR pump pulse energy $\sim 12.5 \mu\text{J}$.

The amount of output mid-IR pulse energy depends on the population inversion of the lasing transition and to achieve the population inversion acetylene molecules should absorb the near-IR pump energy. The main reason for this observation is the pump saturation. The amount of absorbed near-IR pump energy by acetylene molecules depends on the overlapping between OPA linewidth and the absorption line width of acetylene P(13) line. The OPA linewidth has FWHM of $\sim 440 \text{ MHz}$ based on the time-bandwidth product for Gaussian shaped pulse. The FWHM of the acetylene P(13) line depends preliminarily on the temperature and the gas pressure. Due to the room

temperature (22 °C) acetylene P(13) absorption line is Doppler broadened by ~ 475 MHz and it gets pressure broadened by ~ 11 MHz/torr [36] on top of that. Due to this, the overlapping between OPA linewidth and the absorption linewidth will be limited as the gas pressure is increased. Also, the absorption line profile for acetylene P(13) line is a Voigt profile at higher acetylene pressures (> 1 torr). Voigt profile is an area normalized as a function of frequency. The amplitude of the function should decrease to preserve the area under the Voigt profile since the linewidth gets broader as the pressure increases. Due to these effects, the amount of near-IR energy absorbed by acetylene molecules will saturate with the increase of pressure and therefore produced mid-IR energy will also saturate as the gas pressure increases.

Figure 3.11 shows the laser optical-to-optical conversion efficiency as a function of acetylene gas pressure inside the fiber. The optical-to-optical conversion efficiency ‘ η ’ is found by fitting each data set in Fig. 3.9 to the linear function as in Eq. 3.7.

$$E_{Lout} = \eta \times E_{Pabs} + E_{Thr} \quad 3.7$$

where, E_{Thr} is the threshold value of the near-IR pump absorption to start the lasing.

In comparison with Fig. 3.10 (a), the laser optical-to-optical conversion efficiency shows similar behavior as a function of gas pressure. The optical-to-optical conversion efficiency is stable at 25% except for the lowest gas pressure. This behavior suggests that the laser output is not limited by the collisional relaxations at the higher gas pressures but the fiber loss at lasing wavelength.

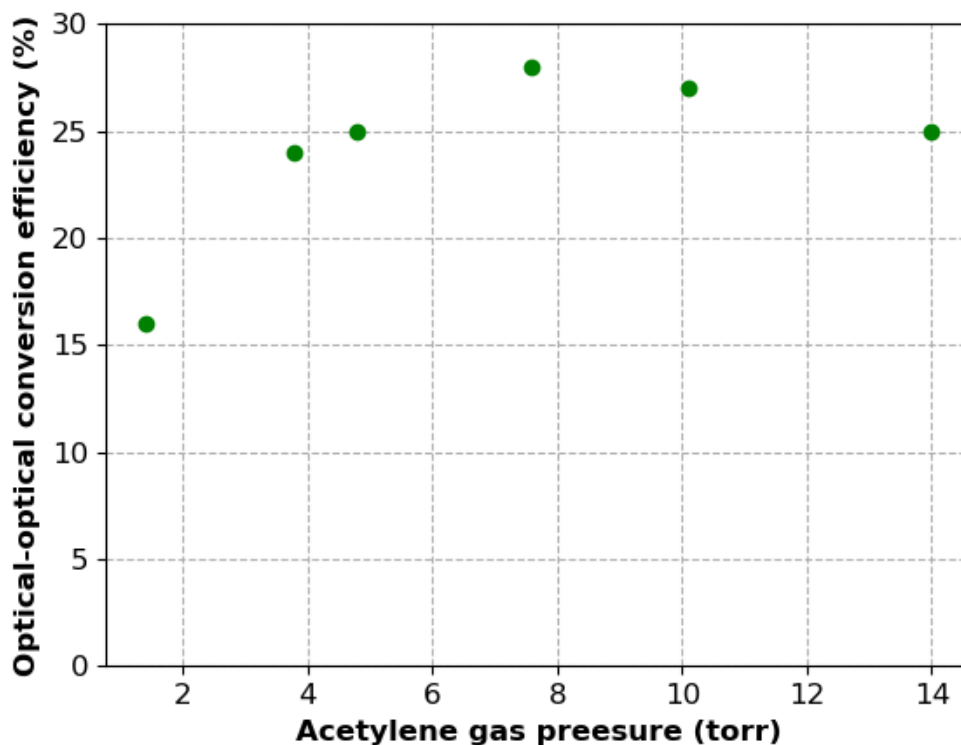


Figure 3.11 Laser's optical-to-optical conversion efficiency as a function of acetylene gas pressure inside the fiber. Acetylene molecules are excited via P(13) absorption line.

At the lowest gas pressure, the estimated optical-to-optical conversion efficiency is only 16%. One reason for this could be that the gain attained at this lower gas pressure due to the population inversion is not as large as gain attained at higher gas pressures. Then, whatever gain attained with population inversion is mostly reduced by fiber loss at lasing wavelength resulting in lower optical-to-optical conversion efficiency. If we look at Fig. 3.4 the simplified version of laser energy level diagram, once the acetylene molecules made radiative transitions into $J = 13$ or $J = 11$ rotational states of the ν_1 vibrational manifold the transitions into the vibrational ground state are not allowed by dipole-selection rules. In order to depopulate the ν_1 vibrational manifold, acetylene molecules must lose their energy through collisions either with other acetylene molecules or with fiber wall. If the gas pressure is low, then the available molecules for collisions to happen could be limited and hence creates a bottleneck condition to the lasing transition. Then

acetylene molecules in the $\nu_1 + \nu_3$ vibrational state will not participate in the lasing transition effectively, and they will undergo non-radiative transitions to vibrational ground. This could limit the laser output energy and the optical-to-optical conversion efficiency by a significant amount. Furthermore, this might be the main underline reason for the laser signal saturation like effect observed at lower acetylene gas pressure in this work and the previous works [60, 65]. Even though one would expect to see a 33% optical-to-optical conversion efficiency out from the acetylene filled HOFGLAS system, the maximum conversion efficiency obtained with this work is 28%. In contrast, Wang *et al.*[23] were able to obtain 30% conversion efficiency by using a 10.5 m long anti-resonant hollow-core fiber with lower fiber loss at the pump (0.11 dB/m at 1530 nm) and lasing wavelength (0.1 dB/m at 3.1-3.2 μm) in diode-pumped acetylene filled HOFGLAS system. These suggest that the output of our laser system is mainly limited by the fiber loss at the lasing wavelength and suggests that the fiber length is not optimized for optimum laser output.

3.3 Effect of the pump wavelength

The diode-pumped acetylene filled HOFGLAS system demonstrated by Wang *et al.* [23] was pumped at a wavelength of 1530.37 nm. Moreover, this wavelength corresponds to the P(9) absorption line of acetylene. More details about this laser system were discussed in section 1.1. By using a 10.5 m long anti-resonant hollow-core fiber in the setup, the authors were able to obtain 30% optical-optical conversion efficiency and furthermore, they did not see any laser signal saturation like effect for any gas pressure that was studied. In contrast to our work, they obtained the highest mid-IR pulse energy and the optical-to-optical conversion efficiency at a lower acetylene gas pressure (0.53 torr), whereas we obtained the highest mid-IR energy and the optical-optical to conversion efficiency at relatively higher-pressure regime (7.5 – 14 torr). The line

strength for P(9) absorption line is $1.211 \times 10^{-20} \text{ cm}^{-1}/(\text{molecules cm}^{-2})$ and it is slightly higher than the line strength $=1.035 \times 10^{-20} \text{ cm}^{-1}/(\text{molecules cm}^{-2})$ for P(13) absorption line [38]. Because of this, pumping the acetylene filled HOFGLAS system via the P(9) line can be an efficient route with lower gas pressure in order to reduce the intermolecular collisions and thereby increase the mid-IR laser output and the optical-to-optical conversion efficiency. To study this hypothesis, we decided to pump our acetylene filled HOFGLAS system via the P(9) absorption line.

3.3.1 Experimental results and discussion

To pump the acetylene filled HOFGLAS system with P(9) absorption line, the OPA signal output is tuned to be on-resonance with P(9) line by tuning the tunable diode laser wavelength $\sim 1530.37 \text{ nm}$. Then, the same experimental procedure described in the previous section is followed to obtain the mid-IR pulse energy as functions of coupled near-IR pump pulse energy and absorbed near-IR pump pulse energy only by acetylene gas. Same pressure regime as in the previous section is studied to make a better comparison between the two methods.

A simplified version of the laser energy level diagram is depicted in Fig. 3.12. Initially, all the energy levels are populated according to the Boltzmann distribution. When the acetylene molecules are pumped via the P(9) line, they can absorb near-IR pump energy and make transitions from $J = 9$ rotational state of the vibrational ground state to the $J = 8$ rotational state of $\nu_1 + \nu_3$ the vibrational state. Then, if the population in $J = 8$ rotational state of $\nu_1 + \nu_3$ vibrational manifold is larger than the population in the ν_1 vibrational manifold, acetylene molecules can make radiative transitions to $J = 9$ or $J = 7$ rotational states of the ν_1 vibrational manifold, and these transitions are governed by the dipole selection rule $J = \pm 1$. Based on the spectroscopic notations these transitions are named as P(9) and R(7), and the previous studies have measured the corresponding

wavelengths to be 3.16 μm and 3.12 μm respectively [23, 26, 28, 29]. Once acetylene molecules are in the ν_1 vibrational state, they cannot spontaneously go into the vibrational ground state since that transition is forbidden. So, molecules will go into vibrational ground state by losing energy via intermolecular and fiber-wall collisions.

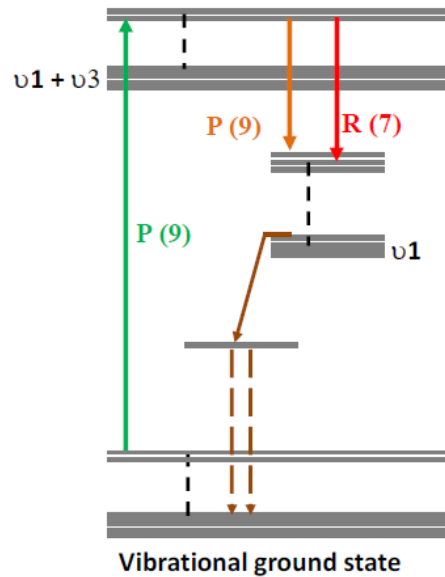


Figure 3.12 Simplified ro-vibrational energy level diagram of acetylene. The lasing wavelengths 3.12 μm and 3.16 μm correspond to the R(7) and P(9) transitions when pumped via P(9) line.

Figure 3.13 shows the produced mid-IR pulse energy as a function of coupled near-IR pump pulse energy. The maximum coupled near-IR energy into the hollow-core fiber is around 13 μJ . As in the previous section the mid-IR laser output pulse energy shows laser signal saturation like effect at the lowest gas pressure and does not show signal saturation like effect at higher acetylene gas pressures. We were able to obtain the highest mid-IR pulse energy of 2.56 μJ at 13.8 torr, and this is the highest mid-IR pulse energy ever achieved by acetylene filled HOFGLAS system to best of our knowledge. The maximum overall laser efficiency of 21% is obtained with

the gas pressure of 13.8 torr, and this is slightly higher than the overall laser efficiency obtained with pumping via P(13) line.

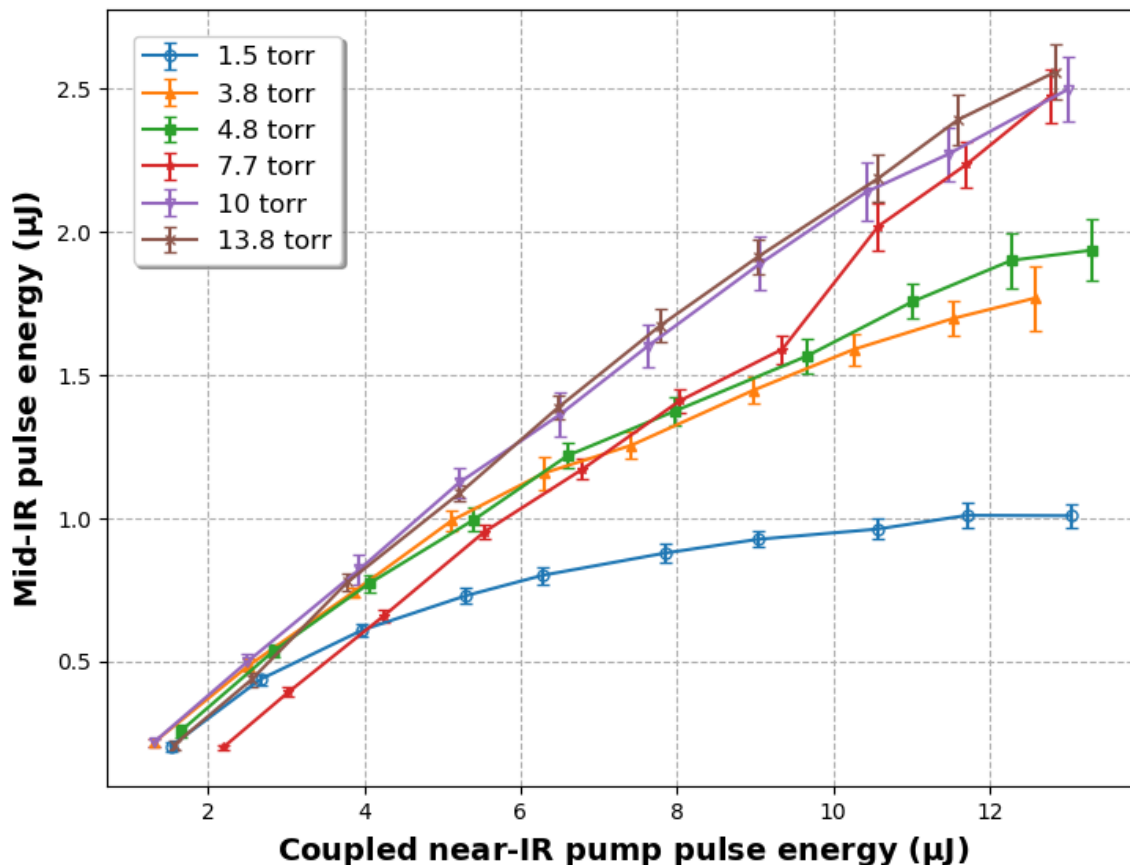


Figure 3.13 Produced mid-IR pulse energy as a function of coupled near-IR pump pulse energy into the fiber with coupling lens of focal length $f = 7.5$ cm. The portion of near-IR pump pulse energy lost due to the fiber guidance also included in the coupled near-IR pump pulse energy. Each pulse energy is obtained averaging over 500 pulses, and error bars indicate the standard deviation of each individual measurements. Acetylene molecules are pumped via P(9) absorption line.

As discussed in Section 3.2.1, the absorbed near-IR pump pulse energy only by the gas is calculated to study the mid-IR laser output pulse energy as a function of absorbed near-IR pump pulse energy only by acetylene gas. Figure 3.14 shows the produced mid-IR pulse energy as a function of absorbed near-IR pump pulse energy. The mid-IR laser output still shows laser signal

saturation like effect at lowest pressure reflecting the limited pump absorption. This behavior is another indication that the number of absorbers at lowest pressure is not enough to effectively absorb the near-IR pump pulse energy. However, at all the other gas pressures the mid-IR pulse energy increased linearly with the absorbed near-IR pump pulse energy only by gas. This behavior reveals the power scalability of acetylene filled HOFGLAS system.

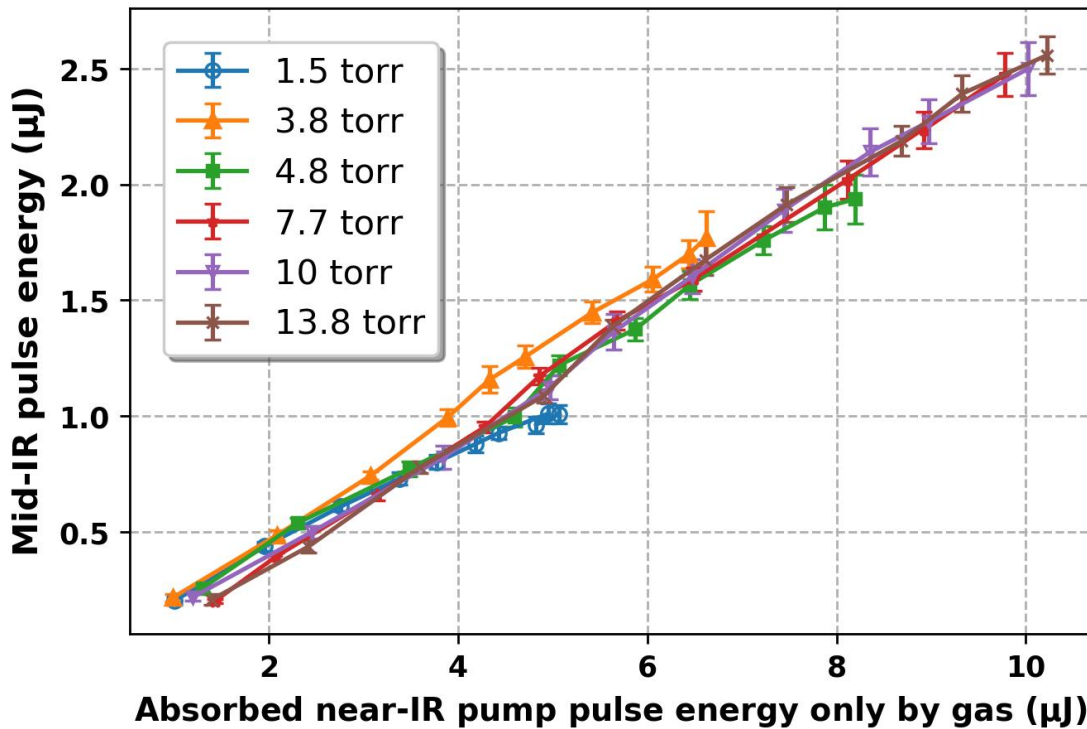


Figure 3.14 Mid-IR laser output energy as a function of estimated absorbed pump pulse energy only by acetylene molecules at a given pressure. Acetylene molecules are excited via P(9) absorption line. Each pulse energy is obtained averaging over 500 pulses, and error bars indicate the standard deviation of each individual measurements.

To have a better understanding of the laser dynamics, the maximum produced mid-IR energy and maximum absorbed near-IR pump pulse energy are plotted as a function of acetylene gas pressure inside the fiber. These results are illustrated in Fig 3.15 (a) and (b) respectively. In comparison to laser operation with P(13) absorption line, similar behavior is observed for mid-IR pulse energy and absorbed near-IR pump energy as a function of gas pressure. This similar type

of behavior was explained in Section 3.2.1. Again, as with pump via P(13) line primary cause for this observation is the pump saturation as explained in Section 3.2.1.

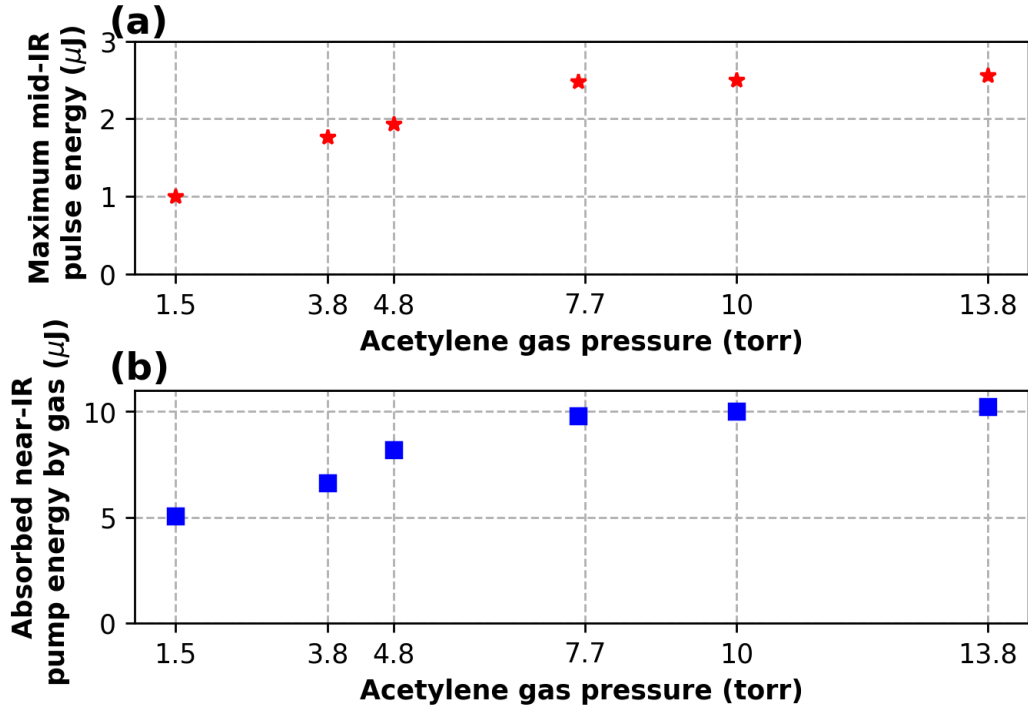


Figure 3.15 Maximum mid-IR pulse energy (a) and absorbed maximum near-IR pump pulse energy only by acetylene gas (b) as a function of acetylene gas pressure inside the fiber. Acetylene molecules are pumped with P(9) absorption line. Maximum coupled near-IR pump pulse energy $\sim 13 \mu\text{J}$.

Furthermore, we observed slightly higher near-IR pump absorption and output mid-IR energy with pumping via P(9) absorption line. This is mainly due to the slightly higher line strength of P(9) line than that of P(13) line. Figure 3.16 shows the overall optical-to-optical laser conversion efficiency as a function of acetylene gas inside the fiber. As in Fig. 3.11, Fig. 3.16 shows the similar behavior where the optical-to-optical conversion efficiency is almost the same for all the pressure except the lowest pressure. This is a strong indication that laser operation is not limited by intermolecular collisions and most of the excited acetylene molecules relax through the radiative transition.

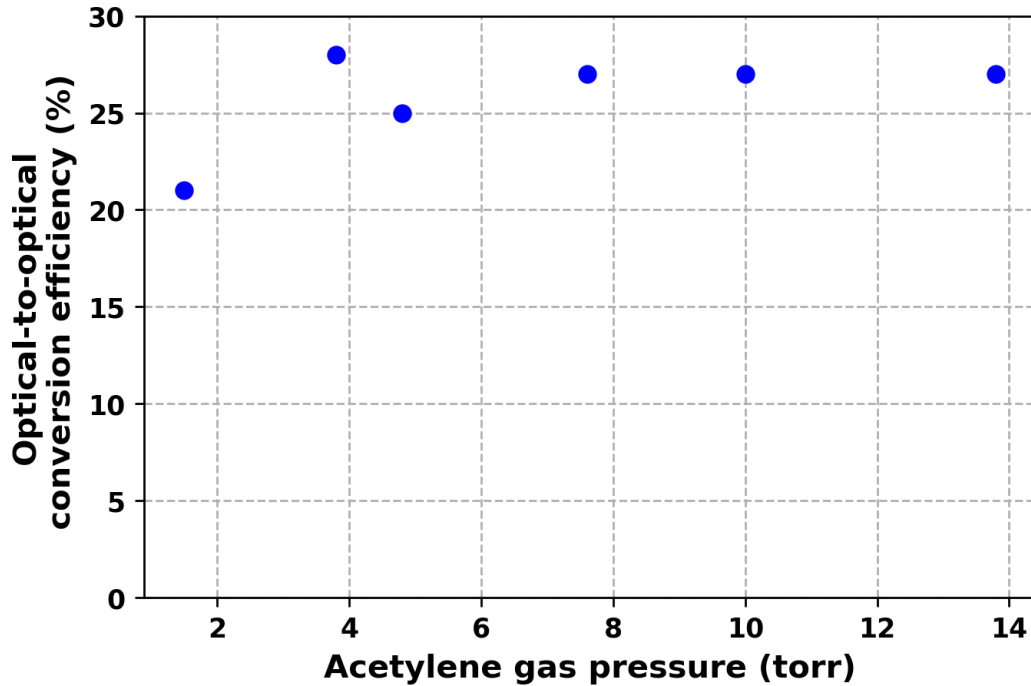


Figure 3.16 Laser's optical-to-optical conversion efficiency as a function of acetylene gas pressure inside the fiber. Acetylene molecules are pumped at P(9) absorption line.

By choosing the P(9) absorption line as the pumping line we obtained the highest optical-to-optical conversion efficiency of 27%. Even though we pumped the acetylene filled HOFGLAS system with a stronger absorption line, we could not obtain the maximum theoretical limit optical-to-optical conversion efficiency of 33%. This is mainly due to fiber loss at the lasing wavelength. Regardless of that we successfully removed the laser signal saturation like effect observed in the previous system, and this gives us the opportunity to scale the mid-IR laser output into higher energies. By comparing the laser performance with that of pumping with P(13) line, we can say that pump wavelength does not effect on the laser performance significantly in the studied pressure regime. At the moment mid-IR laser output pulse energy is only limited by the available near-IR pump pulse energy and a newer pump source is needed to scale the system to higher pulse energies. In order to power scale and to study about the current acetylene filled HOFGLAS system we designed and built a new near-IR pump source and more details will be discussed in Chapter 6.

3.4 Effect of pump pulse duration on laser performance

Figure 3.17 shows the optical-to-optical conversion efficiencies for diode-pumped HOFGLAS configuration in Ref. [23], and optical-to-optical conversion efficiencies for our OPA pumped HOFGLAS configuration when pumped at P(9). Even though Wang *et al.* used a lower loss fiber in the HOFGLAS system, the laser's optical-to-optical conversion efficiency decreases with pressure from 30% to 8% while our HOFGLAS system's conversion efficiency remains the same around 25%. This is a stronger indication that the performance of our HOFGLAS system is not limited by collisional relaxation whereas HOFGLAS system reported in Ref. [23] is limited by collisional relaxation.

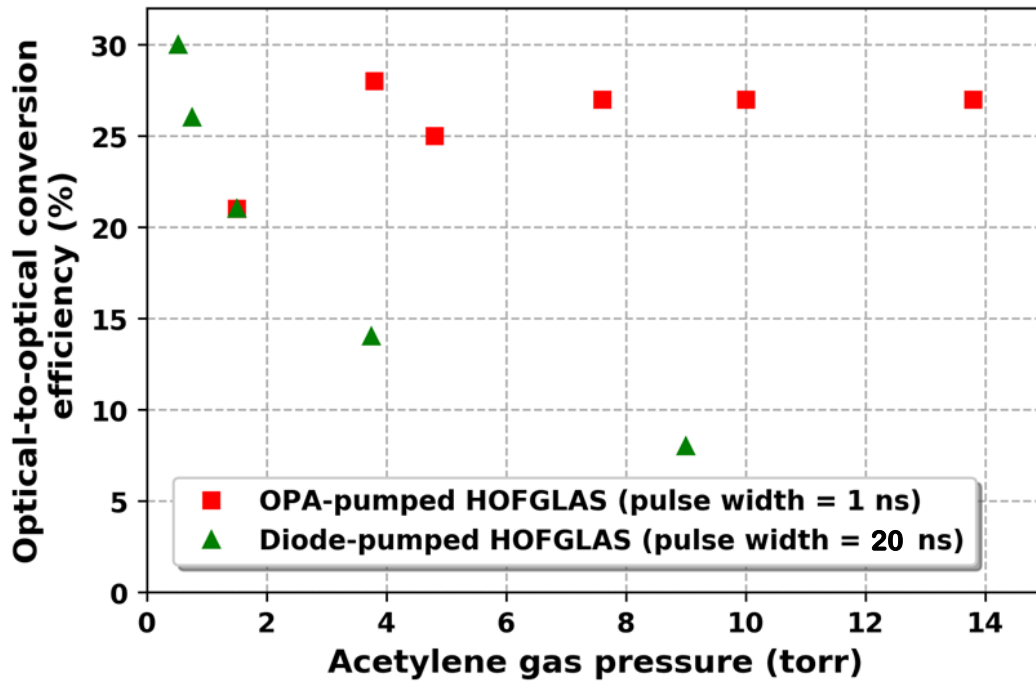


Figure 3.17 The optical-to-optical conversion efficiency as a function of gas pressure compared for an OPA pumped acetylene filled HOFGLAS system with the pump pulse duration of 1 ns and a diode-pumped HOFGLAS system with the pump pulse duration of 20 ns.

To understand the above-mentioned behavioral difference between two systems, we need to compare the respective pump pulse widths with the mean collisional times of acetylene molecules. To estimate the mean collisional times, we calculated the mean free path of acetylene for the pressure region of 0.1 torr to 15 torr. Assuming acetylene is an ideal gas, the mean free path ‘*MFP*’ can be written in terms of gas pressure *P*, molecular diameter *d*, Boltzman constant *k_B*, and room temperature *T* as in Eq.3.8.

$$MFP = \frac{k_B T}{\sqrt{2} \pi d^2 P} \quad 3.8$$

To calculate the *MFP*, *d*=330 pm is used as the molecular diameter of acetylene (11), and *T*=293.15 K is used as the room temperature. The calculated *MFP* values are depicted in Fig. 3.18 as a function of gas pressure.

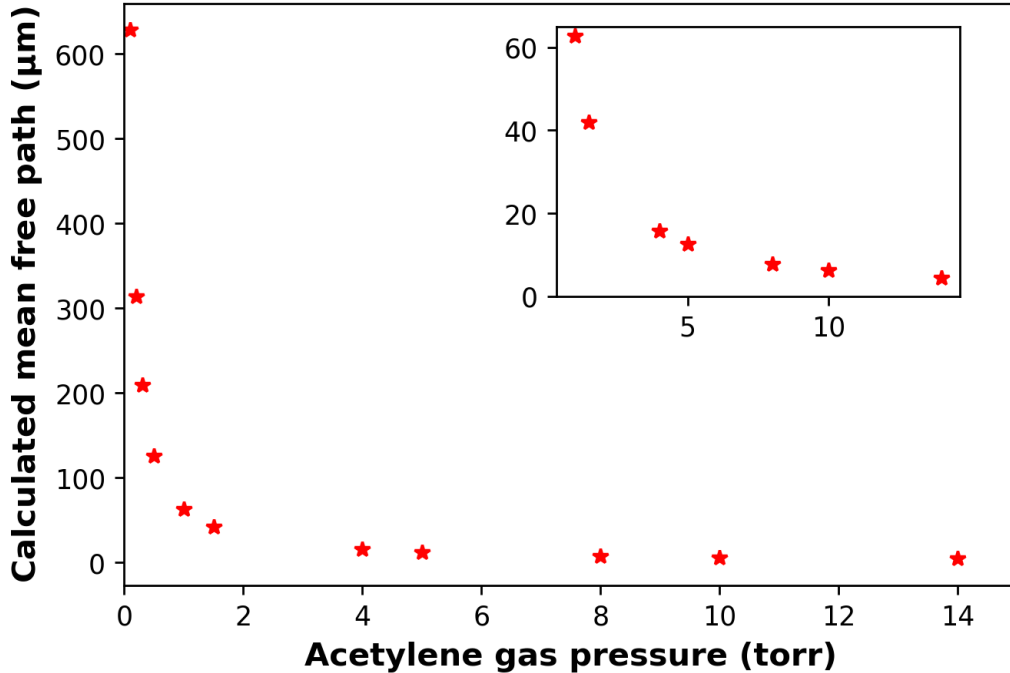


Figure 3.18 The calculated mean free paths for pressure region 0.1 torr to 14 torr as a function of acetylene gas pressure. Inset shows the calculated mean free paths for acetylene pressure form 1 torr to 14 torr.

The fiber used in the Ref. [23] has a diameter of 109 μm . The calculated mean free paths for pressures below one torr are higher than 100 μm , and so the contributions from wall collisions will be an effect on the laser performance. Moreover, the calculated mean free paths for pressures above 2 torr are $< 50 \mu\text{m}$ and are smaller than the fiber diameters in both setups. So the intermolecular collisions should dominate the laser performances. However, as per Fig. 3.17 only diode-pumped HOFGLAS system's efficiency is degraded at higher gas pressures. This suggests that merely the calculated MFP is not enough to study the effect of collisions on the laser performance and we need to compare the pulse widths with the mean collisional times. Assuming acetylene molecules travel with a mean velocity of $\bar{v} = \sqrt{\frac{8RT}{\pi M}}$ we can calculate the mean intermolecular collisional time τ_{mean} as follows.

$$\tau_{mean} = \frac{MFP}{\bar{v}} \quad 3.9$$

At room temperature of 20 °C acetylene molecule ($M = 26 \text{ g/mole}$) has mean velocity of 488 m/s. Using this value along with $MFPs$, τ_{mean} is calculated for pressure region of 0.1 torr to 14 torr, and the calculated τ_{mean} as a function of acetylene gas pressure is plotted in Fig. 3.29. Intermolecular collisional time scale will be comparable with pump pulse width when the pressure is increasing. In the diode-pumped HOFGLAS system acetylene molecule would take $\sim 220 \text{ ns}$ to collide with fiber wall, and $\sim 600 \text{ ns}$ to collide with another acetylene molecule at low pressure limit. These time scales are much larger than the pump pulse width (20 ns) and lasing transition is more favorable at low pressure limit than the collisional relaxations. But when the acetylene gas pressure is larger than 2 torr mean intermolecular collisional time scale is comparable with the pump pulse width and excited molecules will tend to relax via intermolecular collisions than the

lasing transition. Therefore, laser's optical-to-optical conversion efficiency will decrease as the gas pressure increases.

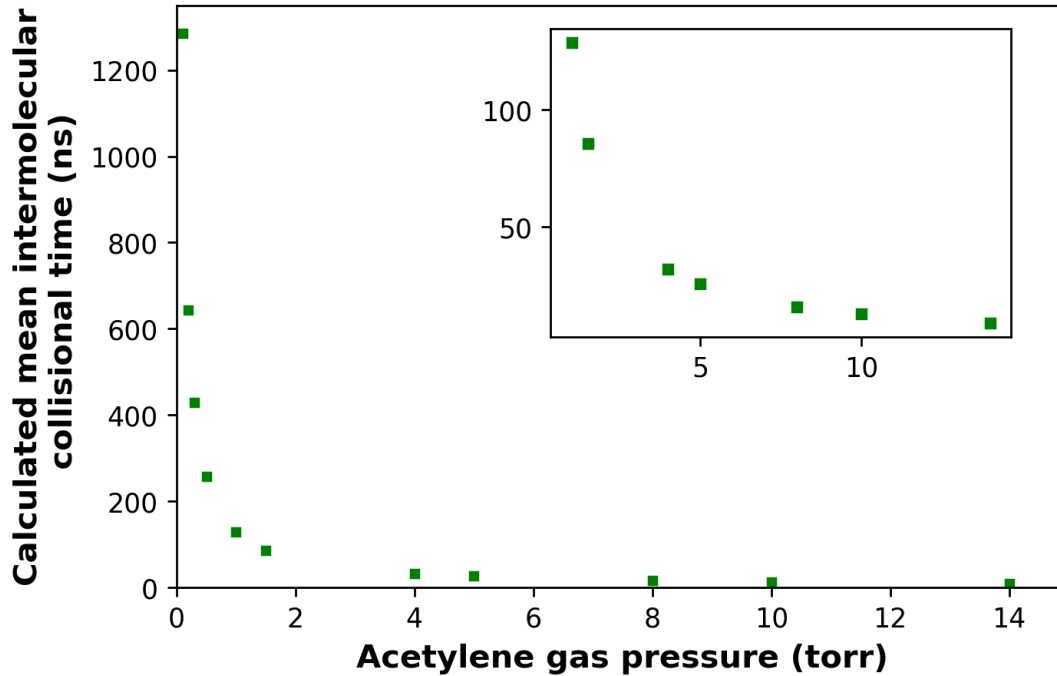


Figure 3.19 The calculated mean intermolecular collisional time as a function of acetylene gas pressures. Inset zoomed in to the pressure region of 1-14 torr.

In OPA pumped HOFGLAS system acetylene molecule would take ~ 15 ns to collide with fiber wall and the mean intermolecular collisional times are larger than 9 ns in the studied gas pressure region (1 – 14 torr). Since the OPA has a pulse width of 1 ns, excited acetylene molecule is more favorable to make a lasing transition than collisional relaxation. Therefore, one would expect to see a constant optical-to-optical conversion efficiency in the gas pressure region of 1- 14 torr. Then we can conclude that higher gas pressures are suitable for shorter pump pulses to utilize the pump energies effectively, and lower gas pressures are appropriate for longer pump pulses to use the pump energies efficiently.

Chapter 4 - Mode quality of acetylene filled HOFGLAS system

The transverse mode quality (also known as beam quality) of a laser is an important factor when characterizing the laser specifications. It describes the laser beam divergence while propagating in space and the power (intensity) distribution across the beam. Also, mode quality indicates how tightly one can focus the laser beam to attain a high intense field. Therefore, the mode quality of a high-power laser system is critical factor in applications where the free space laser beam delivering is involved. Moreover, the mode quality is a significant factor for coherent beam combining, which is a technique of achieving higher laser power by combining multiple beams [66]. The most common way to quantify the laser mode quality is the M^2 factor. It is a measure of how close the beam profile is to an ideal single-mode Gaussian beam (diffraction-limited). The value $M^2 \geq 1$ for any arbitrary laser beam. $M^2 = 1$ is for the single-mode TEM₀₀ (Gaussian beam) beam, while non-Gaussian beams have $M^2 \geq 1$ and describe the multi-mode property of the beam [67]. Mode quality depends on the coupling between the laser's cavity modes and the free space modes. The non-ideal beam quality depends on the coupling of higher order modes which depends on the cavity geometry and the wavefront distortion. The wavefront can get distorted due to several reasons. To name a few, spherical aberrations due to lenses, diffraction at output laser head, and thermal effects in a gain medium.

To quantify the mode quality of our acetylene filled mid-IR HOFGLAS system, we performed M^2 measurement based on the finite slit method [68], experimental procedure and results will be discussed in following sections. Some of the work presented here is published in Ref. [27] and this is a collaborative work with Dr. Neda Dadashzadeh.

The M^2 value indicates the transverse modal content of a laser beam, and the modal content depends on the geometry of the laser cavity. Therefore, one must understand the possible modal

content for a given cavity geometry to obtain a better beam quality. Since we use a core of the hollow-core fiber as the waveguide, it is important to discuss the possible modal content for the core of the hollow-core fiber. Ultimately, the M^2 value depends on the coupling between cavity modes and the free space modes. Therefore, the properties of free space modes also will be discussed in following sections.

4.1 Free space propagation modes

Starting from Maxwell's equations, we can write the wave equations for electric field \vec{E} and magnetic field \vec{H} for free space (no bound charges or currents) as [42],

$$\nabla^2 \vec{E} - \mu_0 \epsilon_0 \frac{\partial^2 \vec{E}}{\partial t^2} = 0 \quad 4.1$$

$$\nabla^2 \vec{H} - \mu_0 \epsilon_0 \frac{\partial^2 \vec{H}}{\partial t^2} = 0 \quad 4.2$$

where, ϵ_0 and μ_0 are free space permittivity and free space permeability respectively and the quantity $1/\mu_0 \epsilon_0$ equals to the c^2 (where c is the speed of light in vacuum). Both Eq. 4.1 and Eq. 4.2 have the same format. One can solve one equation and can use the same analogy to solve other equation. Therefore, we will only consider the electric field propagation in the medium. Assuming the electric field oscillates with frequency ω , we can write \vec{E} in Cartesian coordinates system as,

$$\vec{E} = \vec{E}(x, y, z)e^{-i\omega t} \quad 4.3$$

then along with $\frac{\omega^2}{c^2} = k^2$ Eq. 4.1 can be written as,

$$\nabla^2 \vec{E} + k^2 \vec{E} = 0 \quad 4.4$$

Choosing z as the propagation direction, we can write electric field as,

$$\vec{E}(x, y, z) = \varphi(x, y, z) \exp(-ikz) \quad 4.5$$

Then, Eq. 4.4 is reduced to following scalar equation.

$$\frac{\partial^2 \varphi(x, y, z)}{\partial x^2} + \frac{\partial^2 \varphi(x, y, z)}{\partial y^2} - 2ki \frac{\partial \varphi(x, y, z)}{\partial z} + \frac{\partial^2 \varphi(x, y, z)}{\partial z^2} = 0 \quad 4.6$$

For an optical beam, the wavenumber k is a large value. So, the term $2ki \frac{\partial \varphi(x, y, z)}{\partial z}$ is larger than the term $\frac{\partial^2 \varphi(x, y, z)}{\partial z^2}$ and we can simply neglect the later term. This approximation called as the paraxial approximation and finally, we end up with the paraxial equation.

$$\frac{\partial^2 \varphi(x, y, z)}{\partial x^2} + \frac{\partial^2 \varphi(x, y, z)}{\partial y^2} - 2ki \frac{\partial \varphi(x, y, z)}{\partial z} = 0 \quad 4.7$$

One can show that the lowest-order spherical Gaussian wave is a solution to the Eq. 4.7 [69]. With a complex radius of curvature $q(z)$, the spherical Gaussian wave can be written as,

$$\varphi(x, y, z) = \frac{1}{q(z)} \exp \left[-ik \frac{x^2 + y^2}{2R(z)} - \frac{x^2 + y^2}{w^2(z)} \right] \quad 4.8$$

where, $R(z)$ is the radius of curvature and $w(z)$ is the beam spot size. The Eq. 4.8 describes the divergence of a spherical wave along the propagation distance z . Therefore, it is important to discuss about the Gaussian beam propagation in free space. Let us assume that the lowest-order Gaussian beam has a beam size of w_0 and a planar wavefront $R_0 = \infty$ at $z = 0$. Figure 4.1 shows

the divergence of this beam with all the relevant quantities. The normalized Gaussian wave at any arbitrary position z can be written as follows [69].

$$\varphi(x, y, z) = \left(\frac{2}{\pi}\right)^{1/2} \frac{\exp[-ikz + \phi(z)]}{w(z)} \exp\left[-ik \frac{x^2 + y^2}{2R(z)} - \frac{x^2 + y^2}{w^2(z)}\right] \quad 4.9$$

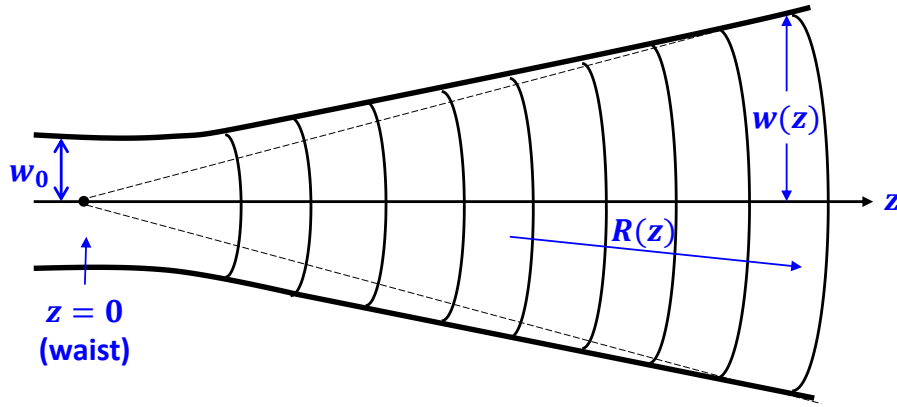


Figure 4.1 Divergence of lowest order Gaussian beam.

Then the beam width $w(z)$, the radius of curvature $R(z)$, and the additional axially varying phase shift $\phi(z)$ (which also called as Gouy phase) can be written as,

$$w(z) = w_0 \sqrt{1 + \left(\frac{z}{z_R}\right)^2} \quad 4.10$$

$$R(z) = z + \frac{z_R^2}{z} \quad 4.11$$

$$\phi(z) = \tan^{-1}\left(\frac{z}{z_R}\right) \quad 4.12$$

where, the quantity $z_R = \frac{\pi w_0^2}{\lambda}$ is the Rayleigh range. As shown in Fig. 4.2, Rayleigh range is the distance from beam waist to the point where the beam size equal to the $\sqrt{2}w_0$.

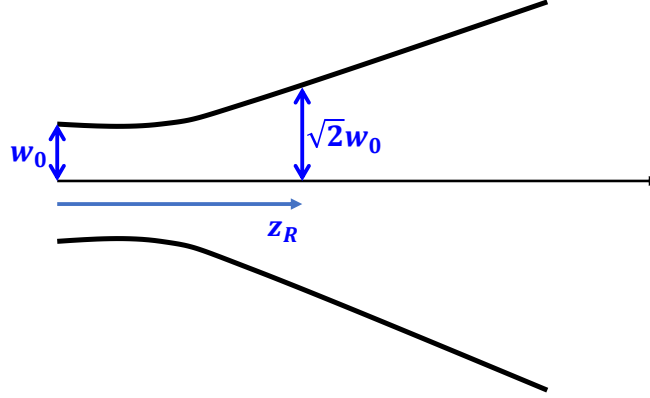


Figure 4.2 Rayleigh range of a Gaussian beam.

While spherical Gaussian wave is the lowest order propagation mode in free space, one can find higher propagation modes by solving Eq. 4.7. The higher order solutions to the Eq. 4.7 can be either Hermite-Gaussian functions or Laguerre-Gaussian functions. If the Eq. 4.7 solved in Cartesian coordinates system one would obtain Hermite-Gaussian functions as the solutions, while Laguerre-Gaussian functions for the cylindrical coordinates system.

4.1.2 Higher-order propagation modes in Cartesian coordinates

To solve the Eq. 4.7 in the Cartesian coordinate system, we assume that the solution can write as a product of two identical functions as follows [69].

$$\varphi_{n,m}(x, y, z) = \varphi_n(x, z)\varphi_m(y, z) \quad 4.13$$

where, n and m stand for the order of modes, $\varphi_n(x, z)$ and $\varphi_m(y, z)$ have same the mathematical form. Then the paraxial equation in Eq. 4.7 reduces to one transverse coordinate as follows.

$$\frac{\partial^2 \varphi_n(x, y, z)}{\partial x^2} - 2ki \frac{\partial \varphi(x, y, z)}{\partial z} = 0 \quad 4.14$$

And the solutions can be obtained solving Eq. 4.14 for one coordinate and using the same solution set for the other transverse coordinate.

Then after a tedious mathematical procedure, one can show that the solution to Eq. 4.14 can be written as a Hermite-Gaussian function as follows [69].

$$\begin{aligned} \varphi_n(x, z) = & \left(\frac{2}{\pi}\right)^{(1/4)} \sqrt{\frac{\exp[-i(2n+1)(\phi(z) - \phi_0)]}{2^n n! w(z)}} \\ & \times H_n\left(\frac{\sqrt{2}x}{w(z)}\right) \exp\left[-i\frac{kx^2}{2R(z)} - \frac{x^2}{w^2(z)} - ikz\right] \end{aligned} \quad 4.15$$

where, $H_n\left(\frac{\sqrt{2}x}{w(z)}\right)$ is the Hermite polynomial. Generally, free space modes are called as transverse electromagnetic waves (TEM) and the mode patterns (intensity distribution) for the free space Hermite-Gaussian TEM_{nm} modes are depicted in Fig. 4.3.

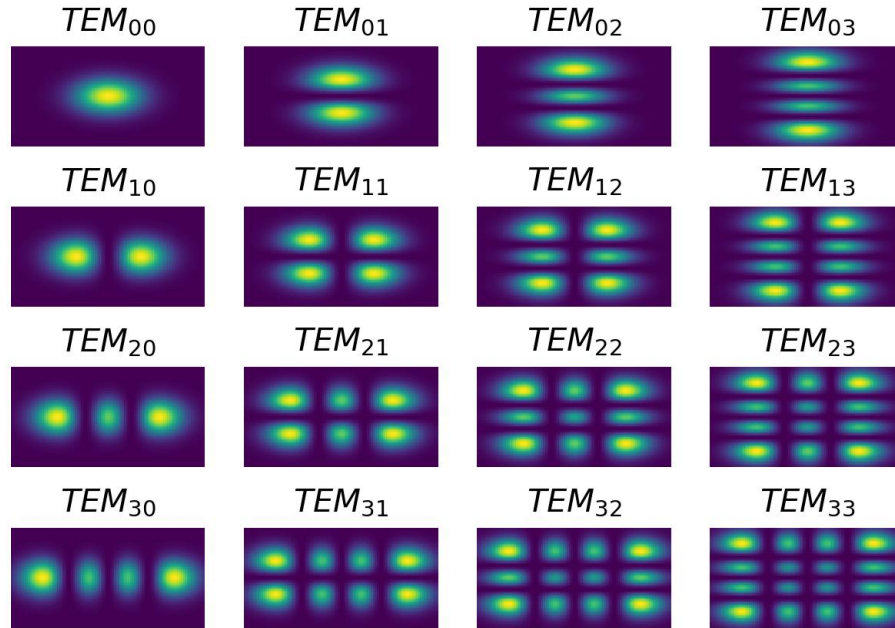


Figure 4.3 Transverse mode patterns for free space propagating Hermite-Gaussian modes. Numerically generated using a Python code.

Also, using the cylindrical coordinate system one can write the Eq. 4.7 as follows [34]. This format is suitable for describing the free space propagation of a beam coming out from a laser that possesses a cavity with cylindrical symmetry. Most of the traditional gas lasers and fiber lasers have cylindrically shaped cavity; therefore it is worthwhile to mention the free space propagation in terms of cylindrical symmetry.

$$\frac{1}{r} \frac{\partial}{\partial r} \left(r \frac{\partial \varphi}{\partial r} \right) - 2ki \frac{\partial \varphi}{\partial z} = 0 \quad 4.16$$

The solutions to the above equation are in the form of Laguerre-Gaussian functions and can be written as follows.

$$\varphi_{p,m}(r, \theta, z) = \sqrt{\frac{2p!}{(1 + \delta_{0m})\pi(m+p)!}} \frac{\exp[i(2p+m+1)(\phi(z) - \phi_0)]}{w(z)} \times \left(\frac{\sqrt{2}r}{w(z)}\right)^m L_p^m\left(\frac{2r^2}{w(z)^2}\right) \exp\left[-ik\frac{r^2}{2q(z)} + im\theta\right] \quad 4.17$$

In Eq. 4.17 L_p^m functions are the generalized Laguerre polynomials, integer m is the azimuthal mode index and integer $p \geq 0$ is the radial index. The quantities $q(z)$, $w(z)$ and $\phi(z)$ have similar definitions as in Hermite-Gaussian modes. These modes also are categorized as TEM_{pm} and intensity distribution of a few modes are depicted in Fig. 4.4.

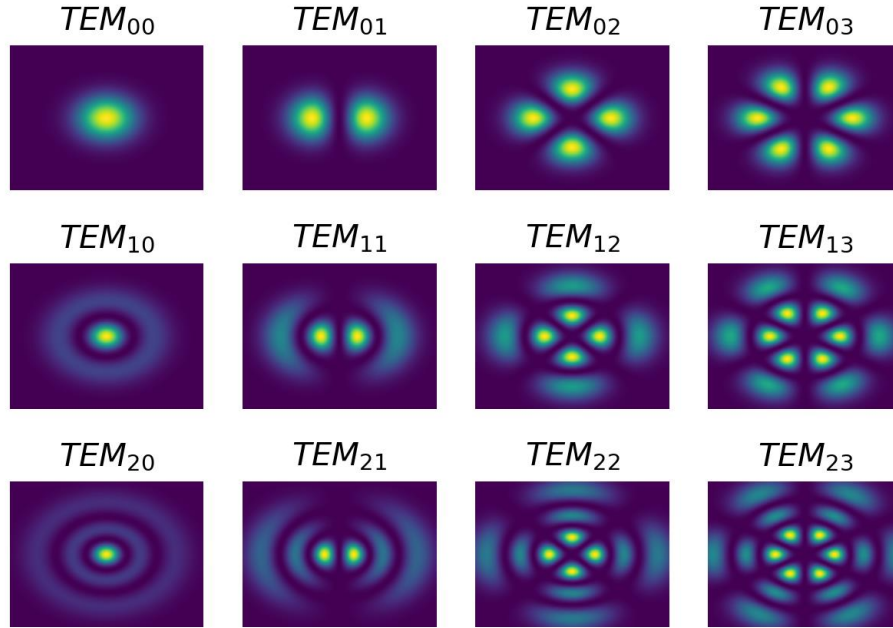


Figure 4.4 Transverse mode patterns of Laguerre-Gaussian modes. Numerically generated using a Python code.

4.2 Guided modes in step-index and hollow fibers

In this section guided modes in conventional step-index fibers and HCPCFs will be discussed. As in the free space propagation, guided modes in a fiber can be found by solving Maxwell's equations in x - y plane for a wave propagating along the fiber length (z -direction). Based on the fiber type different boundary conditions will be applied while solving Maxwell's equations and this section summarized the possible propagation modes for step-index fibers and HCPCFs.

4.2.1 Guided modes in a step-index fiber

For a medium with refractive index of n , the wave equation can be written as follows.

$$\nabla^2 \vec{E} + n^2 k^2 \vec{E} = 0 \quad 4.18$$

The index profile for a step-index fiber is shown in Fig. 4.5. The core has a refractive index of n_1 and core radius of a . The cladding has an index of n_2 and the infinite cladding radius is assumed, in practice cladding radius is very large compared to the core radius. Then we should solve the Eq. 4.18 for those two different regions and allowed modes can be obtained by imposing the appropriate boundary conditions. The detailed solutions can be found in many excellent references like Ref. [42] and Ref. [70], and here only the solutions are summarized. Since the fibers inherently poses cylindrical symmetry, cylindrical coordinates system is ideal to solve the Eq. 4.18. The electric field \vec{E} can be described as,

$$\vec{E} = \vec{E}(\rho, \phi) \exp(-i\beta z) \quad 4.19$$

where $\rho = \sqrt{x^2 + y^2}$ and ϕ are the cylindrical coordinates, and $\beta(\omega)$ is the propagation constant in the z direction.

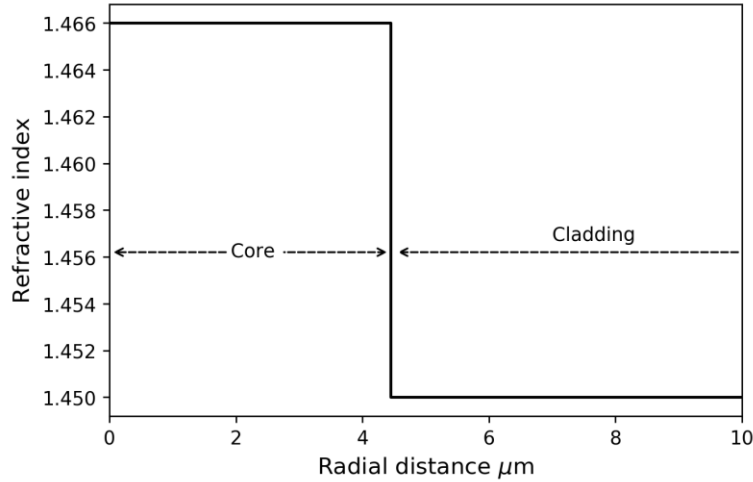


Figure 4.5 The geometry of a step-index fiber. Here the geometry of commercial SMF28 fiber is considered, which has core radius $a = 4.5 \mu\text{m}$ with a refractive index $n_1 = 1.466$ at wavelength 1550 nm. Cladding radius of $62.5 \mu\text{m}$ with a refractive index of 1.45 at the same wavelength.

The guidance inside the core governs by total internal reflection (TIR) and that the value of $\beta(\omega)$ to $n_1 k < \beta < n_2 k$ [71]. Taking β_t as the component of the propagation constant in the x - y plane, the total propagation constant can be written as,

$$\beta_t^2 + \beta^2 = n_1^2 k^2 \quad 4.20$$

To solve the wave equation Eq. 4.18, an electric field of the form in Eq. 4.19 is plugged into the wave equation Eq. 4.18 and a new differential equation for the z component of the electric field in the transverse x - y plane is obtained as follows.

$$\frac{\partial^2 E_z}{\partial \rho^2} + \frac{1}{\rho} \frac{\partial E_z}{\partial \rho} + \frac{1}{\rho^2} \frac{\partial^2 E_z}{\partial \phi^2} + \beta_t^2 E_z = 0 \quad 4.21$$

Then using the separation of variables method, we can write the electric field E_z as,

$$E_z = \sum_i R_i(\rho) \Phi_i(\phi) \exp(-i\beta_i z) \quad 4.22$$

Substituting this solution into Eq. 4.21 yields us two separate differential equations for $R(\rho)$ and $\Phi(\phi)$ as follows.

$$\frac{d^2\Phi}{d\phi^2} + m^2\Phi = 0 \quad 4.23$$

$$\frac{d^2R}{d\rho^2} + \frac{1}{\rho} \frac{dR}{d\rho} + \left(\beta_t^2 - \frac{m^2}{\rho^2} \right) R = 0 \quad 4.24$$

The solution to Eq. 4.23 is sinusoidal and solutions to Eq. 4.24 can be written in terms of Bessel's functions. Then the solutions to Eq. 4.21 can be written as follows.

$$E_z \propto J_m(u\rho/a) \sin(m\phi) \exp(-i\beta z) \quad \text{for } \rho \leq 0 \quad 4.25$$

$$E_z \propto K_m(w\rho/a) \sin(m\phi) \exp(-i\beta z) \quad \text{for } \rho \geq 0$$

where, $u = a\sqrt{n_1^2 k^2 - \beta^2}$ and $w = a\sqrt{\beta^2 - n_2^2 k^2}$.

The boundary condition for ϕ limits the constant m to be an integer. Therefore, the order of the Bessel function is also an integer. The allowable propagation constants β can be determined by solving the set of eigenvalue equations which are obtained by considering the continuity of E_z at the boundary $\rho = a$. The guidance is said to be weakly guiding if the core refractive index is slightly higher than the cladding refractive index and most of the step-index fibers are weakly guided. Therefore, the mode series associated with step-index fibers are known as LP (linearly

polarized) modes, and these LP modes can be constructed by combining appropriate EH, HE, TE, and TM modes [42]. The spatial intensity patterns in the transverse plane for a few LP modes are depicted in Fig.4.5. These modes are characterized as LP_{mn} , where m is the azimuthal mode number and n is the radial mode number. The LP_{01} mode, which is the lowest order LP mode has a similar intensity distribution like free-space TEM_{00} mode. Moreover, under the weakly guiding condition, the LP_{01} can be approximated by a Gaussian function, $\exp\left(-\rho^2/a_0^2\right)$, where the mode field diameter a_0 defines the width of the Gaussian mode. The number of guided modes for step-index fiber at a given wavelength depends on the value of the normalized frequency V , where V is given by the following equation [70].

$$V = \sqrt{u^2 + w^2} = n_1 a k \sqrt{2(n_1 - n_2)} \quad 4.26$$

The fiber is said to be a single mode fiber (SMF) if it guides only the LP_{01} mode. If the fiber core diameter and refractive indices are optimized in a way that the value of $V < 2.405$ at a given wavelength then the fiber supports only the LP_{01} mode.

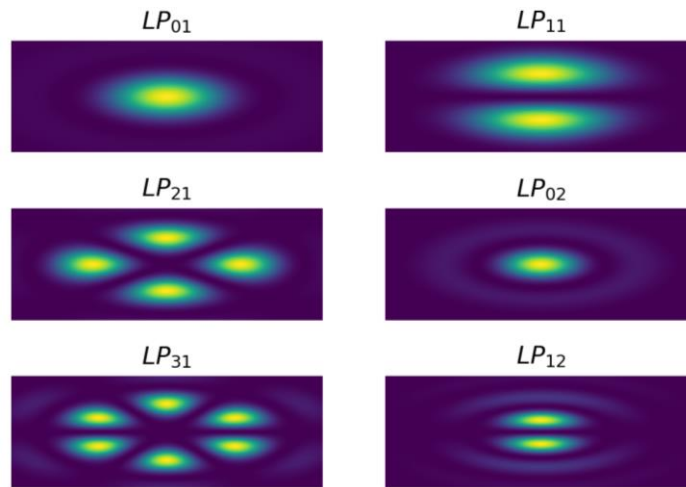


Figure 4.6 Intensity distribution of a few LP modes in step-index fiber. Numerically obtained using a Python code.

4.2.2 Guided modes in kagome structured HCPCF

Since the kagome structured HCPFs show inhibited coupling between core and cladding modes we can approximate their guidance mechanism to that of a cylindrical waveguide with a hollow core. By carefully choosing the waveguide material type and dielectric coating one can confine the light in the hollow core of the waveguide with lower losses [72]. Particularly, dielectric-coated metallic hollow waveguides have demonstrated transmission of laser light with lower losses [73-75].

For cylindrical waveguide with hollow-core, we should solve Eq. 4.1 and Eq. 4.2 to find out the allowable propagation modes. Since the cylindrical symmetry can apply to the waveguide, we can extend the discussion in the previous section to solve the wave equations. Fortunately, solutions and propagation modes can be found in many references like Refs. [42, 76]. The propagation modes are characterized as the transverse electric (TE), transverse magnetic (TM) or hybrid modes (EH or HE). Where the fundamental modes are the HE_{mn} modes, and these modes correspond to skew rays where rays do not cross the waveguide axis while propagating. The lowest order mode is HE_{11} mode, and this has an intensity distribution similar to that of free-space lowest order Gaussian mode [77]. Then, if the free-space Gaussian beam is focused down to the waveguide, HE_{11} mode of the waveguide will be excited and supports the beam propagation along the waveguide. By properly matching the free-space lowest-order Gaussian beam width with the waveguide's core diameter one can achieve couple efficiency of 99% [78]. Therefore, for acetylene filled HOFGLAS system it is important only to couple the lowest order mode of the pump beam into the HCPCF in order to obtain a laser output with a good mode quality.

Recently the modal content of the hypocycloidal kagome-structured HCPCFs was studied by employing spectral and special (S^2) imaging technique by Bradley *et al.* [79]. There, 7 and 19 cell kagome HCPCFs were studied and showed they support 4 and 7 LP modes respectively. Usually, LP modes can be interpreted as the superposition of TE, TM, HE, and EH modes [42]. Therefore, we can extend the symmetries associated with cylindrical waveguides to hypocycloidal kagome structured HCPCFs for optimizing the near-IR pump coupling. If the waveguide's entrance has a radius b , one can couple 99% of energy from free-space lowest order Gaussian mode into the waveguide if the free-space beam has a flat wavefront and beam width of $w = 0.64b$ at the waveguide entrance [78]. Then the HE_{11} or the LP_{01} mode will support the guidance inside the waveguide. If a lens with focal length of f is used to focus a free-space TEM_{00} beam with beam width w on the entrance of waveguide (or the HCPCF), the mode matching condition can be written as [65],

$$\frac{4\lambda}{\pi} \left(\frac{f}{w} \right) = 0.64 b \quad 4.27$$

where, λ is the wavelength of light.

4.3 M^2 measurement

Even though laser beam is guided with the lowest propagation mode inside the laser resonator, a laser can still deliver multimode beam into the free space due to the shape of the laser head, the thermal effect due to higher output powers, due to optical components with poor quality and spherical aberration of lenses [80]. TEM_{nm} modes guide the laser beam's free space propagation. If the beam is guiding with the TEM_{00} mode, the beam width changes according to Eq. 4.10 and if higher order modes are involved in propagation Eq. 4.10 modified as follows.

$$w(z) = w_0(z) \sqrt{1 + M^2 \left(\frac{z\lambda}{\pi w_0^2} \right)^2} \quad 4.28$$

Equation 4.28 tells that, for TEM₀₀ mode M²=1 and for any other higher order modes M² > 1. Also, Eq. 4.28 provides us a path to estimate the value of M² for a particular laser beam. One can measure the beam size along the propagation axis and use Eq. 4.28 to estimate the M² value. In fact, we implemented the same method to estimate the M² value for the output mid-IR beam of the acetylene filled HOFGLAS system. To get an accurate estimation, we followed the ISO Standard 11146 [81]. This suggests taking measurements of at least 10 different z positions. Half of the measurements should be done within one Rayleigh range on either side of the beam waist, and the other half should be taken at least two Rayleigh range away from the beam waist. And more importantly, the beam widths should be taken based on the second moment integration. Where for laser beam the second moment σ^2 is defined as follows [67, 81].

$$\sigma_x^2 = \frac{\int_{-\infty}^{\infty} (x - x_0)^2 I(x, y) dx dy}{\int_{-\infty}^{\infty} I(x, y) dx dy} \quad 4.29$$

Where, $I(x, y)$ is the laser beam intensity at a point (x, y) . Then, the beam width w_x can be written as,

$$w_x^2 = 4 \sigma_x^2 \quad 4.30$$

and the same equation can be written to other transverse direction y . One must obtain beam profiles to find out the above-mentioned quantities along the propagation axis. There are numerous ways to obtain the beam profiles. Use of scanning pin hole, scanning knife edge, scanning slit, and a

CCD camera are famous among the researchers. Among these techniques, we chose scanning slit technique simply because it gives the beam profile straightway and is a cost-effective method. Also, it automatically takes care a one integration in Eq. 4.29, less sensitive to the beam pointing and provides a good signal to noise ratio [68]. If the beam profiles are obtained with a finite slit width of s , the second moment can be written as follows [68].

$$\sigma_x^2 = \frac{\int_{-\infty}^{\infty} (x - x_0)^2 I(x, y) dx dy}{\int_{-\infty}^{\infty} I(x, y) dx dy} - s^2/12 \quad 4.31$$

Then, beam width should be modified as,

$$w_x^2 = 4 \sigma_x^2 - s^2/3 \quad 4.32$$

One can use Equations 4.31 and 4.32 to calculate the beam widths at respective positions once the beam profiles are obtained with a scanning slit and then can estimate the M^2 using Eq. 4.28.

4.3.1 M^2 for Corning SMF28 fiber

Commercially available Corning SMF28 step-index fiber manufactured in such a way that it only supports the lowest-order guidance mode (LP_{01}) for wavelengths longer than 1300 nm. Therefore, laser light coming out from an SMF28 fiber should behave as TEM_{00} mode and if we implement an M^2 measurement on this beam outcome should be $M^2 = 1$. Before employing the experimental procedure discussed in the previous section on mid-IR output beam of the acetylene filled HOFGLAS system, we decided to implement the experimental technique on the output beam from an SMF 28 fiber to test the validity of the experimental procedure.

Figure 4.7 shows a simple schematic of the experimental setup. The output of the fiber laser works at 1532 nm is coupled into a 50 cm long SMF28 fiber. The output beam from the fiber

end is collimated using an aspheric lens and focused down using another aspheric lens. Then a slit with a variable slit width (Thorlabs: VA100) is used to scan across the focused laser beam. The slit width is fixed to $60\ \mu\text{m}$, and intensity at each position is measured using a larger area photodetector (Newport: 2033).

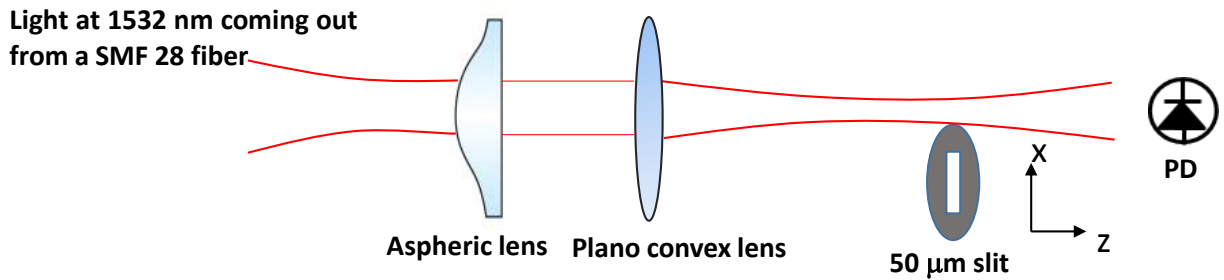


Figure 4.7 Simple schematic of the experimental setup that used to obtain the beam profiles of light coming out from a SMF28 fiber.

To obtain the beam profile at a specific axial position, the slit is mounted on a translation stage in a way that the beam is normal to the slit and translation stage is moved in the transverse plane using a micrometer. Figure 4.8 shows a beam profile obtained with the scanning slit, and it shows the shape of a Gaussian distribution as we expect.

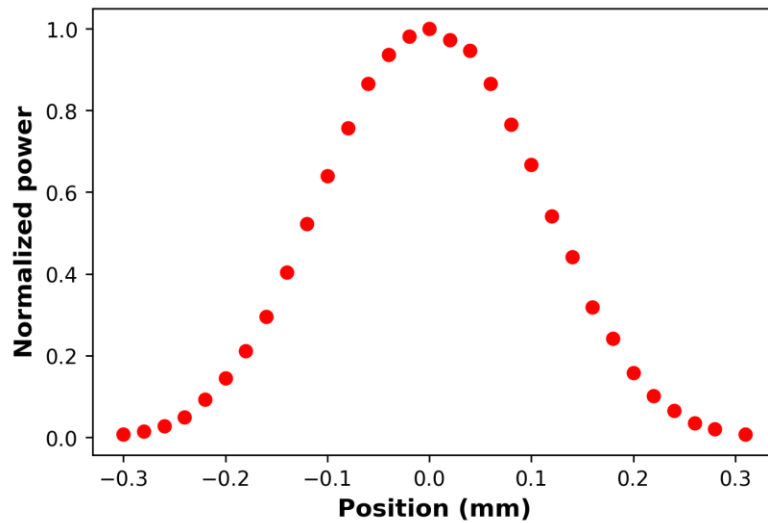


Figure 4.8 A beam profile of the beam coming out from a single-mode fiber.

Once the beam profiles are obtained at relevant axial positions, beam widths are calculated using Eq. 4.31 and 4.32. Then, the beam widths are plotted as a function of axial position z and fitted to the Eq. 4.28 to estimate the M^2 value. Figure 4.9 shows the plotted beam widths as a function of axial position. By fitting to Eq. 4.28 we found the value of M^2 equals to (1.02 ± 0.02) , which is equal to the M^2 value of a lowest order free-space mode Gaussian beam. As discussed in section 4.2.1 lowest order fiber mode LP_{01} can be approximated by lowest-order Gaussian mode under weakly guidance condition. Therefore, light coming out from the SMF 28 fiber should behave as a TEM_{00} mode and should have $M^2=1$. Since the estimated M^2 is matched with that of free-space TEM_{00} beam, we can safely implement the experimental method to estimate the M^2 value for the mid-IR beam of acetylene filled HOFGLAS system.

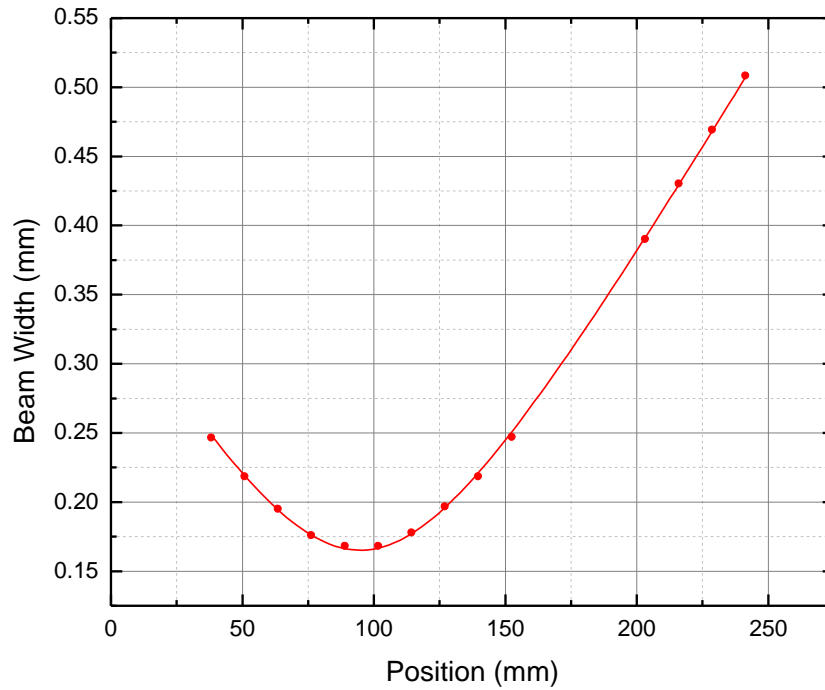


Figure 4.9 The beam width of the SMF 28 output measured using 60 μm slit.

4.3.2 M^2 measurement for mid-IR output beam of acetylene filled HOFGLS system

After Dr. Neda Dadashzadeh improved the performance of acetylene filled HOFGLAS system, we wanted to check the beam quality of the produced mid-IR beam. The first step was to optimize the focal length of the input coupling lens using Eq. 4.27 to couple only the lowest-order pump mode. Then the beam quality of the mid-IR beam is investigated at the highest laser output energy. The laser is operated with acetylene gas pressure of 10 torr and produced maximum mid-IR energy of 1.17 μJ [65].

The collimated mid-IR beam is focused using a plano-convex CaF_2 lens with a focal length of 15 cm. This specific focal length gave us adequate Rayleigh range to take data. Here, a fixed 20 μm wide slit (Thorlabs: S20RD) is used to scan the beam, and fast photo detector is used to record the intensity. Since the detector area is only 1 mm^2 , another CaF_2 lens with a focal length of 20 mm is used between the scanning slit and the photodetector to capture all the light. Then, beam profiles are obtained following the same procedure as in the previous section. Since the laser output is pulsed with a repetition rate of 30 Hz, approximately 50 pulses are averaged to take data for one point. Due to that, it took us more than 8 hours to collect the necessary data, and we made sure that the laser output is stable throughout the measurements. The obtained beam profiles for the highest laser output is depicted in Fig. 4.10. We can see that the obtained beam profiles almost show intensity distributions close to lowest-order Gaussian modes, but we need to use Eq. 4.28 in order to estimate the value of the M^2 .

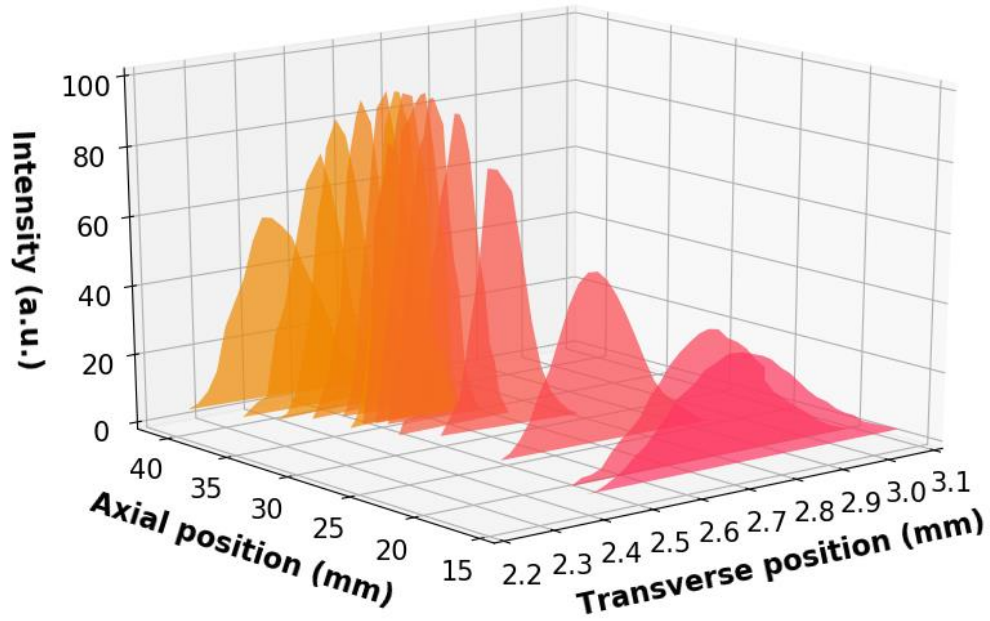


Figure 4.10 A series of beam profile obtained at the highest mid-IR laser output energy. A fixed 20 μm slit is used to scan across the beam.

Beam widths at respective positions are calculated using data in Fig. 4.10 along with Eq.4.31 and Eq. 4.32. Then the calculated beam widths are plotted as a function of axial position as fitted to the Eq. 4.28 to estimate the M^2 value for the mid-IR output beam of the acetylene HOFGLAS system. Figure 4.11 shows the obtained beam widths as a function of axial position and the fitted curve.

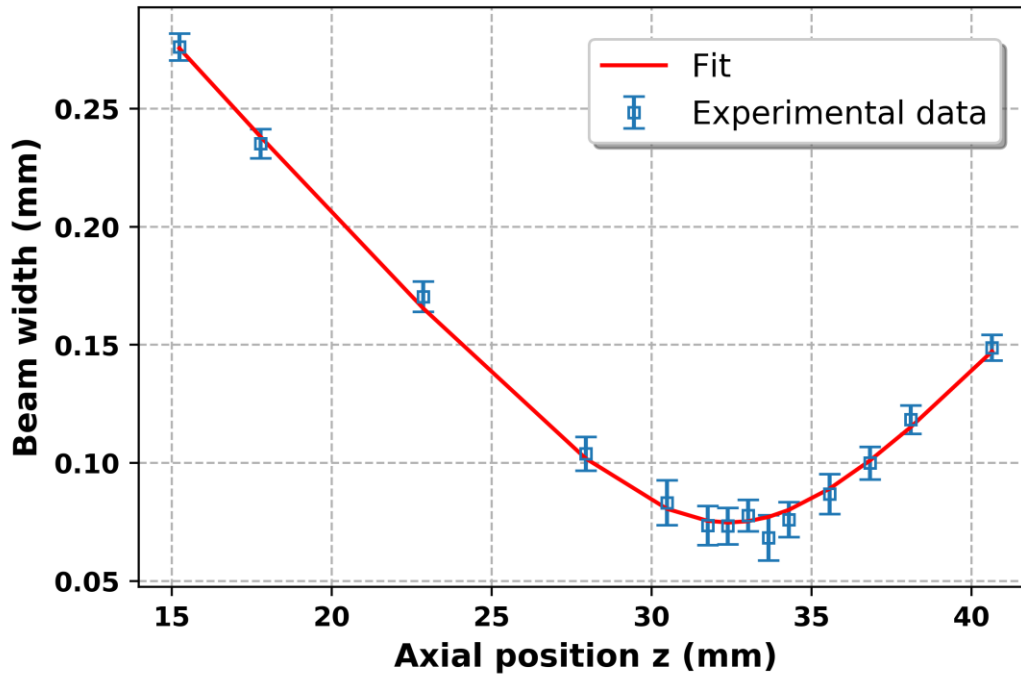


Figure 4.11 Experimentally determined beam width as a function of axial position. The laser is worked at the highest output energy. Error bars stand for fluctuations in the averages of 50 pulses.

By fitting to the Eq. 4.28 we found $M^2 = 1.15 \pm 0.02$ and the error is obtained using the fitting procedure. If the $M^2 \leq 1.3$ for a laser system then, that laser is said to be diffraction limited [82]. Since the measured M^2 value for the mid-IR beam of the acetylene filled HOFGLAS system is clearly less than 1.3, we can claim that our mid-IR laser works at the diffraction limited regime with a stable mid-IR output. Furthermore, M^2 values for other mid-IR energies are measured for the same gas pressure. The measured M^2 values are depicted in Fig. 4.12. Even though, the M^2 value slightly is changed from 1.15 for other mid-IR energies it is uncompromised. These slight deviations maybe associated with the beam quality of the near-IR pump beam. Regardless of these slight variations, we can still say that the mid-IR laser output beam is a stable diffraction limited beam, especially when it delivers the highest output energy.

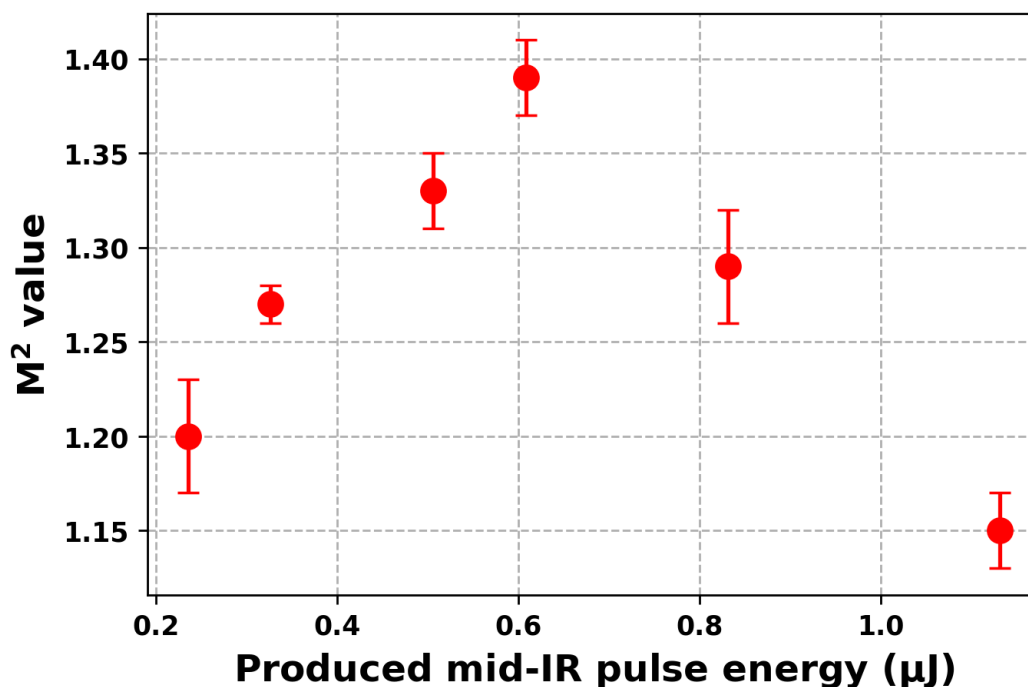


Figure 4.12 Measured M^2 values as a function of produced mid-IR pulse energy. The acetylene gas pressure inside the fiber was kept at 10 torr when measuring each data point.

To summarize this chapter, we developed a simple method to measure the beam quality of an acetylene filled HOFGLAS system. We successfully used this method in our acetylene filled HOFGLAS system and showed that the mid-IR output showed the mid-IR output beam has near diffraction limited beam quality at the highest output energy. This behavior is encouraging for power scaling the mid-IR laser system through coherent beam combining.

Another important factor when determining the power scalability of acetylene filled HOFGLAS system is how much near-IR energy absorbed by the acetylene gas at specific gas pressure. In the next chapter, I will introduce a numerical model to estimate the absorbed near-IR energy only by acetylene gas and will compare the numerical results with experimental results.

Chapter 5 - Saturated absorption in acetylene

When the laser light interacts with absorbing media, high laser intensities cause the pumping rate of an exciting transition to exceed its relaxation rate. As a consequence, the number of absorbers in the lower state will be limited. This leads to saturation in the population difference and therefore saturation in amount of optical pump power absorbed by the medium. Other than the saturation in the population difference, high pump intensities also lead in to additional line broadening. These effects will discuss in detail later. The degree of the saturation usually characterized by the saturation parameter S which defined in terms of input intensity I and saturation intensity I_s as

$$S = I/I_s \quad 5.1$$

Lamb [83] theoretically predicted this saturated absorption effect and Szöke and Javan [84] experimentally observed this phenomena for the first time as a dip in a He-Ne laser output power during its wavelength tuning. Researches have used this so called “Lamb dip” effect, i.e. a narrow frequency dip in the laser tuning curve, to stabilize the laser frequencies in past few decades [85-87].

For an absorbing medium outside the laser resonator, one need to employ pump and probe experiment to see this saturated absorption effect. In this technique a relatively high intense pump beam excites the absorbers to upper level hence saturates the population difference and counter propagating probe beam interrogates this saturated population difference or absorption. This method is widely used in saturation spectroscopy and named as Saturated Absorption Spectroscopy (SAS). SAS has been a popular technique among researches, in particular laser frequency stabilization and optical frequency references using cells filled with Rubidium (Rb) vapors or acetylene [49, 88].

Even though acetylene SAS is very interesting topic to discuss, this chapter is focused on just the saturated absorption in acetylene. Henningsen *et al.* [89] observed the reduction in optical depth with increase of input optical power for acetylene filled hollow-core fiber and for detailed discussion read section 5.2. Since the peak pump power for acetylene filled HOFGLAS system is in the order of few kilowatts and the pump light is confined in a core of an optical fiber the optical intensities are well beyond the saturation intensity for acetylene gas, it is important to discuss about the saturated absorption in acetylene and how it impacts on the acetylene filled HOFGLAS system.

5.1 Linear and nonlinear absorption

Since high optical intensities can bleach the ground state population in absorbing media, the amount of optical power absorb by the media has a nonlinear dependence with the incident radiation power. In this section the basic physics behind this phenomenon is discussed. First, I will discuss the linear absorption and extend the discussion for nonlinear absorption in homogeneously and inhomogeneously broadened media.

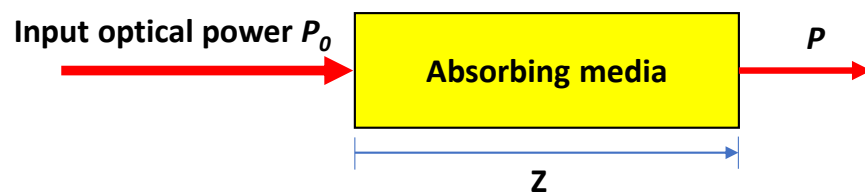


Figure 5.1 Laser with initial power P_0 travel through an absorbing medium with length Z

As in Fig. 5.1, when a weak laser beam travels through a sample of molecules and if molecules absorb the laser light by exciting from lower state to an upper state, the amount of optical power P transmit through the molecular sample can write as,

$$P = P_0 e^{-\alpha Z} \quad 5.2$$

where P_0 is the input optical power, α is linear absorption coefficient and Z is the length of the absorbing media. Equation 5.2 is known as the Lambert-Beer law of linear absorption. Here the linear absorption coefficient can be written in terms of absorption cross-section σ_{ik} and population difference ΔN_{ik}^0 between upper state k and lower state i as,

$$\alpha = \sigma_{ik} \Delta N_{ik}^0 \quad 5.3$$

When the laser intensity is high enough, absorbing media does not show a linear absorption, but the nonlinear absorption due to saturation in the population densities and absorption. Now I am going to discuss the saturation of population densities which leads to saturation in the absorption in two-level system. First discussion will be focused in saturation of homogeneous line profile and then will be extended to saturation of inhomogeneous line profile. These effects are well discussed in Ref [90] and I am going to follow the same formalism here.

5.1.1 Absorption line profile

For an absorbing medium with many absorbers (atoms) one can obtain the absorption line profile $\alpha(\omega)$ by treating absorbers as classical damped oscillator with driving force qE . Where q is the electric charge and E is the external electric field strength. With this model absorption line profile can be written as Eq. 5.4. Here, N is the number of absorbers for unit volume, e is the electron's charge, m is the mass of an electron, c is the speed of light, ω_0 is the center frequency and $\gamma = b/m$ with b is the damping coefficient.

$$\alpha(\omega) = \frac{Ne^2}{4\epsilon_0 mc} \frac{\gamma}{(\omega - \omega_0)^2 + (\gamma/2)^2} \quad 5.4$$

According to Eq. 5.4 absorption line profile $\alpha(\omega)$ is Lorentzian with Full Width Half Maximum (FWHM) of γ , which equals to the natural linewidth of the transition. Eq. 5.4 is only valid for when atoms at rest. In a gaseous medium, thermal motion of atoms introduces an additional broadening to the absorption line profile.

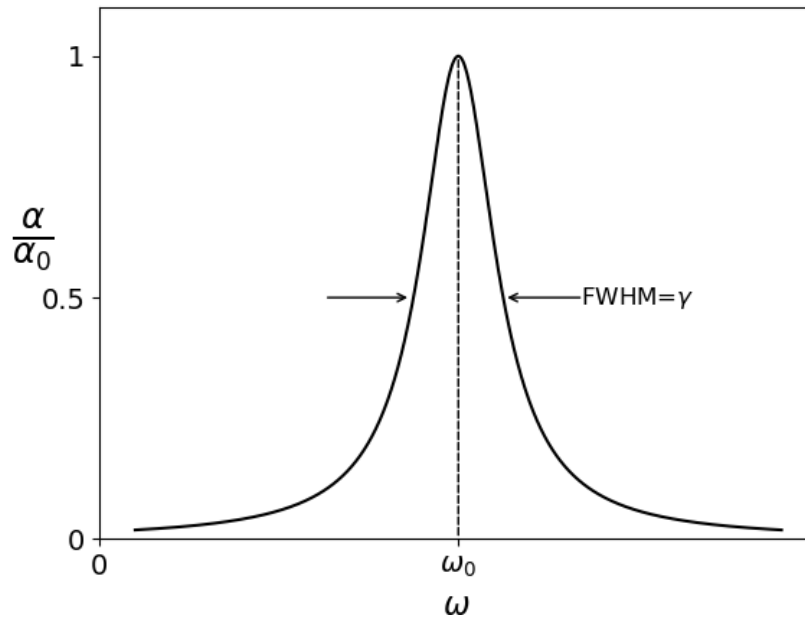


Figure 5.2 Absorption coefficient α as a function of frequency ω near to center frequency ω_0

At thermal equilibrium, the atoms or molecules of gaseous medium follow a Maxwellian velocity distribution. Due to this velocity (v_i) distribution absorbers see Doppler shifted frequency ($\omega_i = \omega_0(1 + v_i/c)$) of the incoming laser beam and light gets absorb at different frequencies. Hence the additional broadening happens in absorption profile and this additional broadening called as “Doppler broadening”. This additional Doppler broadening factor $\delta\omega_D$ can be written in

terms of universal gas constant R , temperature T , speed of light in vacuum c , molar mass M and center angular frequency ω_0 .

$$\delta\omega_D = \left(2\omega_0/c\right)\sqrt{2RT \ln 2/M} \quad 5.5$$

In frequency units, with $c = 299792458$ m/s and $R = 8.314$ J K⁻¹ mol⁻¹

$$\delta\nu_D = 7.16 \times 10^{-7} \sqrt{T/M} \text{ (Hz)} \quad 5.6$$

For acetylene molecule at room temperature (25 °C) this additional Doppler broadening is 475 MHz for P(13) absorption line.

From Eq. 5.4 we know that the frequency response of absorbers is characterized by a Lorentzian profile due to finite lifetimes of absorbers. Then, when the absorbers are at thermal equilibrium their absorption line profile will be a Voigt profile which is a convolution of Lorentzian and Gaussian profiles (see Fig. 5.3).

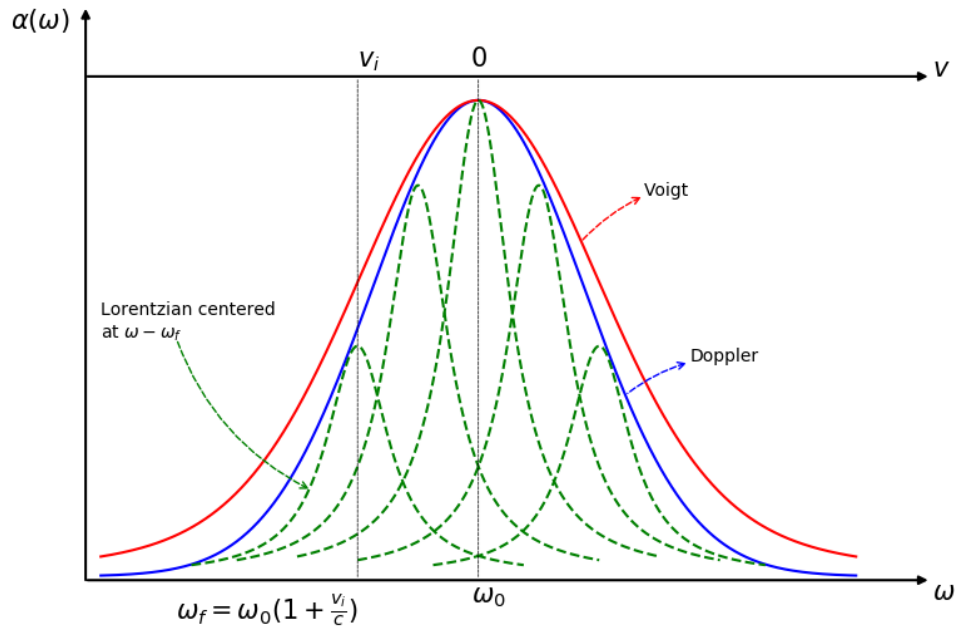


Figure 5.3 Voigt profile as a convolution of Lorentzian line shape with Gaussian profile.

At high enough pressure gas phase absorbers can collide with each other. As a result of these additional interactions between absorbers their energy levels can be shifted. This introduces additional broadening in to absorption line profile and this broadening usually called as collisional broadening or pressure broadening. Not only do these collisions introduce a broadening to the absorption line profile they also shift the center frequency of the profile (see Fig. 5.4). For acetylene P(13) line this pressure broadening factor and pressure shifts are 11 MHz/torr and -0.3 MHz/torr respectively [38].

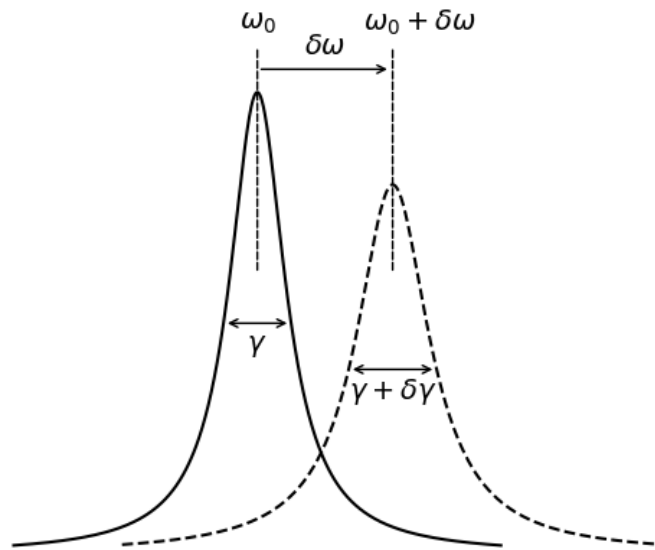


Figure 5.4 Additional broadening and shift of a Lorentzian line profile due to pressure and collisions.

5.1.2 Saturation in population difference and absorption by optical pumping

To study the saturation in population difference and absorption due to optical pumping let's focus on the rate equations for a two-level system. This two-level system is illustrated in Fig. 5.5 and population densities are N_1 and N_2 for the first level and second level respectively.

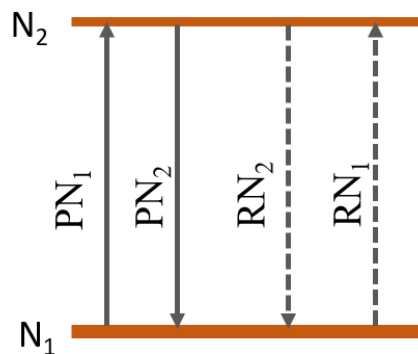


Figure 5.5 Two-level system with no relaxation mechanism to other levels

Absorption or emission and relaxation processes coupled these two levels with each other and no transitions between other levels are assumed. Absorber has a probability of $P = B_{12} \rho(\omega)$ to absorb a photon with energy $\hbar\omega$ and make transition from level 1 to level 2. Where B_{12} is the Einstein coefficient of induced absorption and $\rho(\omega)$ is the spectral energy density of radiation field. With relaxation probabilities R_1 and R_2 for we can write the rate equations for the level populations as,

$$\frac{dN_1}{dt} = -PN_1 - R_1N_1 + PN_2 + R_2N_2 \quad 5.7$$

$$\frac{dN_2}{dt} = -\frac{dN_1}{dt} \quad 5.8$$

With assumption of these levels are nondegenerate levels with unity statistical gain we can solve Eq. 5.7 and Eq. 5.8 under steady state condition ($\frac{dN_i}{dt} = 0$) with $N_1 + N_2 = N$ and show the population densities are,

$$N_1 = N \frac{P + R_2}{2P + R_1 + R_2} \quad 5.9$$

$$N_2 = N \frac{P + R_1}{2P + R_1 + R_2} \quad 5.10$$

And we can see that when the pump rate P becomes larger than the relaxation rates R_1 and R_2 population density of level 1 N_1 approaches $\frac{N}{2}$ hence $N_1 = N_2$. This means that the population difference $\Delta N = N_1 - N_2$ goes to zero and since absorption coefficient $\alpha = \sigma_{12}\Delta N$ also goes to zero. Then the medium will behave as a transparent medium for a high intense field.

If the pumping rate is negligible ($P \sim 0$), we can write the population densities for the energy levels which are at the thermal equilibrium as follows.

$$N_{10} = N \frac{R_2}{R_1 + R_2} \quad 5.11$$

$$N_{20} = N \frac{R_1}{R_1 + R_2} \quad 5.12$$

With $\Delta N_0 = N_{10} - N_{20}$ and $\Delta N = N_1 - N_2$, we can find the population difference ΔN in terms of ΔN_0 as follows.

$$\Delta N_0 = N \frac{R_2 - R_1}{R_1 + R_2}; \quad \Delta N = N \frac{R_2 - R_1}{2P + R_1 + R_2}$$

$$\Delta N = \frac{\Delta N_0}{1 + 2P/(R_1 + R_2)} = \frac{\Delta N_0}{1 + S} \quad 5.13$$

Where S is the saturation parameter with,

$$S = \frac{2P}{R_1 + R_2} = \frac{B_{12}\rho(w)}{\bar{R}} \quad 5.14$$

In other words, the saturation parameter S is the ratio of pumping rate P to the average relaxation rate $\bar{R} = \frac{R_1 + R_2}{2}$. Figure 5.6 shows the population of level 1 and the absorption coefficient as a function of saturation parameter S . When the saturation parameter approaches one, we can see that the absorption coefficient approaches half of the unsaturated absorption coefficient. If the only relaxation mechanism of the upper level 2 is the spontaneous emission to the lower level 1, we can treat $R_1 = 0$ and $R_2 = A_{21}$, where A_{21} is the Einstein coefficient of spontaneous

emission. Also, we can write the pump rate P due to a monochromatic wave as a function of intensity $I(\omega)$, absorption cross section $\sigma_{12}(\omega)$ and can obtain Eq. 5.16 as the saturation parameter S .

$$P = \frac{\sigma_{12}I(\omega)}{\hbar\omega} \quad 5.15$$

$$S = \frac{2\sigma_{12}I(\omega)}{\hbar\omega A_{12}} \quad 5.16$$

Now taking the quantity $\frac{2\sigma_{12}}{\hbar\omega A_{12}}$ as the saturation intensity I_s we can write the saturation parameter S as,

$$S = \frac{I(\omega)}{I_s(\omega)} \quad 5.17$$

When the input intensity ' I ' is equal to the saturated intensity ' I_s ', population density of level 1 becomes three quarters of total population that means that one quarter of total population is excited to the upper state level 2. Then the saturation power can be defined as "the power that needs to pump one quarter of lower level population to upper level". Finally, we can write the saturated absorption coefficient as follows.

$$\alpha(\omega) = \sigma_{12}\Delta N$$

Using Eq. 5.13 with unsaturated absorption coefficient $\alpha_0 = \sigma_{12}\Delta N_0$,

$$\alpha(\omega) = \frac{\alpha_0}{1+S} \quad 5.18$$

Eq. 5.18 describes the saturated absorption for homogeneously broadened line. Saturated absorption for inhomogeneously broadened line will be discussed in section 5.2.

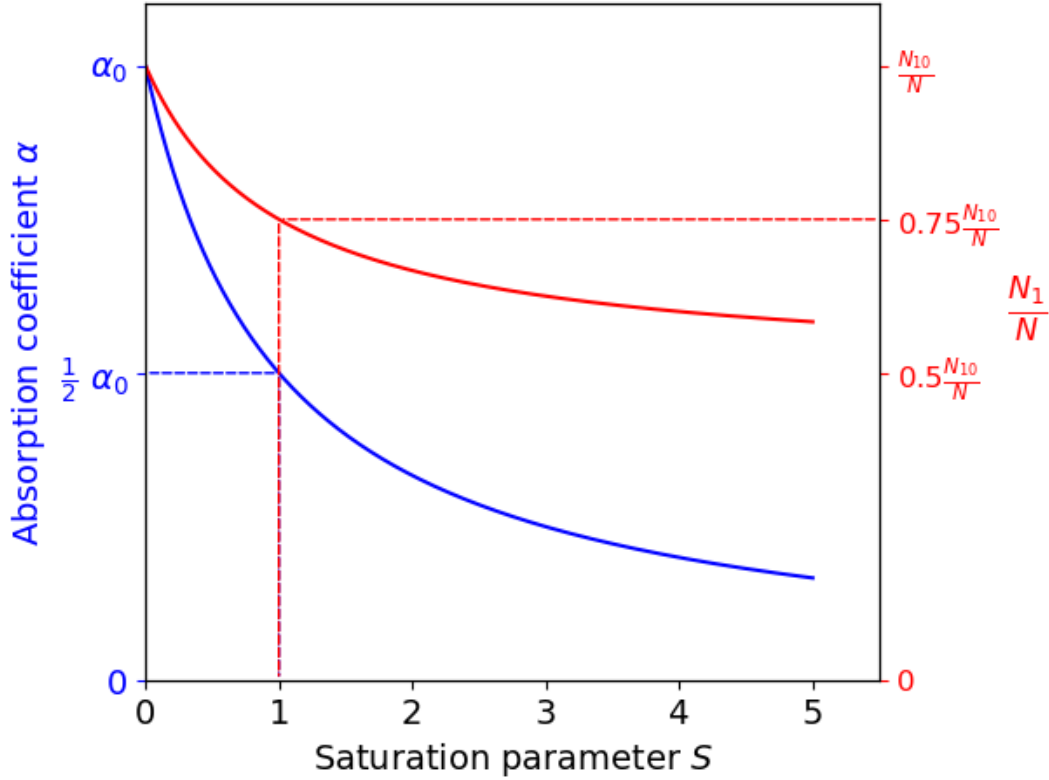


Figure 5.6 Saturation of absorption coefficient α and population density of level one as a function of saturation parameter S .

5.1.3 Saturation and power broadening of homogeneous line profile

Optical pumping reduces the peak absorption and causes the line profile to become broader. From Eq. 5.4 we know that absorption line profile $\alpha(\omega)$ homogeneously broadened line exhibits a Lorentzian profile. With the frequency independent mean relaxation $\langle R \rangle$ we can introduce the frequency dependent spectral saturation parameter as S_ω as,

$$S_\omega = \frac{B_{12}}{\langle R \rangle} L(\omega - \omega_0) \quad 5.19$$

Then we can write spectral saturation parameter S_ω as Eq. 5.20. In Eq. 5.20, $S_0 = S_\omega(\omega_0)$.

$$S_\omega = S_0 \frac{(\gamma/2)^2}{(\omega - \omega_0)^2 + (\gamma/2)^2} \quad 5.20$$

Along with Eq. 5.20 it can be shown that the absorption line profile is saturated and broadened with the optical pumping. Saturated absorption line profile $\alpha_s(\omega)$ can be written as,

$$\alpha_s(\omega) = \alpha_0(\omega_0) \frac{(\gamma/2)^2}{(\omega - \omega_0)^2 + (\gamma_s/2)^2} = \frac{\alpha_0(\omega)}{1 + S_\omega} \quad 5.21$$

where the unsaturated absorption profile is

$$\alpha_0(\omega) = \frac{2\hbar\omega B_{12}\Delta N_0}{\pi c\gamma} \frac{(\gamma/2)^2}{(\omega - \omega_0)^2 + (\gamma/2)^2} \quad 5.22$$

Saturated absorption line profile in Eq. 5.21 also a Lorentzian profile with increased line width

$$\gamma_s = \gamma\sqrt{1 + S_0} \quad 5.23$$

Equation 5.21 tells us that the absorption coefficient is decreasing with the saturation parameter S_ω . And the absorption coefficient $\alpha(\omega)$ is decreased by the factor $(1+S_\omega)$. This saturation factor is maximized at the line center ω_0 and decreases as $(\omega - \omega_0)^2$ increasing. As a consequence the saturation is strongest at the line center and it approaches zero in the wings. Also as in Eq. 5.23 this saturation introduces additional line broadening. As a result of these saturation effects absorption line profile will get broader in width and its peak will go down to preserve the

area under the curve. These saturation effects are shown in Fig. 5.7. Also it can be shown that the broadening in absorption line profile due to intense laser field has the similar behavior as in Eq. 5.23 for more details refer to Section 3.6.3 of Ref [90].

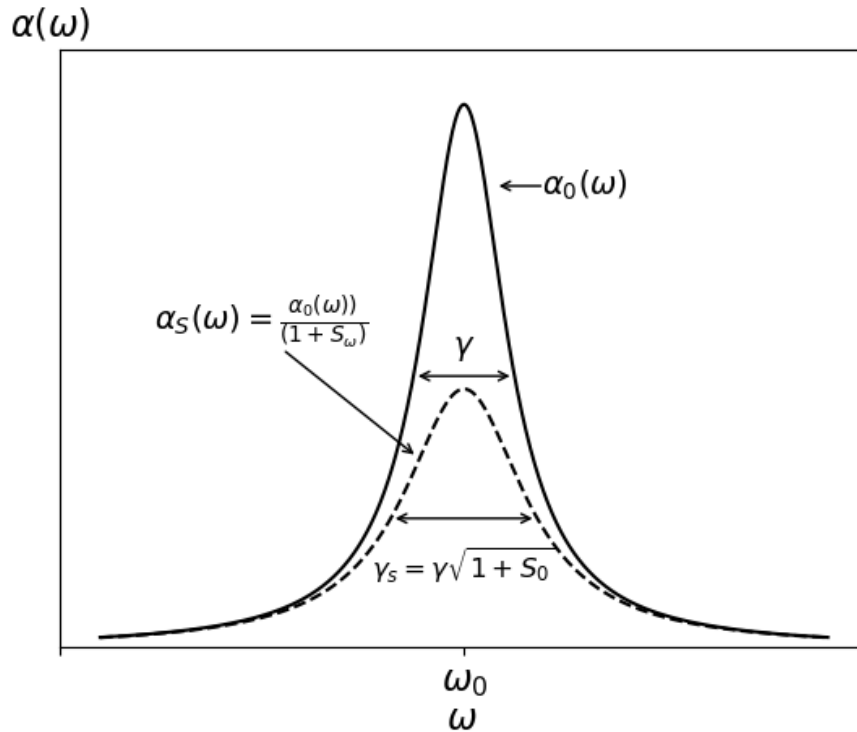


Figure 5.7 Broadening of homogeneous line profile due to saturation or power.

5.1.4 Saturation of the inhomogeneous line profile

In this section I will discuss the saturation of inhomogeneous line profile. Since the gaseous phase absorbers follow a Maxwell-Boltzmann velocity distribution at thermal equilibrium, they see Doppler shifted laser frequency. Due to these different Doppler shifted frequencies absorption line profile is inhomogeneously broadened.

Let's consider a monochromatic light wave E travelling in z -direction goes through a gas phase absorbing medium with a Maxwell-Boltzmann velocity distribution.

$$E = E_0 \cos(\omega t - kz), \text{ with } k=k_z \quad 5.24$$

with $\vec{k} \cdot \vec{v} = kv_z$ the molecules moving with velocities \vec{v} have the Doppler-shifted laser frequencies of $\omega' = \omega - kv_z$ in their reference frame. If these shifted frequencies lie within the homogeneous linewidth γ around the center absorption frequency ω_0 of a molecule at rest, those molecules can contribute to the absorption significantly.

For the two-level system depicted in Fig. 5.5 we can write the saturated population densities for levels as Eq. 5.25 and Eq. 5.26, where $N_i^0(v_z)$ is the density of all molecules in level E_i with velocity v_z . It is clear that due to the absorption, population density in level 1 with velocity class v_z should decrease and population density in the upper level increases accordingly. In Eq. 5.23 and Eq. 5.24, γ_1 and γ_2 are related to the life times of level 1 and 2.

$$N_1(\omega, v_z) = N_1^0(v_z) - \frac{\Delta N^0}{\gamma_1 \tau} \left[\frac{S_0(\gamma/2)^2}{(\omega - \omega_0 - kv_z)^2 + (\gamma_s/2)^2} \right] \quad 5.25$$

$$N_2(\omega, v_z) = N_2^0(v_z) + \frac{\Delta N^0}{\gamma_2 \tau} \left[\frac{S_0(\gamma/2)^2}{(\omega - \omega_0 - kv_z)^2 + (\gamma_s/2)^2} \right] \quad 5.26$$

The quantity $\gamma = \gamma_1 + \gamma_2$ is the homogeneous width of the absorption and the quantity $\tau = \frac{1}{\gamma_1} +$

$\frac{1}{\gamma_2} = \frac{\gamma}{\gamma_1 \gamma_2}$ is called the longitudinal relaxation time. And the transverse relaxation time can be

written as $T = \frac{1}{\gamma_1 + \gamma_2} = \frac{1}{\gamma}$.

Figure 5.8 shows the population densities of upper and lower levels as a function of velocity v_z when pump with optical frequency ω . The optical pump burns a hole in lower state population density at $v_z = \frac{\omega - \omega_0}{k}$ and creates a peak in the upper state population density. This hole and peak

are called as Benne hole and Bennet peak. When $\gamma_1 \neq \gamma_2$ the depth of Bennet hole in lower state $N_1(v_z)$ and height of Bennet peak in upper state $N_2(v_z)$ are different and we get the saturated population difference $\Delta N(\omega_s, v_z)$ as Eq. 5.27 by taking the difference between Eq. 5.25 and Eq. 5.26.

$$\Delta N(\omega_s, v_z) = \Delta N_0(v_z) \left[1 - \frac{S_0(\gamma/2)^2}{(\omega - \omega_0 - kv_z)^2 + (\gamma_s/2)^2} \right] \quad 5.27$$

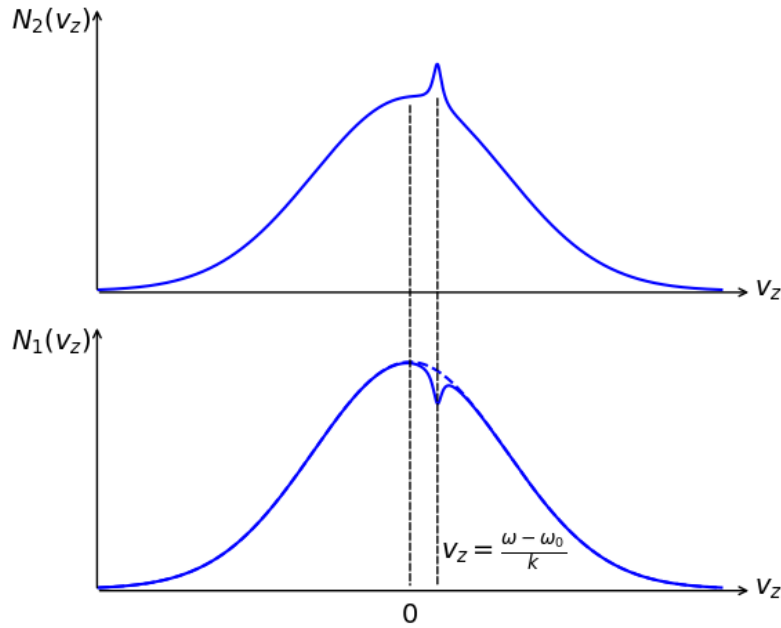


Figure 5.8 The Bennet hole and Bennet peak in the lower and upper state population densities.

As in Eq. 5.27 velocity distribution $\Delta N(\omega_s, v_z)$ also shows a velocity-selective minimum *i.e.* a Bennet hole at $v_z = \frac{\omega - \omega_0}{k}$. And this Bennet hole has the homogeneous width of $\gamma_s = \gamma\sqrt{1 + S_0}$ due to characteristic line profile. The depth of the Bennet hole at the hole center $v_z = (\omega - \omega_0)/k$ is,

$$\Delta N_0(v_z) - \Delta N(v_z) = \Delta N_0(v_z) \frac{S_0}{1 + S_0} \quad 5.28$$

When $S_0 = 1$ the depth of the hole is equal to the half of unsaturated population difference. It is clear that with increases of pumping intensity/ power, the depth and width of the hole increase. The contribution given by molecules with velocity components in the interval v_z to $v_z + dv_z$ to the absorption coefficient $\alpha(\omega, v_z)$ can be written as,

$$\frac{d\alpha(\omega, v_z)}{dv_z} dv_z = \Delta N(v_z) \sigma_{12}(\omega, v_z) dv_z \quad 5.29$$

where the absorption cross-section $\sigma(\omega, v_z)$ is given by,

$$\sigma_{12}(\omega, v_z) = \sigma_0 \frac{(\gamma/2)^2}{(\omega - \omega_0 - kv_z)^2 + (\gamma/2)^2} \quad 5.30$$

Then the total absorption coefficient $\alpha(\omega)$ can calculate by integrating over all velocities as follow.

$$\alpha(\omega) = \int \Delta N(v_z) \sigma_{12}(\omega, v_z) dv_z \quad 5.31$$

Using $\Delta N_0(v_z) = \frac{\Delta N_0}{v_p \sqrt{\pi}} e^{-(v_z/v_p)^2}$ and Eq. 5.30 in Eq 5.31 yields,

$$\alpha(\omega) = \frac{\Delta N_0 \sigma_0}{v_p \sqrt{\pi}} \int \frac{e^{-(v_z/v_p)^2} (\gamma/2)^2 dv_z}{(\omega - \omega_0 - kv_z)^2 + (\gamma_s/2)^2} \quad 5.32$$

Here $v_p = \sqrt{\frac{2k_B T}{m}}$ is the most probable velocity and $\Delta N_0 = \int \Delta N_0(v_z) dv_z$ is the unsaturated population difference. Equation 5.30 gives a Voigt profile with saturation broadened homogeneous

line width γ_s . If $S_0 < 1$ generally the Doppler width dominates the numerator in Eq. 5.32 and factor $e^{-(v_z/v_p)^2}$ can be taken out from the integral. Then integral is solved analytically as follow.

$$\text{Let } \int_{-\infty}^{+\infty} \frac{dv_z}{(\omega - \omega_0 - kv_z)^2 + (\gamma_s/2)^2} = \int_{-\infty}^{+\infty} \frac{dx}{(x^2 + a^2)} \text{ with } x = (\omega - \omega_0 - kv_z) \text{ and } a = \gamma_s/2.$$

This yields us $\int_{-\infty}^{+\infty} \frac{dx}{(x^2 + a^2)} = \frac{1}{a} \left[\tan^{-1} \frac{x}{a} \right]_{-\infty}^{+\infty} \rightarrow \frac{2\pi}{\gamma_s \sqrt{1 + S_0}}$, then with $v_z = \frac{\omega - \omega_0}{k}$ and $k = \omega_0/c$.

Putting all of these together we have the saturated absorption coefficient as,

$$\alpha_s(\omega) = \frac{\alpha_0(\omega_0)}{\sqrt{1 + S_0}} \exp \left\{ - \left[\frac{\omega - \omega_0}{0.6\delta\omega_D} \right]^2 \right\} \quad 5.33$$

Where $\alpha_0(\omega_0) = \Delta N_0 \frac{\sigma_0 \gamma_c \sqrt{\pi}}{2 v_p \omega_0}$ and the Doppler width $\delta\omega_D = \frac{\omega_0}{c} \sqrt{\frac{8k_B T \ln 2}{m}}$.

Then the absorption coefficient for inhomogeneous profile can be written as,

$$\alpha_s(\omega) = \frac{\alpha(\omega)}{\sqrt{1 + S_0}} \quad 5.34$$

This absorption coefficient $\alpha_s(\omega)$ shows a Voigt profile with reduced amplitude by factor $\sqrt{1 + S_0}$. Along with Eq. 5.17 we can write Eq. 5.34 as,

$$\alpha_s(\omega) = \frac{\alpha(\omega)}{\sqrt{1 + I/I_s}} \quad 5.35$$

Since the absorption profile for acetylene molecules at room temperature is Doppler broadened we can use Eq. 5.34 or Eq. 5.35 to estimate the optical power absorbed by acetylene molecules inside a fiber at given pressure. In the next section I will discuss how we can use Eq. 5.35 to estimate the pump power/energy absorb by acetylene gas in different mid-IR acetylene filled HOFGLAS systems.

5.2 Numerical model to estimate the pump absorbed energy by gas for the HOFGLAS system

In this section I will discuss a simple numerical model to estimate the absorbed pump energy by acetylene gas in the HOFGLAS system for given pressure. And finally, I will compare the results of numerical model to experimental results for different HOFGLAS systems.

In 2017 Lane *et al.* [91] have developed a numerical model to understand the primary physical processes that affect the HOFGLAS output and efficiency. There, two numerical models were developed, and numerical results were comrade to experimental results of Ref. [27]. The first model was a time-dependent model and based on a single frequency, one-dimensional calculation. Even though this model successfully predicted the lasing threshold, it overpredicted the absorbed near-IR energy absorbed by the gas. The second numerical model was a two-dimensional, time-dependent model and Gaussian spectral and radial intensity profiles were assumed for the pump beam. By doing so, the authors were able to obtain better numerical results for absorbed near-IR pump energy by acetylene gas. But still, the numerical results are overestimated. Even though this work showed some agreement between experimental and numerical results, the numerical models are based on rate equations, and computationally it is not trivial to solve them. So, a flexible, quick method is needed to predict the mid-IR laser operation of the acetylene HOFGLAS system with a

given fiber length and gas pressure. Here, I will introduce a numerical model to predict the amount of absorbed near-IR pump energy/power by acetylene gas in a HOFGLAS system.

Since both the fiber and gas absorb near-IR pump energy, it is important to optimize the fiber length and the acetylene gas pressure to obtain a higher mid-IR energy with a good laser slope efficiency. One can do this experimentally by trying different fiber lengths and different gas pressures. But this requires many of fiber cut backs, which is an expensive and somewhat tedious process. If we can numerically estimate the amount of energy that loses to the fiber and the amount of energy that absorbs by acetylene gas it would be beneficial for the experiment to power scale the acetylene filled HOFGLAS system.

Since both the fiber and gas absorb the pump energy (power) we can write the intensity of pump light I as follows,

$$\frac{dI}{dz} = -\alpha_g I - \alpha_f I \quad 5.36$$

Where, α_g is the gas absorption coefficient and α_f is the fiber loss coefficient. In the previous section I showed that α_g can be written as Eq. 5.35 for inhomogeneously broadened absorption line.

$$\alpha_g = \frac{\alpha_0}{\sqrt{1 + I/I_s}} \quad 5.37$$

In Eq. 5.37, α_0 is the unsaturated absorption coefficient and I_s is the saturation intensity. The unsaturated coefficient α_0 is given by,

$$\alpha_0 = NSg(v - v_0) \quad 5.38$$

here N is number of absorbers per unit volume in the medium, S is the line strength of chosen absorption line and $g(\nu - \nu_0)$ is the area normalized line shape function. By assuming the ideal gas law we can write down Eq. 5.38 in terms of gas pressure p , temperature T and Boltzmann constant k_B as follows.

$$\alpha_0 = \frac{p}{k_B T} S g(\nu - \nu_0) \quad 5.39$$

Finally, we can write down the Eq. 5.36 as follows by combining Eq. 5.37 and Eq. 5.39.

$$\frac{dI}{dz} = - \frac{p}{k_B T} \frac{s g(\nu - \nu_0)}{\sqrt{1 + I/I_s}} I - \alpha_f \quad 5.40$$

Now we need to solve Eq. 5.40 for acetylene gas at a given pressure inside a hollow-core fiber with a specific length. Assuming uniform cross-sectional area for core of the fiber we can write Eq. 5.40 as a function of laser power P_l as follows, where P_s is the saturation power acetylene.

$$\frac{dP_l}{dz} = - \frac{p}{k_B T} \frac{s g(\nu - \nu_0)}{\sqrt{1 + P_l/P_s}} P_l - \alpha_f P_l \quad 5.41$$

5.2.1 Saturation power for acetylene $\nu_1 + \nu_3$ absorption band

Henningsen *et al.* [89] estimated the saturation power to be 23 mW for acetylene by measuring transmitted optical power through a 6.35 m long hollow-core photonic band gap (HC-PBG) fiber filled with 10 Pa (75 mtorr) gas pressure of acetylene. Using the experimental setup shown in Figure 1 the peak absorbance was determined for the acetylene P(9) line as a function of off-resonance power exit from the fiber. HC-PBG fiber which was used in the experiment has 10 μm

core diameter with hexagonal cladding structure and 0.2 dB/m fiber loss at acetylene P(9) line. In order to estimate the saturation power (intensity) they omitted the fiber loss term in Eq. 5.41, hence assumed the average power inside the fiber is 16% higher than the power at the exit end of the fiber and they used an analytical solution to Eq. 5.41.

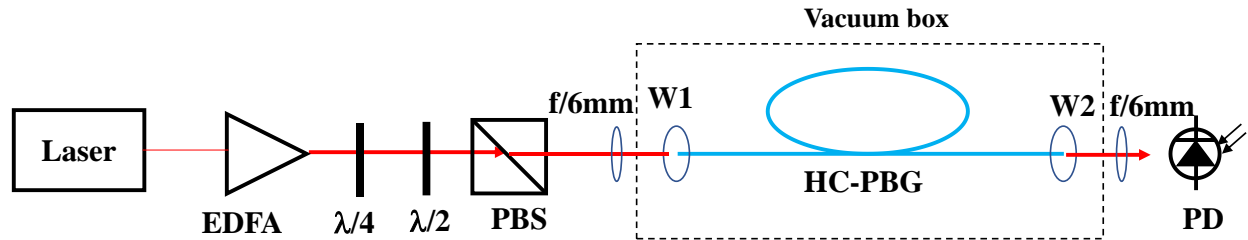


Figure 5.9 Simplified experimental configuration to determine the peak absorbance. A 6.35 m long HC-PBG fiber is coiled with 6 cm diameter and both ends are inside a vacuum chamber. W1 and W2 are 1 mm thick sapphire windows. $\lambda/4$ is a quarter wave plate and $\lambda/2$ is a half wave plate. PBS is a polarizing beam splitter. The EDFA is seeded with extended cavity diode laser and EDFA operated at 60 mW output power. PD is $5 \times 5 \text{ mm}^2$ Ge photo diode and two 6 mm convex lens are used couple in/out the light to/from fiber.

Without the fiber loss term, we can write Eq. 5.40 with definition of unsaturated absorption coefficient α_0 as,

$$\frac{dP_l}{dz} = -\frac{\alpha_0}{\sqrt{1 + P_l/P_s}} \quad 5.42$$

By solving Eq. 5.42 analytically the input power P_{l0} and output power P_{lL} is related by following equation.

$$\alpha_0 L = 2 \left(\sqrt{1 + P_{l0}/P_S} - \sqrt{1 + P_{lL}/P_S} \right) + \ln \frac{\left(\sqrt{1 + P_{lL}/P_S} + 1 \right) \left(\sqrt{1 + P_{l0}/P_S} - 1 \right)}{\left(\sqrt{1 + P_{lL}/P_S} - 1 \right) \left(\sqrt{1 + P_{l0}/P_S} + 1 \right)} \quad 5.43$$

Henningsen *et al.* [89] calculated the unsaturated Napierian peak absorbance $\alpha_0 L$ (I will call this quantity optical depth from here on) to be 0.963 for acetylene P(9) absorption line for $\nu_1 + \nu_3$ band (1530.37095 nm). They have used line strength $S = 1.024 \times 10^{-20} \text{ cm}^{-1}/(\text{molecules cm}^{-2})$ for acetylene P(9) absorption line and the line shaping function $g(\nu - \nu_0)$ would be either Voigt or Gaussian depending on the pressure regime. By solving Eq. 5.43 for a given input optical power and measured output power they estimated the saturation power for each input powers. Figure 5.10 shows the peak optical depth and the estimated saturation powers as a function of off-resonance transmitted power.

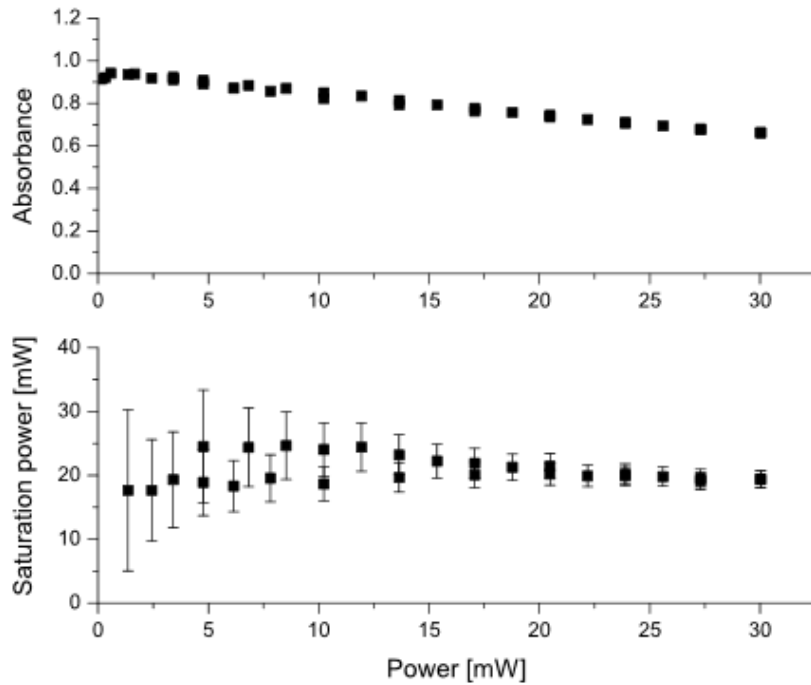


Figure 5.10 Peak Optical depth (top) for the 6.35 m fiber filled with 10 Pa acetylene and saturation power (bottom) as a function of off-resonance transmitted power. (Reproduced with permission from Ref [89], [The Optical Society].)

As I discussed earlier Henningsen *et al.* [89] estimated the saturation power as 23 mW by considering that the average power inside the fiber is 16% higher than the exit power due to fiber loss. And, they pointed out this estimated saturation power might be somewhat lower than the actual saturation power due to presence of fiber surface modes.

5.2.2 Numerical calculation to estimate the absorbed energy by gas

To estimate the absorbed pump energy only by gas I modified the Python script written by Dr. Brian Washburn and a copy of the script in the appendix. To test the validity of Python script I reproduced the upper plot of Fig. 5.10 by using data available with Ref [89]. I used the same line strength and wavelength values which are reported in Ref. [89]. Also, the Voigt profile from the Python lmfit package [92] was used as the line shape function and 12.46 MHz/torr [38] was used

as the pressure broaden factor for P(9) line. The peak of the Voigt profile depends on the full width half max (FWHM) of the profile. Since both Doppler and pressure broadening effect on the FWHM of the Voigt profile, 2.35σ is used as the Gaussian broadening factor, where $\sigma = 201$ MHz depends on temperature (296 K) and molar mass of acetylene.

In this script I numerically solved Eq. 5.41 using the ODE solver in Python to calculate the peak optical depth for specific input powers. Equation 5.41 was solved under similar conditions as in Fig 5.10 except the input power. In Fig 5.10, authors used the off-resonance transmitted power as the x-axis, which has been degraded due to fiber loss. But when we need to solve Eq. 5.42 we need to reverse the process to get the input power levels. So as the input powers I used the same x-axis values and multiply by them with factor of $e^{(\alpha_f \times 6.35)}$ to eliminate the fiber loss factor. For the Ref. [89] x-axis values are, $P_{out} = P_{in} \times e^{-\alpha_f L}$. So, the $P_{in} = P_{out} \times e^{\alpha_f L}$.

If we have unsaturated absorption, we can write power along the fiber as,

$$\frac{dP}{dz} = -\alpha_0 P - \alpha_f P \quad 5.44$$

Where, α_0 is the unsaturated absorption coefficient for acetylene gas which is given by Eq. 5.39 and α_f is the fiber loss coefficient in m^{-1} . By solving Eq. 5.44 we can write peak optical depth as,

$$\alpha_0 L = \ln\left(\frac{P(0)}{P(L)}\right) - \alpha_f L \quad 5.46$$

And following same argument we can write peak optical depth for saturated absorption as,

$$\text{Peak optical depth} = \ln\left(\frac{\text{Input power}}{\text{Transmitted power}}\right) - \alpha_f L \quad 5.48$$

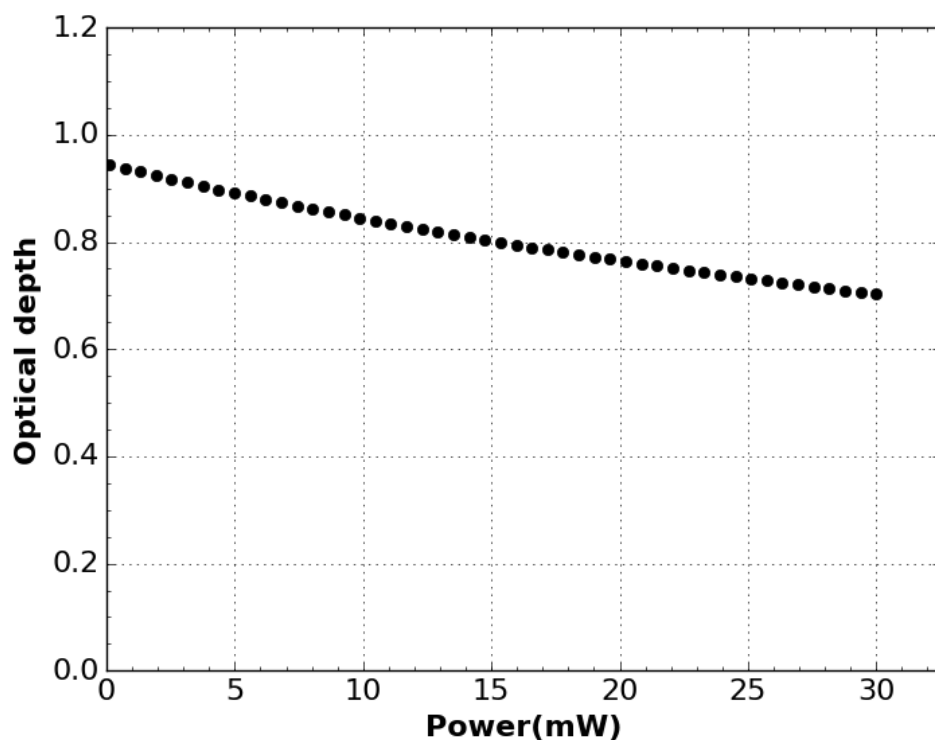


Figure 5.11 Calculated optical depth by solving Eq. 5.42 numerically for the 6.35 m long fiber filled with 10 Pa (0.075 torr) acetylene gas as a function of input power.

Then by solving Eq. 5.41 numerically I calculated the peak optical depth as in Eq. 5.48 and resulted values are shown in Fig. 5.11 as a function of input powers.

In Ref. [89], the authors determined the peak optical depth in low power limit to be in good agreement with unsaturated peak optical depth $\alpha_0 L = 0.963$. With our numerical calculation we calculated the peak optical depth at low input power regime to be 0.945. Even though there is slight difference between experimental and numerical values for the peak optical depth, its behavior with the input power is matched well. I also calculated the unsaturated peak optical depth for acetylene under same conditions by using the same Python script and it turned out to be 0.946. And this reflects that the calculated peak optical depth at the low power limit is in good agreement with the calculated unsaturated peak optical depth. It can be concluded that the above mention difference

between experimental value and the numerical value is not due to a numerical error rather a difference in the peak of line shaping function. Since results from the above numerical method are in good agreement with observations of Henningsen *et al.* [89], we can use this method in HOFGLAS system for estimate the power(energy) absorb by the acetylene gas.

5.2.2 Estimating absorb power/energy by acetylene gas in different HOFGLAS systems.

In this section I will discuss how I applied the above method to estimate the absorbed power (energy) by acetylene gas in given HOFGLAS configuration and finally I will compare the outcome with experimental observations. Three acetylene filled HOFGLAS systems were studied, a continuous wave (CW) laser configuration and a 1 ns pulsed laser configuration with two different fiber lengths.

Xu *et al.*[28] demonstrated a 1 W continuous-wave mid-IR laser output with acetylene filled hollow-core fiber. Further details about the characteristics of the laser is discussed in section 1.1. For the numerical calculation for this system I picked two data sets from the Ref. [93], which are related to acetylene gas pressure of 0.6 mbar (0.435 torr) and 4.23 mbar (3.17 torr). The fiber length used in the setup is 15 m and the acetylene molecules are pumped via the P(9) line. Even though authors of Ref. [28] reported produced mid-IR power as a function of incident pump power, roughly 50% of the incident power is confined at the pumping wavelength due to large ASE associate with the high power EDFA. Figure 5.12, which is reproduced from Ref. [28] shows the spectrum of EDFA output at 9.6 W.

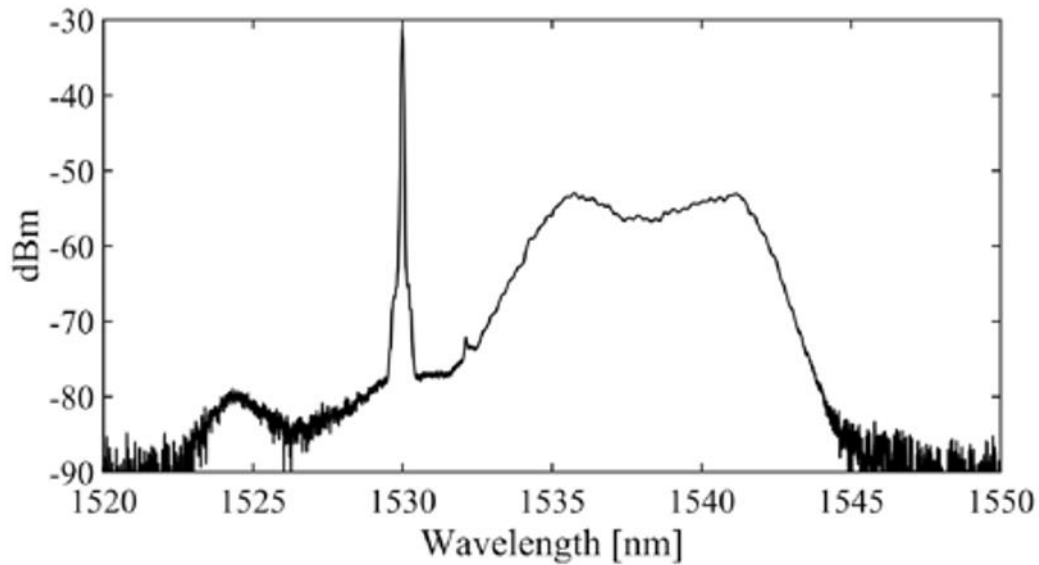


Figure 5.12 EDFA spectrum measured when output power is at 9.6 W. Approximately 50% of the total output power lies within a 3 nm bandwidth around the seed wavelength. (Reproduced with permission from Ref [28],[The Optical Society]).

The anti-resonant fiber used in the above work has loss of 37 dB/km [28] at pump wavelength (1530.385 nm). The updated line strength for P(9) line is $1.211 \times 10^{-20} \text{ cm}^{-1}/(\text{molecules cm}^{-2})$ [38], pressure broaden factor is 12.49 MHz/torr ($0.158 \text{ cm}^{-1}/\text{atm}$) [38]. Since 50% of the incident power is at the pumping wavelength, input power is scaled by 50% in the Python script. With these information, a Voigt profile was used as the normalized line shaping function and absorbed power by acetylene gas is estimated by solving the Eq. 5.41 numerically. Absorbed power by acetylene gas is estimated as a function of input power for two different gas pressures. Depending on the laser performance and availability of data 0.6 mbar and 4.23 mbar are used as the acetylene gas pressure. Figure 5.13 shows the comparison between numerical results and experimental results which are in good agreement especially at lower pressure. Even though there is slight difference between numerical results and experimental values for higher pressure system, that could be due to an over estimation of absorbed energy in the experiment.

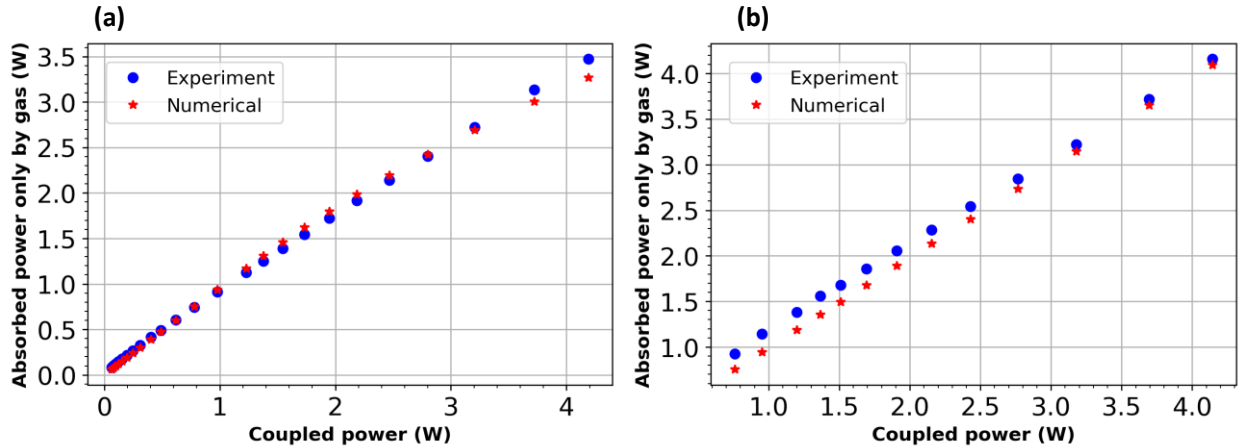


Figure 5.13 Comparison between numerical results and experimental results for absorbed power by acetylene gas as a function of coupled power (a) for gas pressure of 0.6 mbar (b) for gas pressure of 4.23 mbar.

The absorbed power by acetylene gas was calculated as a function of gas pressure for given input pump power. For this, 4.3 W was used as the input power depending on the availability of experimental data. Figure 5.14 shows the comparison between numerical and experimental results. According to the comparison, numerical results and experimental results are quite agree with each other. Even though numerical results underestimate/overestimate the absorbed power by gas, it predicted the behavior of absorbed power by gas as a function of gas pressure well. This quantitative discrepancy between numerical and experimental results could be due to errors that are associated with the experiment. For instance, the authors of Ref. [28] used scattered light from the side of the fiber to estimate the absorb energy by gas. If there was significant amount of scattered light from the side of the fiber this could mean that the bend loss associated with fiber is significant and the fiber loss at the pump wavelength should be higher than the reported value. This implies that both numerical and experimental values are overestimated, and the amount of overestimation for experimental data could be higher than the numerical values.

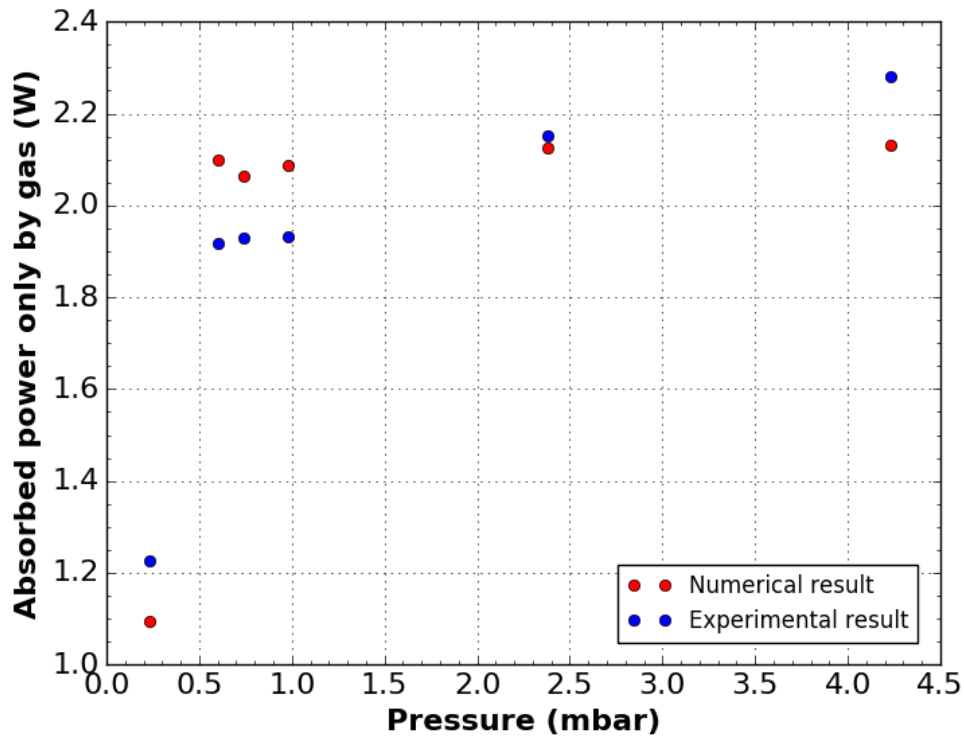


Figure 5.14 Comparison between numerical result and the experimental result of absorbed power by acetylene gas as a function of gas pressure. Input (coupled) power to the system is 4.3 W for all the data points.

Eventhough there is slight quantitative disagreement between numerical and experimental results in Fig. 5.14, qualitatively they have same behavior. Now we can extend this numerical analysis to pulsed acetylene filled HOFGLAS system and can study the feasibility of using it in a such a system.

To extend this discussion to pulsed acetylene filled HOFGLAS system I will consider the pulsed HOFGLAS system which was discussed in Ref. [27]. To extend the numerical analysis from the CW system to pulsed system we need to do a one major change to Python code. For the CW system Eq. 5.41 is solved for optical pump powers. But in pulsed HOFGLAS system we have to deal with the pulsed energies. Since we know the pulse duration of pump pulse is 1 ns we can calculate the peak pump power that is associated with a given pump pulse energy assuming a

Gaussian pulse shape. Then we will use this peak pump power as the initial condition and solve the Eq. 5.41. After the Eq. 5.41 is solved the results will be used to calculate the absorbed pump pulse energy by acetylene gas assuming that the pulse width does not change while propagating through the gas and fiber. This is a valid assumption, since the pump pulses are confined in the core of the fiber and dispersion that is associated with acetylene gas is negligible. Also the line strength 'S' and wavelength are changed according to the pump line.

The pulsed acetylene filled HOFGLAS system with 10.9 m long fiber is treated with this numerical model. More details about this HOFGLAS system can be found in Ref. [27] and discussed in Sections 1.1 and 3.1. One of the important factors to note down is, this HOFGLAS system was pumped at P(13) line and therefore the Python code is changed accordingly. The absorbed pump energies only by the gas are calculated as a function of gas pressure for given coupled pump pulse energies and they are compared to experimentally obtained values. Figure 5.15 shows the comparison between numerical and experimental data. Here, the numerical model clearly underestimates the amount of pump pulse energy absorbed by gas. But the numerical results qualitatively match with the experimental results.

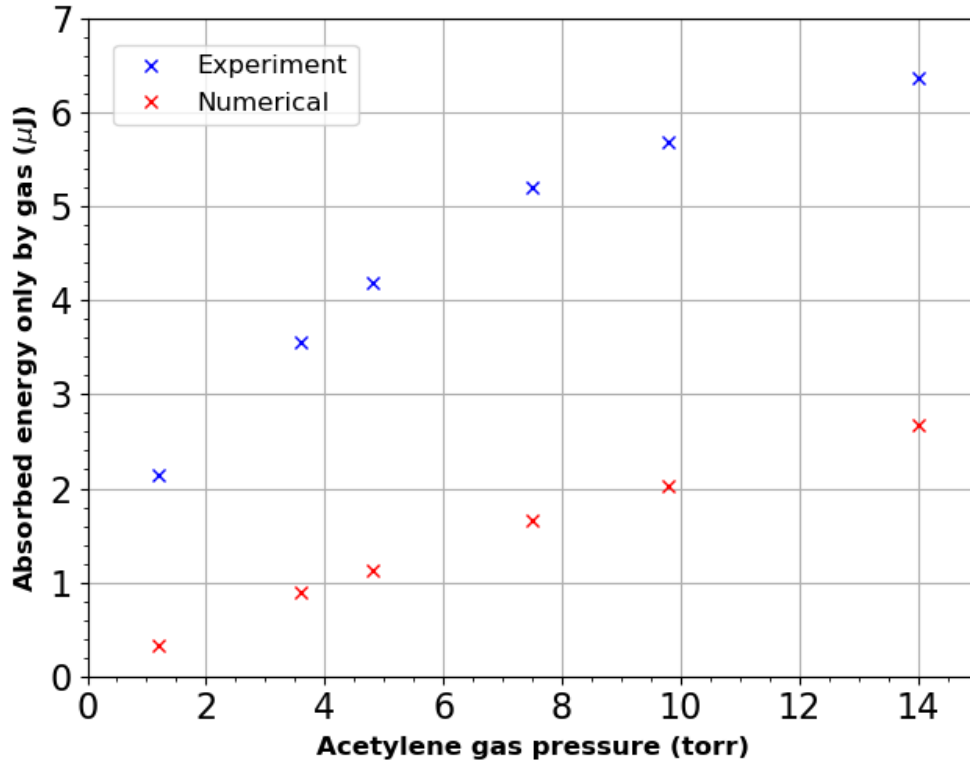


Figure 5.15 Comparison between numerical result and the experimental result of absorbed energy only by acetylene gas as a function of gas pressure for pulsed acetylene HOFGLAS system with fiber length 10.9 m. Coupled pulse energy to the system is $\sim 7.5 \mu\text{J}$ for all the data points.

The behavior of the absorbed energy only by gas can be explained as follows. The line profile $g(\nu - \nu_0)$ for this pressure regime is the Voigt profile. It is Doppler broadened by ~ 475 MHz and further broadened by 11 MHz/torr [38] due to acetylene gas pressure. Since Voigt profile is an area normalized function its peak will go down as it gets broader. Furthermore, since the absorption coefficient at the line center is proportional to the peak value of Voigt profile this pressure broadening eventually saturates absorbed energy/ power by acetylene gas. And Fig. 5.15 clearly reflects this saturation behavior in both experimental and numerical results.

Based on the comparison between experimental and numerical results, it seems like saturation power $P_s = 23$ mW is too small for high peak power limit. To get a better agreement

between experimental data saturation power P_s is scaled up by factor of 25 and obtained results are shown in Fig. 5.16.

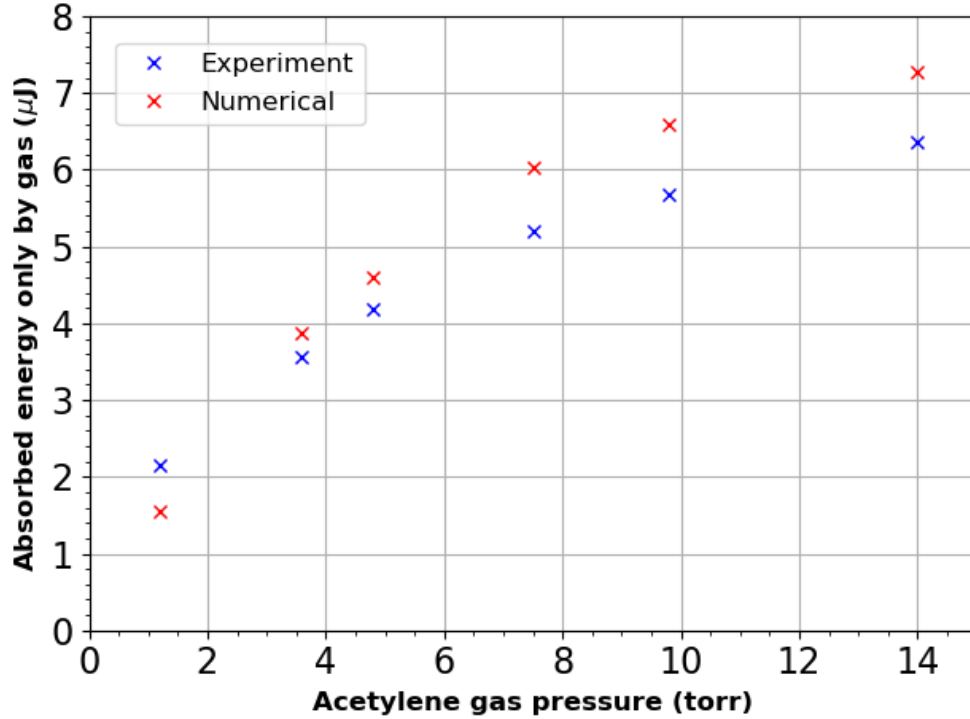


Figure 5.16 Comparison between numerical result and the experimental result of absorbed energy only by acetylene gas as a function of gas pressure for pulsed acetylene HOFGLAS system with fiber length 10.9 m. Here numerical results were obtained by scaling the saturation power by factor of 25. Coupled pulse energy to the system is $\sim 7.5 \mu\text{J}$ for all the data points.

By scaling up the saturation parameter we have a better agreement with experimental data but now absorbed energy by gas is overestimated specially for higher pressures. Based on this we would treat the saturation power as a free parameter for pulsed HOFGLAS system to estimate the energy absorbed by gas. Unlike for the CW acetylene HOFGLAS system, we had to change the saturation power when treating the pulsed acetylene HOFGLAS system with the above-mentioned numerical method. Underline root for this behavior may due to the difference in the linewidths of the pumps in both systems. In CW configuration the linewidth of the pump is in the order of few

100 KHz, while for pulsed configuration we have a pump linewidth of ~ 500 MHz. Therefore, more acetylene molecules can contribute the near-IR pump absorption in pulsed configuration than the CW configuration. But, in the numerical model we only considered the pump absorption at the line center for both cases. While, this method provides a good approximation for CW configuration we need to include the contributions from other frequencies away from the center frequency in order to get better agreement for the pulsed configuration. But, for now we will treat the saturation power as free parameter for pulsed configuration and leave the contribution from other frequency components as a future work.

As a summary, we introduced a numerical model to estimate the absorbed near-IR pump energy (power) only by acetylene gas at a given pressure. We compared the numerically obtained values with experimental values and found good agreement for CW lasing mechanism while using 23 mW as the saturation power. For the pulsed HOFGLAS system, even though numerical results showed the same qualitative behavior as the experimentally obtained values, numerical values are underestimated compared to the experimental values. A good agreement between numerical results and experimental results was found by reducing the saturation parameter by a factor of 25 (increasing the saturation power by a factor of 25). As discussed earlier the numerical model was based on a single frequency calculation. For pulsed pump source, we might need to include the contribution from the other frequency components. In Ref. [91], the authors have concluded that the spectral width of the pump beam has influenced on the absorption and therefore, it is worthwhile to include the contribution from the other frequency components in our numerical model for the pulsed HOFGLAS system.

Chapter 6 - New near-IR pump source

The mid-IR output energy our acetylene filled HOFGLAS system is currently limited by the available near-IR pump energy. We currently work with the highest near-IR output pulse energy we can get from the current OPA. Therefore, new near-IR pump source is needed to power scale the mid-IR output of the acetylene filled HOFGLAS system. This chapter is focused on designing and construction of a new near-IR pump source for the acetylene filled mid-IR HOFGLAS system. This new near-IR pump source is based on a two-stage OPA and design is discussed in the later part of this chapter. In the first part of the chapter I will discuss about the second order nonlinear optical frequency conversion and specifically will focus on the optical parametric amplification. Before constructing the two-stage OPA, numerical calculations are done to predict the total gain of the two-stage OPA based on the proposed design and the results of the numerical calculation are also discussed. Finally, the construction and the preliminary results of the two-stage OPA are reported.

6.1 Optical parametric amplification

The working mechanism of the OPA relies on the second-order nonlinear optical wave interaction inside a nonlinear medium. Generally, this second-order nonlinear process also called three-wave mixing since the involvement of three distinct fields [94]. The second harmonic generation (SHG) of the ruby laser with a quartz crystal [95] opened a new area in nonlinear optics, and since then researchers have demonstrated the generation of new spectral components via second-order nonlinear effects using a different kind of nonlinear materials/crystals. Mainly, there are three types of second-order nonlinear optical process. Namely, second harmonic generation (SHG), sum frequency generation (SFG) and difference frequency generation (DFG). These processes are

described schematically in Fig. 2.9. The subscripts p , s , and i indicate the pump, signal, and idler waves and are given based on the convention $\omega_p > \omega_s > \omega_i$. As in Fig. 2.9, SHG can be described as, single strong pump beam at the fundamental frequency ω_p is incident on nonlinear crystal and generates new a spectral component at second harmonic frequency $2\omega_p$. In the SFG process pump beam with a frequency ω_p and signal beam at a frequency ω_s are mixed inside the crystal to make the new spectral component at frequency $\omega_i = \omega_p + \omega_s$. The DFG process is somewhat similar to the SFG process but the new frequency component is $\omega_i = \omega_p - \omega_s$.

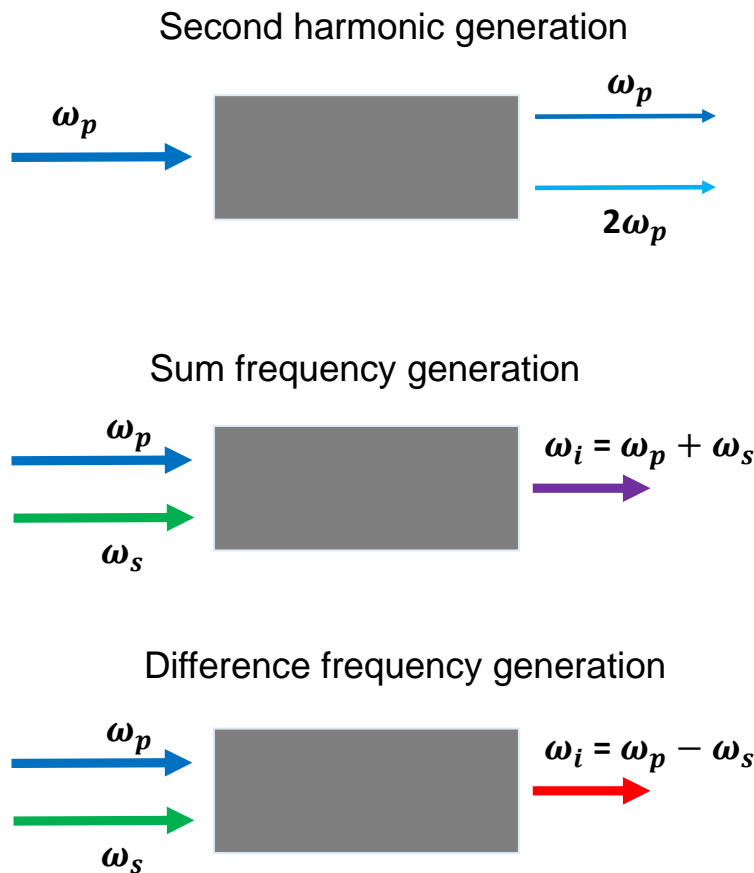


Figure 6.1 Schematic of various frequency conversion processes involving the second-order nonlinear process.

The process of optical parametric amplification (OPA) strictly depend on the process of DFG. In the OPA a strong pump wave and a relatively weak signal wave mix inside the nonlinear

crystal. Then, the signal wave is amplified through the DFG process, and the idler wave is generated to conserve the photon energy. This process is depicted in Fig. 2.10. As per the energy-level description in Fig. 2.10, to create a photon at idler frequency ω_i a photon at the higher frequency (pump) ω_p must be annihilated and a photon at the signal frequency ω_s must be created. And this process is stimulated by input weak signal wave, thus the signal wave is amplified by the process of DFG.

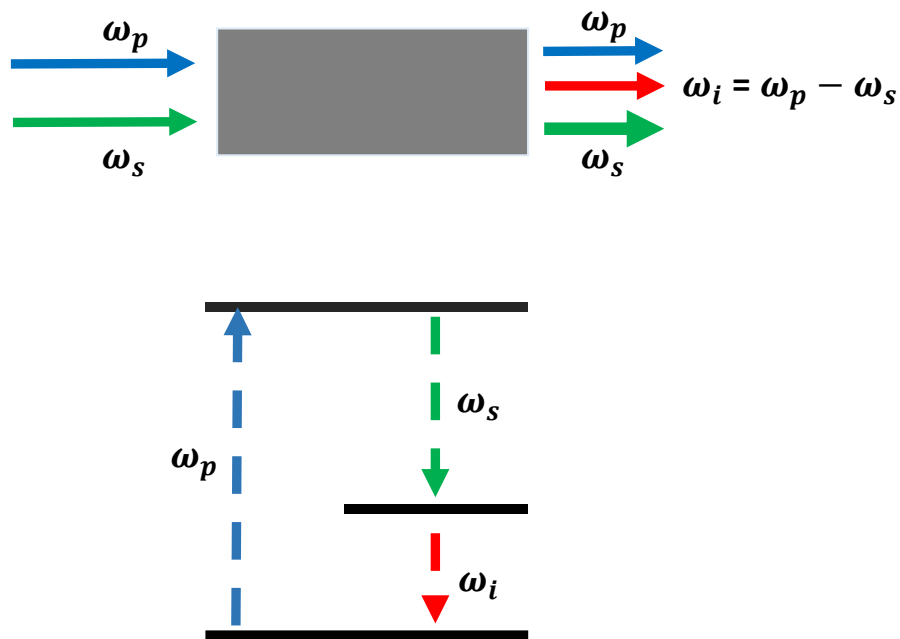


Figure 6.2 Optical parametric amplification. The interaction beams

The amount of parametric gain critically depends on parameters like the effective nonlinearity d_{eff} , length of the nonlinear crystal L , and the phase matching condition Δk . The effective nonlinearity d_{eff} depends on the symmetry relation of the nonlinear susceptibility, nonlinear crystals optical properties and orientation with respect to the fundamental input beams. The phase matching condition Δk represents the phase velocity mismatch between three waves that involved in the nonlinear process. To achieve the perfect phase matching condition pump

beam's wave vector should equal to the summation of the signal beam's and the idler beam's wave vectors. Figure 2.11 shows the parametric gain as a function of normalized propagation distance, for perfect phase match condition, the phase mismatch condition with $\Delta kL = 1$ and $\Delta kL = 10$. As per Fig. 2.11, it is obvious that to get higher gain (higher signal output) one need to minimize the phase mismatch Δk .

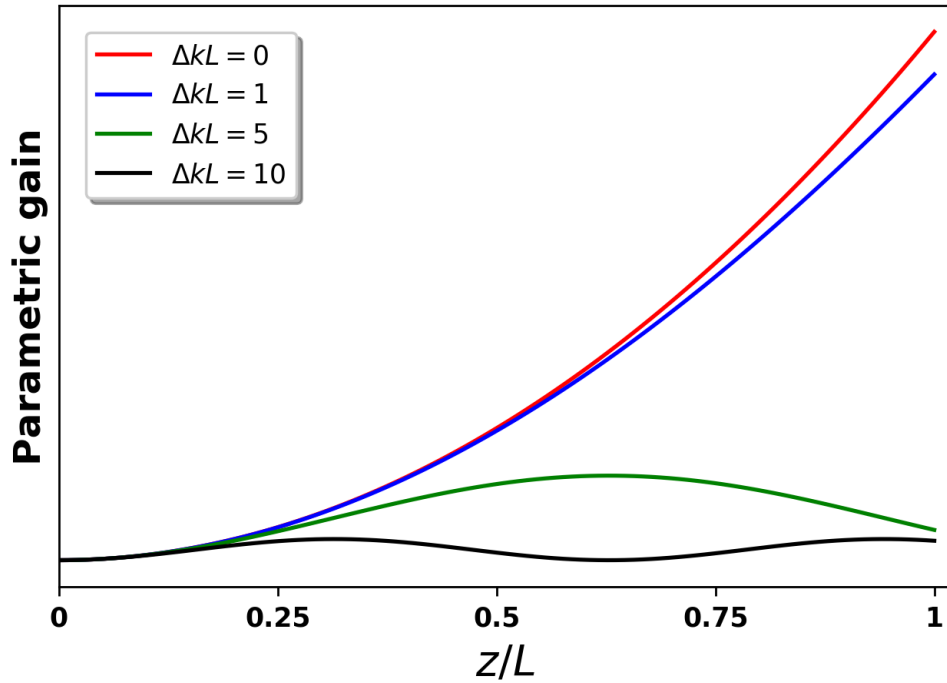


Figure 6.3 Parametric gain for different phase matching conditions as a function of normalized propagation distance along the nonlinear crystal. This is numerically generated using solutions available in Ref. [94].

The magnitude of the wave vector k of an arbitrary optical beam with frequency ω can be written as,

$$k = \frac{n\omega}{c} = \frac{2\pi n}{\lambda} \quad 6.1$$

where n is the index of refraction of the nonlinear crystal for the optical beam with vacuum wavelength λ . Then the perfect phase matching condition for the OPA process is given by [94],

$$\vec{k}_p = \vec{k}_s + \vec{k}_i \quad 6.2$$

Since the propagation direction for all the interacting beams are predefined, the magnitude of the phase mismatch can be written as,

$$\Delta k = k_p - k_s - k_i \quad 6.3$$

and, since the refractive index depends on the color, we can write Eq. 6.3 along with Eq. 6.1 as,

$$\Delta k = \frac{[n(\omega_p)\omega_p - n(\omega_s)\omega_s - n(\omega_i)\omega_i]}{c} \quad 6.4$$

then for perfect phase matching condition the quantity $[n(\omega_p)\omega_p - n(\omega_s)\omega_s - n(\omega_i)\omega_i]$ should equal to zero. But due to the normal or anomalous dispersion of the nonlinear crystal, it is not trivial to satisfy the above condition [62, 94]. However, the birefringence property of the nonlinear crystals allows us to satisfy the phase matching condition. The refractive index of a birefringent material depends on the frequency, polarization and the direction of propagation of a wave. For an example, in uniaxial crystals (have only one principle optic axis) there are two indices of refraction, called ordinary index n_o and extraordinary index n_e [94]. If the optical wave's polarization is perpendicular to the optic axis of the crystal, this wave said to be an ordinary wave and regardless of the propagation direction observes the ordinary index n_o . If the wave's polarization in parallel to the optic axis, then it sees the extraordinary index $n_e(\theta)$ and the refractive index depends on the angle θ , where the angle θ defined as the angle between the principal optic axis and the propagation direction [94]. Then by selecting appropriate polarizations with respect to the crystal's

optic axis and the propagation angle, one could obtain the perfect phase match condition (rather minimize the phase mismatch). Usually, this type of phase matching named as angle tuning phase matching due to the phase matching condition highly depends on the critical propagation angle θ_{pm} . Based on how the polarizations of interacting waves are rotated, there are two types of angle tuning phase matchings. If the pump and signal waves share the same polarization it refers as type I phase matching and if pump and signal wave's polarizations are orthogonally polarized, it is identified as type II phase matching. Depending on the each interacting wave's polarization designation as in Table 6.1 is used to name the interactions.

Table 6.1 Various polarization combination for type I and type II phase matching.

Type I			
Pump polarization	Signal polarization	Idler polarization	Shorthand notation
Extraordinary	Extraordinary	Ordinary	eeo
Ordinary	Ordinary	Extraordinary	ooe
Type II			
Extraordinary	Ordinary	Extraordinary	eoe
Extraordinary	Ordinary	Ordinary	eoo
Ordinary	Extraordinary	Extraordinary	oeo
Ordinary	Extraordinary	Ordinary	oeo

To find the phase matching angle θ_{pm} one should first know how the extraordinary wave's refractive index $n_e(\theta)$ changes with the propagation direction. If the wave's propagation direction makes angle θ with the optic axis of a uniaxial crystal, the extraordinary wave has a refractive index of [62, 94],

$$\frac{1}{n_e(\theta)^2} = \frac{\sin^2 \theta}{n_e^2} + \frac{\cos^2 \theta}{n_o^2} \quad 6.5$$

Then for perfect phase matching Eq. 6.4 can be reduced along with $\omega_p = \omega_s + \omega_i$ to,

$$\left(n(\omega_p) - n(\omega_i)\right)\omega_p - \left(n(\omega_s) - n(\omega_i)\right)\omega_s = 0 \quad 6.6$$

and Eq. 6.5 and Eq. 6.6 can be simultaneously used with various polarization combinations in Table 6.1 to find the phase matching angle θ_{pm} . The obtained values can be found in Table 10 at the second chapter of Ref. [94]. In some special situations, the phase matching angle is equal to the 90° . This special scenario typically is referred to noncritical phase matching (NCPM) and phase matching is usually achieved via the temperature phase matching [94]. The condition where the phase matching angle $\theta_{pm} \neq 90^\circ$ is then called critical phase matching (CPM). The refractive index of a material is also a function of temperature and is described by temperature-dependent Sellmeier equations [96, 97]. So, the phase matching condition can be achieved by tuning the crystal temperature with NCPM [94]. Sometimes, NCPM is favorable over CPM due to several reasons. Unlike the CPM, NCPM is less sensitive to the beam divergence. If the beam divergence is larger than the phase matching angle, it introduces additional phase mismatch and hence lowers the conversion efficiency. Furthermore, NCPM does not introduce beam walk-off like in CPM. The beam walk-off can severely reduce the overlapping between interacting beams and limits the beam sizes and the length of the crystal. The beam walk-off is a phenomenon that arises due to birefringence of the crystal. For an extraordinary wave, the direction of the propagation vector and the direction of the pointing vector (which defines the direction of energy flow) is not the same. Therefore, the ordinary and extraordinary beams will not entirely overlap along the whole length

of the crystal in both type I and type II CPM. On the other hand, for NCPM the spatial beam walk-off is negligible [94].

Phase matching angles for a biaxial crystal is not as simple as for the uniaxial crystal. Unlike for a uniaxial crystal, there are two optic axes in biaxial crystals. Therefore, the phase matching condition depends on two angles: θ and ϕ . If the crystal's principle axes are X, Y, Z , these two optic axes lie in the XZ plane and there are three indices of refractions as n_X, n_Y , and n_Z associate with each axis. For crystal with $n_X < n_Y < n_Z$, these two optic axes lie symmetrically around the Z - axis with an angle Ω with respect to the Z -axis. These angles are illustrated in Fig. 6.4 and the angle Ω is given by Eq. 6.7 (a). For crystal with $n_X > n_Y > n_Z$, the optic axes make angles Ω' with Z -axis and are given by Eq. 6.7 (b). And, in Fig. 6.4 the angle Ω is replaced by Ω' for the above situation [94].

$$\sin \Omega = \frac{n_Z}{n_Y} \left(\frac{n_Y^2 - n_X^2}{n_Z^2 - n_X^2} \right)^{1/2} \quad 6.7 (a)$$

$$\cos \Omega' = \frac{n_X}{n_Y} \left(\frac{n_Y^2 - n_Z^2}{n_X^2 - n_Z^2} \right)^{1/2} \quad 6.7 (b)$$

If wave with a wave vector \vec{k} travels in biaxial crystal with at an angle θ with the Z -axis and an azimuthal angle ϕ , as depicted in Fig. 6.4, the indices of refraction for the allowed two propagation modes can be found by solving the following Fresnel equation.

$$\frac{\sin^2 \theta \cos^2 \phi}{n^{-2} - n_X^{-2}} + \frac{\sin^2 \theta \sin^2 \phi}{n^{-2} - n_Y^{-2}} + \frac{\cos^2 \theta}{n^{-2} - n_Z^{-2}} = 0 \quad 6.8$$

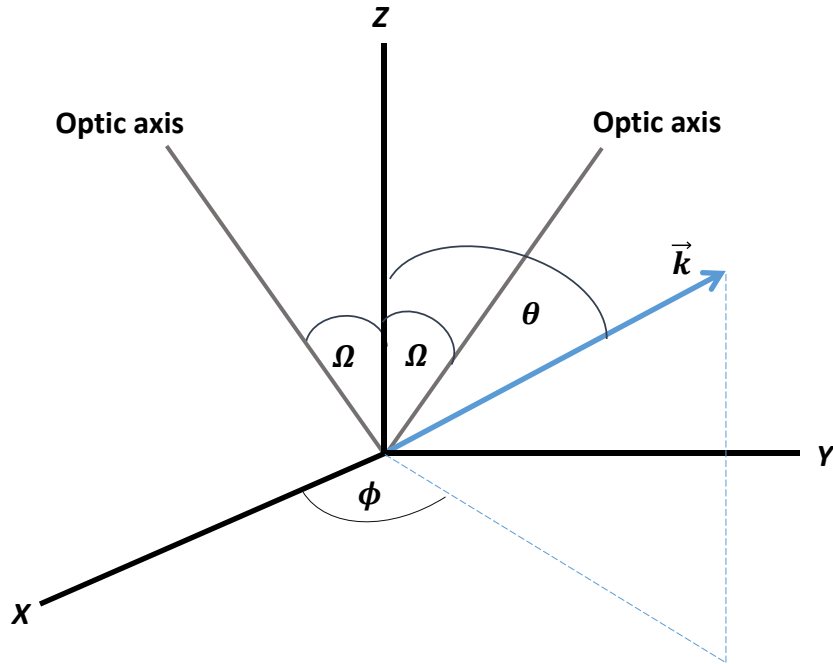


Figure 6.4 Wave propagation in biaxial crystal's coordinate system.

The solutions to the Eq. 6.8 relate to the two orthogonal modes of propagation in the direction of (θ, ϕ) . In a biaxial crystal, unless the propagation is in the principal planes, these two orthogonal modes are neither extraordinary nor ordinary. For a biaxial crystal, in type I phase matching the pump and signal wave's polarizations are parallel to each other while they are orthogonally polarized in type II phase matching [94]. Then the Eq. 6.8 can be used along with Eq. 6.6 to determine the phase matching angles for type I and type II conditions. Usually, solving these equations for the biaxial crystal is more complex than for a uniaxial crystal. The phase matching angles can be obtained numerically using available software packages such as SNLO [106] easily. But analytical solutions are possible if the propagation is confined to the principal planes of the crystal. One can find the phase matching angles by using relevant formulas available in Tables 16, 17 and 18 at chapter 2 of Ref. [94]. Potassium titanyl phosphate (KTiOPO_4) also known as KTP crystal is a biaxial crystal and phase matching angles for a specific OPA process will be calculated in section 6.2.

Even though angle tuning phase matching is a widely used technique, there are some drawbacks associated with it. As discussed earlier beam divergence and spatial walk-off add limitations for the crystal length, and some angles of propagation are not possible [94]. Also, some nonlinear crystals do not show enough birefringence nor have birefringence (for optically isotropic crystal structure) that need for angle tuning. For example, even though gallium arsenide (GaAs) is a semiconductor with high nonlinear coefficients, angle tuning phase matching is not possible due to its optically isotropic property [98]. Furthermore, the diagonal elements in the nonlinear susceptibility tensor are usually higher than the off-diagonal elements [62], but diagonal elements are only accessible when the fundamental interacting beams share the same polarization. Therefore, diagonal elements are inaccessible with angle tuning. For an example, lithium niobate (LiNbO₃) has an off-diagonal nonlinear optical coefficient of $d_{31} = -4.52$ pm/V whereas, diagonal nonlinear optical coefficient of $d_{33} = 31.5$ pm/V [99]. The technique known as quasi-phase-matching (QPM) allows to access these diagonal elements by having the same polarization state for the interacting beams [94]. This method was first suggested by Armstrong *et al.* [100] in 1962. They suggested that the QPM can be achieved by dividing the nonlinear medium into thin sections and then rotating each section by 180°. Figure 6.5 shows the idea of QPM. Here, the material divided into thin sections with the same size and is periodically poled such a way that the nonlinear coefficient d_{eff} changes its sign between each segment. The period Λ is equal to the twice of coherent length L_{coh} , where L_{coh} is given by Eq. 6.9 and is the distance that waves should travel to generate the desired spectral component [94].

$$L_{coh} = \frac{\pi}{|\Delta k|} \quad 6.9$$

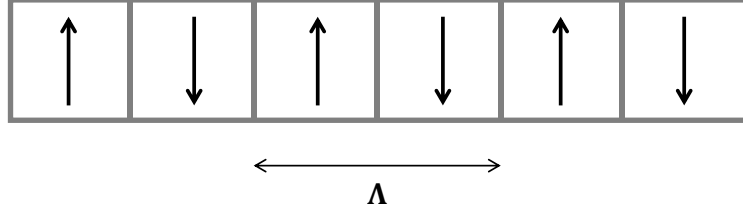


Figure 6.5 A schematic of a periodically poled material with the orientation of crystalline axes changes between each segment.

For the first-order QPM, the effective nonlinearity is lowered by a factor of $\left(\frac{2}{\pi}\right)$ than the phase matching achieves with the angle tuning. But, the diagonal elements of the nonlinear susceptibility tensor are accessible with the QPM and one can utilize higher effective nonlinearity with the QPM than the angle tuning hence higher conversion efficiencies with the QPM [94]. For the OPA process with a first order QPM crystal phase mismatch can be written as [62],

$$\Delta k = k_p - k_s - k_i - \frac{2\pi}{\Lambda} \quad 6.10$$

and the optimum poling period for a given interaction can be found by equaling the Eq. 6.10 to zero, i.e., imposing the perfect phase matching condition. This yields us,

$$\Lambda = \frac{2\pi}{k_p - k_s - k_i} \quad 6.11$$

6.2 Two-stage OPA

As I discussed in chapter 3, the laser signal saturation is removed from the acetylene filled HOFGLAS system by using a ~ 8 m long hypocycloidal kagome structured HCPCF with acetylene gas pressures above 2 torr. Also, linear dependence between produced mid-IR energy and absorbed near-IR energy by acetylene gas observed. Furthermore, produced mid-IR pulse energy only

limited by the available near-IR pump energy. With the available near-IR pump source the maximum near-IR pump pulse energy we can get is 21 μJ . More pump energy can be obtained by pumping the existing near-IR OPA with higher pump pulse energies. Even though Nd:YAG laser which is the pump laser for the OPA is capable of producing energy of 3 mJ per pulse we use only 200 μJ out of it due to damage threshold and the aperture size of the PPLN crystal. So new near-IR pump source is needed to test the limits of acetylene HOFGLAS system under current configurations.

We have looked for several options as the higher power (energy) near-IR pump source. One possible way is to replace the current PPLN crystal by another PPLN crystal with a larger aperture. This gives us the ability pump the OPA with higher Nd:YAG energy to get higher near-IR output energy. Replacing the current PPLN crystal with a larger aperture PPLN crystal is not feasible solution for us due to limitation in the budget. Buying a new PPLN crystal with a larger aperture is an expensive step, since this includes growing a new crystal and poling it with required poling periods. Replacing the PPLN crystal with a bulk nonlinear crystal is not a viable solution too. For bulk crystal phase matching condition is usually achieved by angle tuning method. As discussed in section 6.1, the effective nonlinearity (d_{eff}) accessible with angle tuning is usually less than the effective nonlinearity that can be attainable with quasi phase matched condition. And the conversion efficiency is directly proportional to d_{eff}^2 [94]. Therefore, it is clear that there is no advantage of using a bulk crystal instead of the existing PPLN crystal.

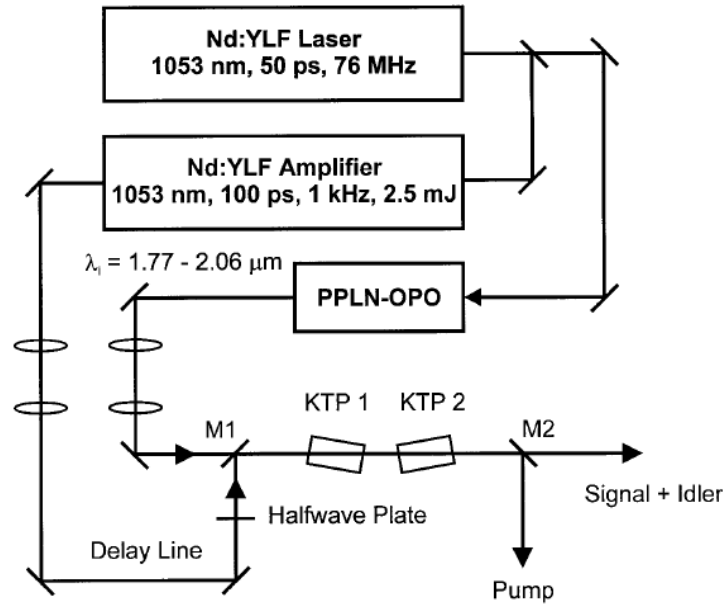


Figure 6.6 The schematic of the tunable, high-power near-IR two stage OPA using two KTP crystals. Adapted from Ref. [101].

Tunable, high-power near-IR radiation by an OPA has been demonstrated by Finsterbusch and coworkers using two potassium titanyl phosphate (KTP) crystals [101]. There, picosecond pulses from an Nd:YLF regenerative amplifier at 1053 nm with repetition rate of 1 kHz is used as the pump source and near-IR output from synchronously pumped frequency-stabilized optical parametric oscillator (OPO) is used as the seed source. The OPO is based on a PPLN crystal. Then the seed and pump beams are focused on the first KTP crystal and then the amplified seed and residue pump beams are sent through the second KTP crystal which is orientated in walk-off compensation geometry. Both KTP crystals are uncoated, 15 mm long with an aperture of 5×5 mm² and cut to phase matching angles of $\theta = 54^\circ$ and $\phi = 0^\circ$. And, type II phase matching at x - z plane is used. Figure 6.5 shows the schematic of the experimental setup. The signal beam is tunable between 1780 and 2020 nm and idler has tunability range from 2200 to 2580 nm. By using pump pulse energy of 2.3 mJ authors were able to obtain 400-500 μ J pulse energies for signal beam and 350-400 μ J pulse energies for idler beam with total conversion efficiency of 37%.

By motivated from above described work, a two-staged OPA is designed to amplify the near-IR pulse energy of our current OPA. As mentioned earlier, even though our Nd:YAG laser has capability of producing 3 mJ of energy per one pulse we used only 200 μJ out of it to pump the current OPA and rest of the pulse energy is dumped. The main idea for the two-staged OPA is, use 200 μJ of Nd:YAG pulse energy to pump the current OPA and use previously dumped energy to pump the second stage. The near-IR output from the existing OPA will be used as the seed beam for the second stage and a suitable bulk crystal will be used as the nonlinear crystal for the second stage.

We decided to use a bulk KTP crystal as the nonlinear crystal for the second stage of the OPA due to it has a good optical transparency in the wavelength region we are interested in, and good nonlinear optical properties [102]. The KTP crystal has good optical transparency from 0.35 μm to 4.5 μm and is widely used in frequency doubling of the Nd lasers at 1 μm [103]. Bulk KTP crystals have been used in OPAs at near-IR [101, 104], in OPOs at IR [105], and OPOs at mid-IR [106] with good conversion efficiencies. KTP is biaxial crystal and the phase matching condition for a given interaction is depends on the propagation plane of the crystal. The calculation of the phase matching angels for our desired OPA interaction is discussed in next section.

6.2.1 Phase matching condition of bulk KTP crystal for near-IR OPA operation

For bulk nonlinear crystals the common way to achieve the phase matching condition is through the angle tuning the crystal. This method was discussed in detail at section 2.3. We need to find the phase matching condition for the interaction of converting pump photon at 1064 nm to a photon at signal wavelength 1532 nm and to a photon at idler wavelength 3483 nm. The phase mismatch for this interaction is given by Eq. 6.4 and for perfect phase matching the quantity

$[n(\omega_p)\omega_p - n(\omega_s)\omega_s - n(\omega_i)\omega_i]$ should equal to zero. The procedure of finding the phase matching angles for biaxial crystal is not a trivial process. The procedure is well discussed in Ref. [94], and one can use numerical software to calculate the phase matching conditions more easily. First, I used a free version of SNLO program which has been developed by AS-Photonics [107] to calculate the phase matching conditions for the OPA process we are interested in. Then, the phase matching conditions are verified through a manual calculation with details available in Ref. [94]. With SNLO, phase matching angles of $\theta = 44.5^\circ$ and $\phi = 0^\circ$ are obtained for the x - z propagation plane under type II phase matching condition. And 353 K is used as the crystal temperature. Under these conditions the effective nonlinearity has a value of 2.27 pm/V. And, the walk-off angle is ~ 48.5 mrad (3°). Unfortunately, this walk-off angle limits the overlap between interacting beams. Then calculations are carried out again by considering propagation in x - y plane. This provides with angles $\theta = 90^\circ$ and $\phi = 63.4^\circ$. This gives us about the same effective nonlinearity but more importantly both pump and signal beams have almost same beam walk-off angles. To check the validity of calculations done with SNLO, I recalculated the phase matching conditions for propagation in x - z plane using equations in table 16 on page 68 of Ref. [94].

The phase matching angles for biaxial crystal are defined as in Fig. 6.4. For propagation in x - z plane the angle ϕ is zero. The perfect phase matching condition only can be attained via the type II condition. So, pump and signal beam should have orthogonal polarizations. And, to find the phase matching angle θ_{pm} following equations are used [94].

$$\tan^2 \theta_{pm} = \frac{1 - V}{V - Y} \quad 6.12$$

where,

$$V = \frac{B^2}{(C - A)^2} ; Y = \left(\frac{B}{E}\right)^2 \quad 6.13$$

and A, B, C and E are given by,

$$A = \frac{n_{p,Y}}{\lambda_p}, B = \frac{n_{s,X}}{\lambda_s}, C = \frac{n_{i,Y}}{\lambda_i}, E = \frac{n_{s,Z}}{\lambda_s} \quad 6.14$$

As usual the subscripts $p, s,$ and i stand for pump, signal and idler. The subscripts X, Y and Z in refractive indices indicate the indices in respective directions at given wavelengths. Then the respective refractive indices are calculated using Sellmeier equations for KTP crystal available in Ref. [108]. All of these calculations were done using a python script and a copy of the script can be found in the appendix. The calculated phase matching angles are $\theta = 43.11^\circ, \phi = 0^\circ$ and well matched with angles found with SNLO. To find the effective nonlinear constant following equation is used [94].

$$\begin{aligned} d_{eff} = & (d_{32} - d_{31})(3 \cos^2 \delta - 1) \sin \theta \cos \theta \sin 2\phi \sin \delta \\ & - 3(d_{31} \cos^2 \phi + d_{32} \sin^2 \phi) \sin \theta \cos^2 \theta \sin^2 \delta \cos \delta \\ & - (d_{31} \sin^2 \phi + d_{32} \cos^2 \phi) \sin \theta \cos \delta (3 \cos^2 \delta - 2) \\ & - d_{33} \sin^3 \theta \sin^2 \delta \cos \delta \end{aligned} \quad 6.15$$

The angle δ is defined as follows.

$$\cot 2\delta = \frac{(\cot^2 \Omega \sin^2 \theta - \cos^2 \theta \cos^2 \phi + \sin^2 \phi)}{\cos \theta \sin 2\phi} \quad 6.16$$

Since for KTP crystal $n_X < n_Y < n_Z$, the angle Ω is given by,

$$\sin \Omega = \frac{n_Z}{n_Y} \left(\frac{n_Y^2 - n_X^2}{n_Z^2 - n_X^2} \right)^{1/2} \quad 6.17$$

Then, the d_{eff} is calculated using above mentioned phase matching angles and obtained value of -2.6 pm/V is fairly matched with the SNLO output value.

6.2.2 Numerical calculation to predict the gain of two-stage OPA

After the phase matching angles and the effective nonlinearity are obtained the next step is to predict the total gain achievable with the two –stage OPA. Again, SNLO software is used to calculate the total gain. First, the interacting beams are treated as plane waves. Secondly, both the pump and signal beams are considered as pulsed. Then the $21 \mu\text{J}$ is used as the input signal pulse energy. Unfortunately, even though our pump laser, the Nd:YAG laser has an energy of 3 mJ per pulse, significant amount of energy is lost to the faraday isolator and only about 1 mJ is available for to pump the both PPLN and KTP crystal. Out of that $200 \mu\text{J}$ should be used to pump the PPLN and we have only about 0.98 mJ to pump the KTP crystal. The beam diameters are set to be 1 mm based on the damage threshold of the KTP crystal and crystal's input face is treated as AR coated. Then the output energies for respective beams are calculated for crystal length of 2.5 cm. The input and output irradiances are shown in Fig. 6.7. The calculated output values are $71 \mu\text{J}$ for signal and 0.88 mJ for pump. And this gives additional 5 dB signal gain from the second stage of the OPA. By decreasing the both pump and signal beams to beam diameter of 0.75 mm we can increase the signal output to $120 \mu\text{J}$, which is equivalent to additional gain of 7.5 dB.

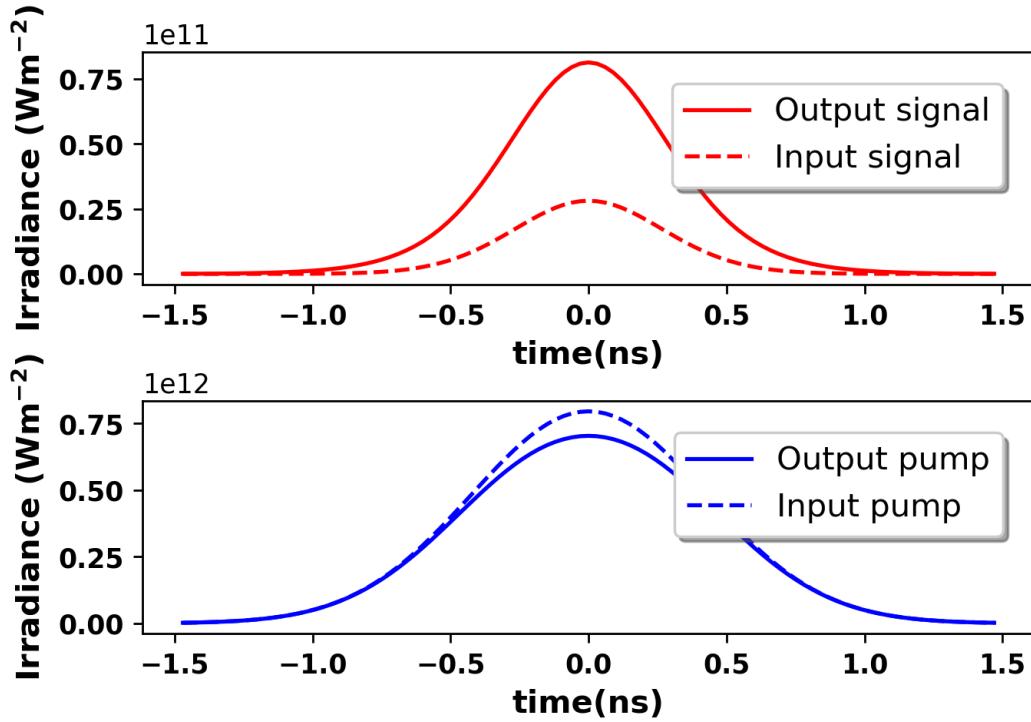


Figure 6.7 Input and output intensities from SNLO calculation for signal beam (top) and pump beam (bottom). The pump beam is depleted, and signal beam is amplified.

6.2.3 Experimental setup of two stage near-IR OPA

Based on the SNLO calculations we can get at least 5 dB additional gain for the near-IR pulse energy. Therefore, we bought a 2.5 cm long KTP crystal and simple schematic of proposed experimental setup is shown in Fig. 6.8. Here, the first stage of the OPA consists with the current PLLN crystal and works as the pre-amplifier and the second stage comprises the 2.5 cm long KTP crystal and works as the power-amplifier. First, a beam splitter with 80% reflection efficiency and 20% transmission efficiency is used to split the YAG beam into two parts. The 20% of YAG beam corresponds to $\sim 200 \mu\text{J}$ and is used to pump the PPLN crystal and 80% of YAG beam ($\sim 0.8 \text{ mJ}$) is used to pump the KTP crystal. A delay line is used in the 80% YAG beam path to achieve the temporal overlap between pump and signal beam at the KTP crystal's input facet. And two

telescopes are used in the respective beam arms to minimize the beam widths to 1 mm. And a dichroic mirror is used in front of the KTP crystal to spatially combine the pump beam and the near-IR output from the first stage of the OPA. A half-wave plate is used in the near-IR beam path to rotate the polarization of the near-IR output of the first stage OPA. At the end of the KTP crystal, long-pass filter is used to filter out the amplified near-IR signal beam from residue pump and the produced idler beam. All the optics used in the setup are AR-coated for maximum transmission of pump and signal beams. KTP crystal is mounted on a heater to reduce the gray tracking effect at higher powers and heater is operated at 80°C. And both the crystal and the heater are mounted on a rotational stage since angle tuning is required to minimize the phase mismatch.

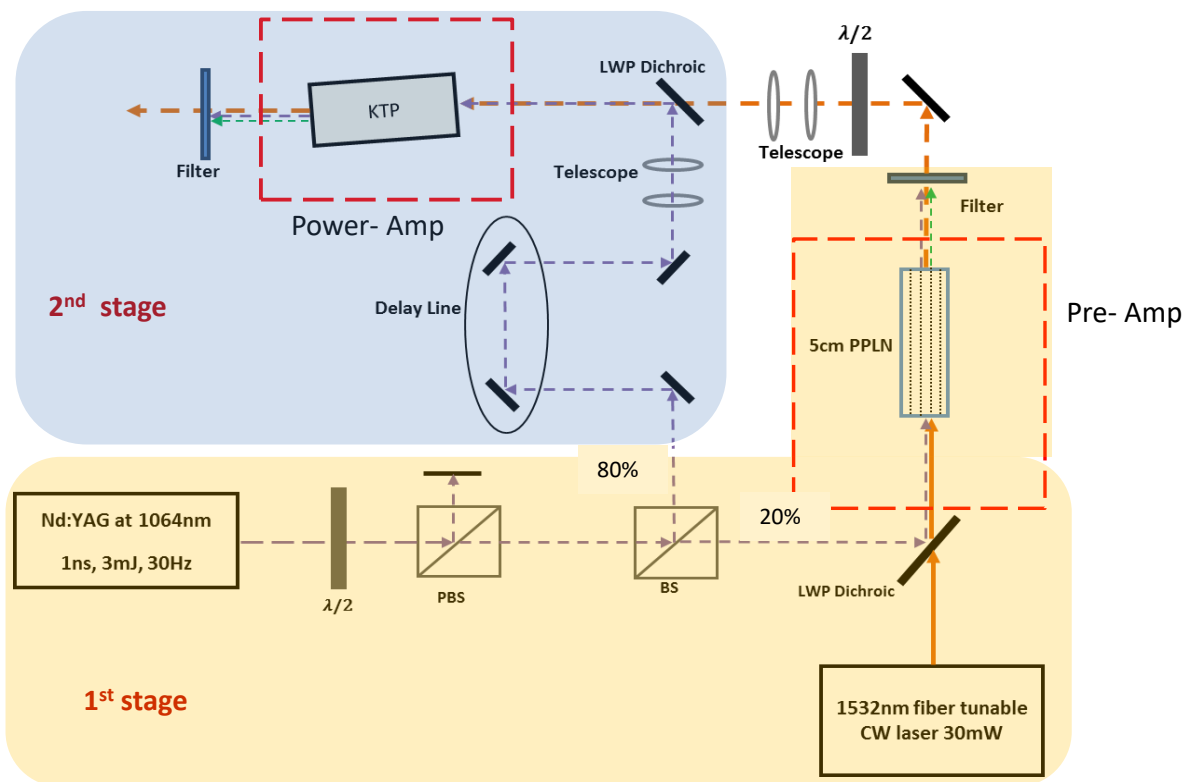


Figure 6.8 A simple schematic of the two-stage OPA. The existing OPA is used as the pre-amplifier in the first stage of the OPA and the bulk 2.5 cm long KTP crystal is used in the second stage as the power-amplifier.

6.2.4 The alignment procedure and preliminary results of two stage OPA

The KTP crystal we received from the seller is cut to propagation in x - z plane and phase matching angles are $\theta = 44.5^\circ, \phi = 0^\circ$. For this specific crystal cut type II phase match should be used. Therefore, orthogonal polarizations for pump and signal beams are made sure by using a polarizer just before the KTP crystal. The phase matching angles are cut with respect to the crystal's axes. First, crystal is rotated the B-axis as in Fig. 6.9 to match the polarization states of beams with the crystal's axes. Secondly, the crystal should rotate around the A-axis as in Fig. 6.4 to achieve the phase matching angles with respect to the beams.

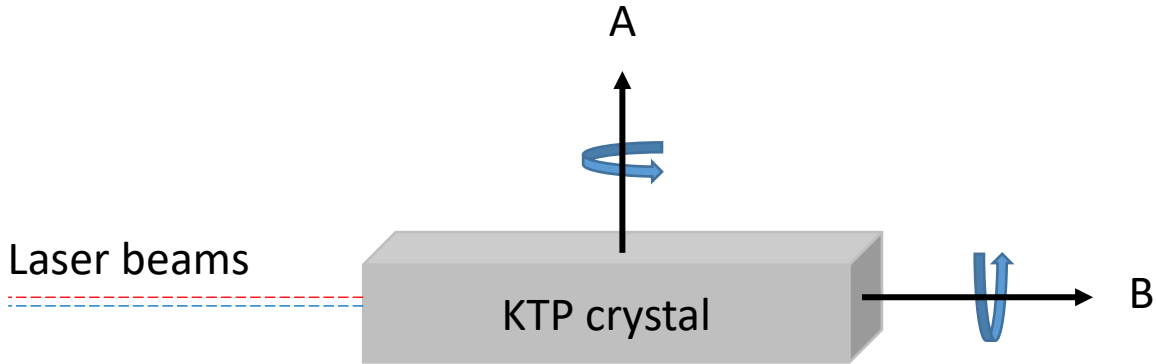


Figure 6.9 Alignment of KTP crystal respect to the laser beams. Rotate around B-axis to match polarizations and rotate around A-axis to achieve phase matching angles.

Even before place the KTP crystal in the setup, temporal overlapping of pump and signal beams are verified. Both beams are focused on to a fast photodiode (rising time ~ 1 ps) and the intensity tracers are observed using a fast enough oscilloscope (Tektronic:). The delay line on the pump beam arm is moved until acceptable temporal overlapping is observed. Then the KTP crystal is placed in the setup and crystal is rotated around the axis B until the correct polarizations are achieved. To check this, first orthogonal polarization states for pump and signal beam are set. Then, only the signal beam is propagated through the KTP crystal and a polarizer is placed after the crystal. The signal beam's intensity after the polarizer is monitored while rotating the KTP

crystal around B- axis and rotation is stopped once the minimum intensity is observed. Then the pump beam is propagated through the crystal and made sure that it still has an orthogonal polarization to that of signal beam after the KTP crystal (This should be done with a low pump energy to protect the polarizer). Once the polarization is set, the KTP crystal is pumped with available maximum pump pulse energy and crystal is rotated around the A-axis until the amplified signal is observed. Once some amplification is observed delay line will be adjusted in order to achieve optimal temporal overlap.

Even though we extensively worked on the alignment of the second stage OPA we only obtained 26 μJ of near-IR pulse energy out from the two stage OPA. The measured near-IR pulse energy is few orders less than the amount predicted by the numerical calculation. The numerical calculations are verified few times by redoing it and no faults are found. Also, experimental procedure also verified few times to make sure that there are no critical errors associated with it. The problem lies within the crystal cut angles. In the numerical calculation I used propagation in x - y plane since it provides same beam walk-off angles for both pump and signal beam. So, the overlapping between interacting beams should fairly preserved. Due to that long wave approximation is used to predict the gain. But, the KTP crystal we received from the seller is cut to propagation in the x - z plane. This introduces significant beam walk-off between pump and signal beam and limits the beam overlapping throughout the crystal. So, long plane wave approximation is no longer valid. To predict the gain under beam walk-off condition two-dimensional long pulse mixing in the SNLO must use. Under this condition numerical simulation gave us only 34 μJ as the amplified signal output. So, the amplification we obtained with the two stage OPA is consistent with the numerical calculations and unfortunately the current KTP crystal is not useful to amplify the near-IR pulses.

Chapter 7 - Summary and outlook

7.1 Summary

The efforts reported in this thesis are to power scale an acetylene-filled mid-IR HOFGLAS system. A 7.6 m long kagome-structured HCPCF is used in the system, and mid-IR laser performance is studied with gas pressures of 1 – 14 torr. As a result, we were able to remove the laser signal saturation that has been observed in previous studies [27]. Moreover, we observed a linear dependence between produced mid-IR energy and the absorbed near-IR pump energy by acetylene gas. We also studied the effect of pump wavelength on mid-IR laser performance by exciting the acetylene molecules via two distinct pump wavelengths and showed the effect of pump wavelength is negligible as long as the line strengths associated with pump wavelengths are almost the same. Also, the observed mid-IR laser efficiency is independent of the acetylene gas pressure, and this reflects that the mid-IR laser efficiency is not limited by the intermolecular collisions. Furthermore, we measured the highest mid-IR pulse energy of 2.56 μJ when the acetylene molecules are at 13.6 torr via the P(9) absorption line and this is the highest ever mid-IR pulse energy that has been observed with a HOFGLAS system to the best to our knowledge. By comparing our acetylene mid-IR HOFGLAS efficiency to that of diode-pumped mid-IR HOFGLAS system [23], we concluded that the near-IR pump source with a shorter pump pulse width is suitable to maximize the output mid-IR energy by reducing the intermolecular collisions. We designed an experiment to perform a beam quality measurement for the mid-IR output beam of the acetylene filled HOFGLAS system based on an M^2 measurement and showed the mid-IR output beam is nearly diffraction-limited and have an M^2 value of 1.15 at the highest mid-IR pulse energy.

We also proposed a numerical model to estimate the absorbed near-IR pump power/energy only by acetylene gas in the HOFGLAS system. This numerical model is based on the saturated absorption of an inhomogeneous line profile. By solving the numerical model using we obtained the absorbed near-IR pump pulse energy only by acetylene gas. We were able to get a good agreement with numerical and experimental values for a CW HOFGLAS by using 23 mW as the saturated power for acetylene. But, we were unable to find a good agreement between numerical and experimental values for the pulsed HOFGLAS system with this saturated power, and we had to treat it as a free parameter to find a good agreement.

A new near-IR pump source is designed and built to access higher pump pulse energies for acetylene HOFGLAS system. The design is based on a two-stage OPA and first stage work as the pre-amplifier and second stage work as the power amplifier. Even though we expect to see an additional 5 dB gain from the second stage of the OPA, no significant gain is observed due to beam-walk associated with the KTP crystal

7.2 Outlook

The maximum theoretical optical-to-optical conversion efficiency that can be obtained from acetylene mid-IR HOFGLAS system is 33%. But the maximum conversion efficiency obtained with the current work is 27%. One reason for this is the fiber loss at the lasing wavelength. So, one possible future work is that trying shorter HC-PCF with a higher acetylene gas pressure in the HOFGLAS system. Also, if we look at the energy level diagram for the mid-IR lasing in acetylene, once the molecules are pumped to upper lasing state and relaxed to the ν_1 vibrational manifold, they cannot move back to the ground vibrational state via radiative process since it is not allowed by the dipole rules. The only way to go back to ground state is either intermolecular collisions or

collisions with the fiber wall. Therefore, this creates a bottle-neck condition for the mid-IR lasing and the population in $J = 12$ rotational state of $\nu_1 + \nu_3$ builds up without making mid-IR lasing transitions to the ν_1 vibrational manifold. Then, those molecules may undergo intermolecular collisions to release their additional energy without making additional mid-IR energy and reduces the mid-IR laser efficiency. Introducing a suitable buffer gas to the acetylene filled HOFGLAS system may help us to remove the bottle-neck condition between the two lasing states and would increase the efficiency of the system. But, the addition of buffer gas may create new problems if we are not careful about the gas concentrations. Buffer gases could potentially add an additional broadening factor to the acetylene's absorption line profile, hence could limit the overlap between acetylene's absorption line profile and the pump source linewidth. So, studying about the effect of buffer gas on mid-IR lasing in acetylene HOFGLAS system is an interesting possible future work.

Dual-comb spectroscopy gained a lot of attention in the past few years and allows researchers to apply the coherence, resolution, and accuracy of frequency combs for precision molecular spectroscopy. As mentioned in Chapter 1 trace gases have fundamental ro-vibrational transitions at the mid-IR region. Therefore, the mid-IR dual comb could be a versatile tool for detecting these trace gases. Nowadays, researchers are focused on making dual-combs in the mid-IR region by employing different techniques like fiber lasers, electro-optic modulators, OPOs, and silicon-based micro resonators [109-112]. Since the acetylene filled HOFGLAS system lases at 3 μm and CW lasing is observed, it is possible to make a frequency comb at 3 μm region with the acetylene filled HOFGLAS system. The formation of the frequency comb is associated with a train of ultrashort laser pulses, and these pulses usually have pulse widths on the order of femtoseconds. So, if we can generate ultrashort pulses with the acetylene filled HOFGLAS system, we might be able to produce compact, robust, fiber-based dual combs at the mid-IR region.

The generation of ultrashort pulses depends on the mode-locking technique. In mode-locking operation, the phases of the longitudinal modes are locked, and constructive interference happens periodically [113]. To generate an ultrashort pulse with the mode-locking technique, the laser gain medium should have wide absorption and emission (gain) bandwidths. As per Fig. 2.2, acetylene has 50 absorption lines near 1.5 μm and the bandwidth is ~ 35 nm. By increasing the acetylene gas pressures up to atmospheric pressure, we can overlap absorption lines since they will be pressure broadened. This allows us having large absorption and emission bandwidths. Then with a proper CW pump source, we can excite almost all the acetylene absorption lines near 1.5 μm and can get a larger number of emission frequencies (larger gain bandwidth) that is required for the mode-locking. Then properly choosing a saturable absorber in the mid-IR region we can obtain an ultrashort pulse by discriminating the CW lasing. This way it is possible to make a frequency comb at mid-IR using the acetylene HOFGLAS system.

Another interesting future direction would be pushing the HOFGLAS system to the longer wavelength mid-IR region. Even though, the mid-IR lasing at 4.6 μm is observed by using N_2O in a HOFGLAS system [31] the mid-IR laser efficiency is low due to higher fiber loss at the lasing wavelength. Therefore, one needs to optimize the fiber structures of HC-PCFs to guide light with low loss multi-octave guidance to push the HOFGLAS systems to the longer wavelengths. The optically pumped gas lasers have demonstrated mid-IR lasing by using molecules like CO_2 , CO, HBr as the gain medium[15-18]. So, it is possible to make mid-IR HOFGLAS systems using them with a proper HC-PCF. Other than the silica-based HC-PCFs, the ones made with other types of glasses have shown multi-octave guidance from UV to the mid-IR region with lower losses. Microstructured photonic crystal fibers that are made with ZBLAN glass or chalcogenide glasses (sulfides, selenides or tellurides) have been used to generate and guide light at the mid-IR region.

For instance, supercontinuum generation from UV to mid-IR is observed using a solid-core ZBLAN photonic crystal fiber [114]. Also, mid-IR supercontinuum generation is demonstrated in a chalcogenide glass-based microstructured fiber [115, 116]. Although both ZBLAN and chalcogenide-based photonic crystal fibers are used to generate or guide light at mid-IR region, they are not suitable for the HOFGLAS system unless the core is hollow. To the extent of my knowledge, HC-PCFs based on the ZBLAN glasses are not reported. However, HC-PCF based on the chalcogenide glass is demonstrated in 2010 [117], and several HC-PCF structures are suggested based on numerical calculations to guide light in the mid/far-IR regions with lower losses [118, 119]. In 2011 a chalcogenide fiber with negative curvature hollow core is used to successfully deliver light at 10.6 μm from CO₂ laser with a fiber loss of 11 dB/m [120]. And the aforementioned fiber showed good transmittance in the spectral range 2-10 μm . Recently, a chalcogenide based negative curvature fiber with a lower loss of 2.1 dB/m at 10 μm is demonstrated by optimizing the fiber geometry [121]. More importantly, more work is done to develop HC-PCFs fibers based on the chalcogenide glasses and once these fibers are available one can potentially push the limits of HOFGLAS systems to longer wavelength region using molecules like CO₂, N₂O.

References

1. F. K. Tittel, D. Richter, and A. Fried, "Mid-Infrared Laser Applications in Spectroscopy," in *Solid-State Mid-Infrared Laser Sources*, I. T. Sorokina and K. L. Vodopyanov, eds. (Springer Berlin Heidelberg, Berlin, Heidelberg, 2003), pp. 458-529.
2. S. D. Jackson, "Towards high-power mid-infrared emission from a fibre laser," *Nature Photonics* **6**, 423 (2012).
3. F. Toor, S. Jackson, X. Shang, S. Arafin, and H. Yang, "Mid-infrared Lasers for Medical Applications: introduction to the feature issue," *Biomed. Opt. Express* **9**, 6255-6257 (2018).
4. H. Kaplan, *Practical Applications of Infrared Thermal Sensing and Imaging Equipment* (SPIE, 2007), Vol. TT75, p. 192.
5. K. Isensee, N. Kröger-Lui, and W. Petrich, "Biomedical applications of mid-infrared quantum cascade lasers – a review," *Analyst* **143**, 5888-5911 (2018).
6. J. Faist, F. Capasso, D. L. Sivco, C. Sirtori, A. L. Hutchinson, and A. Y. Cho, "Quantum Cascade Laser," *Science* **264**, 553-556 (1994).
7. Y. Yao, A. J. Hoffman, and C. F. Gmachl, "Mid-infrared quantum cascade lasers," *Nature Photonics* **6**, 432 (2012).
8. S. Bartalini, M. S. Vitiello, and P. De Natale, "Quantum cascade lasers: a versatile source for precise measurements in the mid/far-infrared range," *Measurement Science and Technology* **25**, 012001 (2013).
9. R. F. Curl, F. Capasso, C. Gmachl, A. A. Kosterev, B. McManus, R. Lewicki, M. Pusharsky, G. Wysocki, and F. K. Tittel, "Quantum cascade lasers in chemical physics," *Chemical Physics Letters* **487**, 1-18 (2010).
10. F. Maes, C. Stihler, L.-P. Pleau, V. Fortin, J. Limpert, M. Bernier, and R. Vallée, "3.42 μm lasing in heavily-erbium-doped fluoride fibers," *Opt. Express* **27**, 2170-2183 (2019).
11. S. Tokita, M. Murakami, S. Shimizu, M. Hashida, and S. Sakabe, "Liquid-cooled 24 W mid-infrared Er:ZBLAN fiber laser," *Opt. Lett.* **34**, 3062-3064 (2009).
12. F. Maes, V. Fortin, S. Poulain, M. Poulain, J.-Y. Carrée, M. Bernier, and R. Vallée, "Room-temperature fiber laser at 3.92 μm ," *Optica* **5**, 761-764 (2018).
13. O. Henderson-Sapir, S. D. Jackson, and D. J. Ottaway, "Versatile and widely tunable mid-infrared erbium doped ZBLAN fiber laser," *Opt. Lett.* **41**, 1676-1679 (2016).

14. S. D. Jackson, "High-power and highly efficient diode-cladding-pumped holmium-doped fluoride fiber laser operating at 2.94 μm ," *Opt. Lett.* **34**, 2327-2329 (2009).
15. T. Y. Chang and O. R. Wood, "Optically pumped atmospheric-pressure CO₂ laser," *Applied Physics Letters* **21**, 19-21 (1972).
16. J. E. McCord, H. C. Miller, G. Hager, A. I. Lampson, and P. G. Crowell, "Experimental investigation of an optically pumped mid-infrared carbon monoxide laser," *IEEE Journal of Quantum Electronics* **35**, 1602-1612 (1999).
17. J. E. McCord, A. A. Ionin, S. P. Phipps, P. G. Crowell, A. I. Lampson, J. K. McIver, A. J. W. Brown, and G. D. Hager, "Frequency-tunable optically pumped carbon monoxide laser," *IEEE Journal of Quantum Electronics* **36**, 1041-1052 (2000).
18. H. C. Miller, D. T. Radzykewycz, and G. Hager, "An optically pumped mid-infrared HBr laser," *IEEE Journal of Quantum Electronics* **30**, 2395-2400 (1994).
19. A. V. V. Nampoothiri, A. Ratanavis, N. Campbell, and W. Rudolph, "Molecular C₂H₂ and HCN lasers pumped by an optical parametric oscillator in the 1.5- μm band," *Opt. Express* **18**, 1946-1951 (2010).
20. A. M. Jones, A. V. V. Nampoothiri, A. Ratanavis, T. Fiedler, N. V. Wheeler, F. Couny, R. Kadel, F. Benabid, B. R. Washburn, K. L. Corwin, and W. Rudolph, "Mid-infrared gas filled photonic crystal fiber laser based on population inversion," *Opt. Express* **19**, 2309-2316 (2011).
21. A. V. V. Nampoothiri, A. M. Jones, C. Fourcade-Dutin, C. Mao, N. Dadashzadeh, B. Baumgart, Y. Y. Wang, M. Alharbi, T. Bradley, N. Campbell, F. Benabid, B. R. Washburn, K. L. Corwin, and W. Rudolph, "Hollow-core Optical Fiber Gas Lasers (HOFGLAS): a review [Invited]," *Opt. Mater. Express* **2**, 948-961 (2012).
22. A. M. Jones, C. Fourcade-Dutin, C. Mao, B. Baumgart, A. V. V. Nampoothiri, N. Campbell, Y. Wang, F. Benabid, W. Rudolph, B. R. Washburn, and K. L. Corwin, *Characterization of mid-infrared emissions from C₂H₂, CO, CO₂, and HCN-filled hollow fiber lasers*, SPIE LASE (SPIE, 2012), Vol. 8237.
23. Z. Wang, W. Belardi, F. Yu, W. J. Wadsworth, and J. C. Knight, "Efficient diode-pumped mid-infrared emission from acetylene-filled hollow-core fiber," *Opt. Express* **22**, 21872-21878 (2014).
24. A. V. V. Nampoothiri, B. Debord, M. Alharbi, F. G er ome, F. Benabid, and W. Rudolph, "CW hollow-core optically pumped I₂ fiber gas laser," *Opt. Lett.* **40**, 605-608 (2015).
25. A. V. Vasudevan Nampoothiri, F. Beygi Azar Aghbolagh, B. Debord, F. Gerome, F. Benabid, and W. Rudolph, "High photon conversion efficiency continuous wave lasing in an optically pumped I₂ hollow fiber gas laser in the visible region," *Appl. Opt.* **56**, 9592-9595 (2017).

26. M. R. Abu Hassan, F. Yu, W. J. Wadsworth, and J. C. Knight, "Cavity-based mid-IR fiber gas laser pumped by a diode laser," *Optica* **3**, 218-221 (2016).
27. N. Dadashzadeh, M. P. Thirugnanasambandam, H. W. K. Weerasinghe, B. Debord, M. Chafer, F. Gerome, F. Benabid, B. R. Washburn, and K. L. Corwin, "Near diffraction-limited performance of an OPA pumped acetylene-filled hollow-core fiber laser in the mid-IR," *Opt. Express* **25**, 13351-13358 (2017).
28. M. Xu, F. Yu, and J. Knight, "Mid-infrared 1 W hollow-core fiber gas laser source," *Opt. Lett.* **42**, 4055-4058 (2017).
29. Z. Zhou, N. Tang, Z. Li, W. Huang, Z. Wang, W. Wu, and W. Hua, "High-power tunable mid-infrared fiber gas laser source by acetylene-filled hollow-core fibers," *Opt. Express* **26**, 19144-19153 (2018).
30. Z. Zhou, N. Tang, Y. Cui, Z. Wang, and W. Hua, *All-fiber structure mid-infrared fiber gas laser source*, SPIE/COS Photonics Asia (SPIE, 2018), Vol. 10811.
31. F. B. A. Aghbolagh, V. Nampoothiri, B. Debord, F. Gerome, L. Vincetti, F. Benabid, and W. Rudolph, "Mid IR hollow core fiber gas laser emitting at 4.6 μm ," *Opt. Lett.* **44**, 383-386 (2019).
32. G. Herzberg and J. W. T. Spinks, "Molecular spectra and molecular structure," Prentice-Hall physics series **New York**(1939).
33. M. Herman, A. Campargue, M. I. E. Idrissi, and J. V. Auwera, "Vibrational Spectroscopic Database on Acetylene, $\tilde{X}^1\Sigma_g^+$ ($^{12}\text{C}_2\text{H}_2$, $^{12}\text{C}_2\text{D}_2$, and $^{13}\text{C}_2\text{H}_2$)," *Journal of Physical and Chemical Reference Data* **32**, 921-1361 (2003).
34. J. T. Verdeyen, *Laser Electronics* (Prentice Hall, 1995).
35. K. K. Lehmann and A. M. Smith, "Where does overtone intensity come from?," *The Journal of Chemical Physics* **93**, 6140-6147 (1990).
36. W. C. Swann and S. L. Gilbert, "Pressure-induced shift and broadening of 1510–1540-nm acetylene wavelength calibration lines," *J. Opt. Soc. Am. B* **17**, 1263-1270 (2000).
37. <http://www.spectralcalc.com/info/about.php>.
38. <http://www.hitran.org/>.
39. G. Agrawal, *Nonlinear Fiber Optics* (Elsevier Science, 2007).
40. R. F. Cregan, B. J. Mangan, J. C. Knight, T. A. Birks, P. S. J. Russell, P. J. Roberts, and D. C. Allan, "Single-Mode Photonic Band Gap Guidance of Light in Air," *Science* **285**, 1537 (1999).

41. F. Benabid, "Hollow-core photonic bandgap fibre: new light guidance for new science and technology," *Philosophical Transactions of the Royal Society A: Mathematical, Physical and Engineering Sciences* **364**, 3439-3462 (2006).
42. J. A. Buck, *Fundamentals of Optical Fibers* (Wiley, 2004).
43. P. J. Roberts, F. Couny, H. Sabert, B. J. Mangan, D. P. Williams, L. Farr, M. W. Mason, A. Tomlinson, T. A. Birks, J. C. Knight, and P. S. J. Russell, "Ultimate low loss of hollow-core photonic crystal fibres," *Opt. Express* **13**, 236-244 (2005).
44. N. V. Wheeler, A. M. Heidt, N. K. Baddela, E. N. Fokoua, J. R. Hayes, S. R. Sandoghchi, F. Poletti, M. N. Petrovich, and D. J. Richardson, "Low-loss and low-bend-sensitivity mid-infrared guidance in a hollow-core photonic-bandgap fiber," *Opt. Lett.* **39**, 295-298 (2014).
45. F. Couny, F. Benabid, P. J. Roberts, P. S. Light, and M. G. Raymer, "Generation and Photonic Guidance of Multi-Octave Optical-Frequency Combs," *Science* **318**, 1118 (2007).
46. G. J. Pearce, G. S. Wiederhecker, C. G. Poulton, S. Burger, and P. S. J. Russell, "Models for guidance in kagome-structured hollow-core photonic crystal fibres," *Opt. Express* **15**, 12680-12685 (2007).
47. C. Wei, R. Joseph Weiblen, C. R. Menyuk, and J. Hu, "Negative curvature fibers," *Adv. Opt. Photon.* **9**, 504-561 (2017).
48. F. Couny, F. Benabid, and P. S. Light, "Large-pitch kagome-structured hollow-core photonic crystal fiber," *Opt. Lett.* **31**, 3574-3576 (2006).
49. K. Knabe, S. Wu, J. Lim, K. A. Tillman, P. S. Light, F. Couny, N. Wheeler, R. Thapa, A. M. Jones, J. W. Nicholson, B. R. Washburn, F. Benabid, and K. L. Corwin, "10 kHz accuracy of an optical frequency reference based on $^{12}\text{C}_2\text{H}_2$ -filled large-core kagome photonic crystal fibers," *Opt. Express* **17**, 16017-16026 (2009).
50. C. Wang, N. V. Wheeler, C. Fourcade-Dutin, M. Grogan, T. D. Bradley, B. R. Washburn, F. Benabid, and K. L. Corwin, "Acetylene frequency references in gas-filled hollow optical fiber and photonic microcells," *Appl. Opt.* **52**, 5430-5439 (2013).
51. A. Lurie, F. N. Baynes, J. D. Anstie, P. S. Light, F. Benabid, T. M. Stace, and A. N. Luiten, "High-performance iodine fiber frequency standard," *Opt. Lett.* **36**, 4776-4778 (2011).
52. F. Benabid, J. C. Knight, G. Antonopoulos, and P. S. J. Russell, "Stimulated Raman Scattering in Hydrogen-Filled Hollow-Core Photonic Crystal Fiber," *Science* **298**, 399 (2002).
53. F. Benabid, G. Antonopoulos, J. C. Knight, and P. S. J. Russell, "Stokes Amplification Regimes in Quasi-cw Pumped Hydrogen-Filled Hollow-Core Photonic Crystal Fiber," *Physical Review Letters* **95**, 213903 (2005).

54. N. V. Wheeler, T. D. Bradley, J. R. Hayes, M. A. Gouveia, S. Liang, Y. Chen, S. R. Sandoghchi, S. M. Abokhamis Mousavi, F. Poletti, M. N. Petrovich, and D. J. Richardson, "Low-loss Kagome hollow-core fibers operating from the near- to the mid-IR," *Opt. Lett.* **42**, 2571-2574 (2017).
55. Y. Y. Wang, N. V. Wheeler, F. Couny, P. J. Roberts, and F. Benabid, "Low loss broadband transmission in hypocycloid-core Kagome hollow-core photonic crystal fiber," *Opt. Lett.* **36**, 669-671 (2011).
56. B. Debord, M. Alharbi, T. Bradley, C. Fourcade-Dutin, Y. Y. Wang, L. Vincetti, F. Gérôme, and F. Benabid, "Hypocycloid-shaped hollow-core photonic crystal fiber Part I: Arc curvature effect on confinement loss," *Opt. Express* **21**, 28597-28608 (2013).
57. B. Debord, A. Amsanpally, M. Alharbi, L. Vincetti, J.-M. Blondy, F. Gérôme, and F. Benabid, "Ultra-Large Core Size Hypocycloid-Shape Inhibited Coupling Kagome Fibers for High-Energy Laser Beam Handling," *Journal of Lightwave Technology* **33**, 3630-3634 (2015).
58. F. Yu, W. J. Wadsworth, and J. C. Knight, "Low loss silica hollow core fibers for 3–4 μm spectral region," *Opt. Express* **20**, 11153-11158 (2012).
59. F. Benabid, "Fiber Datasheet, Personal communication to K.L. Corwin," (2015).
60. A. M. Jones, "REALIZING A MID-INFRARED OPTICALLY PUMPED MOLECULAR GAS LASER INSIDE HOLLOW-CORE PHOTONIC CRYSTAL FIBER," Ph.D. thesis, Kansas State University, Manhattan, KS (2012).
61. https://www.rp-photonics.com/q_switching.html, (Accessed on 2/12/2019).
62. R. W. Boyd, *Nonlinear Optics* (Elsevier Science, 2013).
63. K. Knabe, "Using saturated absorption spectroscopy on acetylene-filled hollow-core fibers for absolute frequency measurements," Ph.D. thesis, Kansas State University, Manhattan, KS (2010).
64. H. W. K. Weerasinghe, N. Dadashzadeh, M. P. Thirugnanasambandam, B. Debord, M. Chafer, F. Gérôme, F. Benabid, K. L. Corwin, and B. R. Washburn, "Toward power scaling in an acetylene mid-infrared hollow-core optical fiber gas laser: effects of pressure, fiber length, and pump power," in *SPIE LASE*, (SPIE, 2018), 9.
65. N. Dadashzadeh, "Improved performance of an optically pumped mid-infrared acetylene-filled hollow-core fiber laser," Ph.D. thesis, Kansas State University, Manhattan, KS (2017).
66. T. Y. Fan, "Laser beam combining for high-power, high-radiance sources," *IEEE Journal of Selected Topics in Quantum Electronics* **11**, 567-577 (2005).

67. A. E. Siegman, "How to (Maybe) Measure Laser Beam Quality," in *DPSS (Diode Pumped Solid State) Lasers: Applications and Issues*, OSA Trends in Optics and Photonics (Optical Society of America, 1998), MQ1.
68. P. B. Chapple, *Beam waist and M^2 measurement using a finite slit* (SPIE, 1994), Vol. 33, pp. 2461-2466, 2466.
69. A. E. Siegman, *Lasers* (University Science Books, 1986).
70. D. Gloge, "Weakly Guiding Fibers," *Appl. Opt.* **10**, 2252-2258 (1971).
71. B. R. Washburn, "DISPERSION AND NONLINEARITIES ASSOCIATED WITH SUPERCONTINUUM GENERATION IN MICROSTRUCTURE FIBERS," Ph.D. thesis, Georgia Institute of Technology, Atlanta, GA (2002).
72. L. Novotny and C. Hafner, "Light propagation in a cylindrical waveguide with a complex, metallic, dielectric function," *Physical Review E* **50**, 4094-4106 (1994).
73. M. Miyagi and S. Kawakami, "Design theory of dielectric-coated circular metallic waveguides for infrared transmission," *Journal of Lightwave Technology* **2**, 116-126 (1984).
74. A. Hongo, K. Morosawa, T. Shiota, Y. Matsuura, and M. Miyagi, "Transmission characteristics of germanium thin-film-coated metallic hollow waveguides for high-powered CO₂ laser light," *IEEE Journal of Quantum Electronics* **26**, 1510-1515 (1990).
75. A. Hongo, K. i. Morosawa, T. Shiota, K. Suzuki, S. Iwasaki, and M. Miyagi, "Transmission of 1 kW-class CO₂ laser light through circular hollow waveguides for material processing," *Applied Physics Letters* **58**, 1582-1584 (1991).
76. E. A. J. Marcatili and R. A. Schmeltzer, "Hollow metallic and dielectric waveguides for long distance optical transmission and lasers," *The Bell System Technical Journal* **43**, 1783-1809 (1964).
77. A. Sampaolo, P. Patimisco, J. M. Kriesel, F. K. Tittel, G. Scamarcio, and V. Spagnolo, "Single mode operation with mid-IR hollow fibers in the range 5.1-10.5 μm ," *Opt. Express* **23**, 195-204 (2015).
78. F. Roullard and M. Bass, "Transverse mode control in high gain, millimeter bore, waveguide lasers," *IEEE Journal of Quantum Electronics* **13**, 813-819 (1977).
79. T. D. Bradley, N. V. Wheeler, G. T. Jasion, D. Gray, J. Hayes, M. A. Gouveia, S. R. Sandoghchi, Y. Chen, F. Poletti, D. Richardson, and M. Petrovich, "Modal content in hypocycloid Kagome hollow core photonic crystal fibers," *Opt. Express* **24**, 15798-15812 (2016).
80. J. A. Ruff and A. E. Siegman, "Measurement of beam quality degradation due to spherical aberration in a simple lens," *Opt Quant Electron* **26**, 629-632 (1994).

81. "Lasers and laser-related equipment-test methods for laser beam widths, divergence angles and beam propagation ratios," ISO Standard 11146 (2005).
82. A. E. Siegman, *Defining, measuring, and optimizing laser beam quality*, OE/LASE'93: Optics, Electro-Optics, and Laser Applications in Science and Engineering (SPIE, 1993), Vol. 1868.
83. W. E. Lamb, "Theory of an Optical Maser," *Physical Review* **134**, A1429-A1450 (1964).
84. A. Szöke and A. Javan, "Isotope Shift and Saturation Behavior of the **1.15- μ** Transition of Ne," *Physical Review Letters* **10**, 521-524 (1963).
85. K. An, R. R. Dasari, and M. S. Feld, "One-step absolute frequency stabilization of a Ti:sapphire laser using frequency modulation Lamb-dip spectroscopy," *Applied Physics Letters* **66**, 2162-2164 (1995).
86. J. Hall, "The laser absolute wavelength standard problem," *IEEE Journal of Quantum Electronics* **4**, 638-641 (1968).
87. E. D. van Ooijen, G. Katgert, and P. van der Straten, "Laser frequency stabilization using Doppler-free bichromatic spectroscopy," *Applied Physics B* **79**, 57-59 (2004).
88. D. C. Heinecke, A. Bartels, T. M. Fortier, D. A. Braje, L. Hollberg, and S. A. Diddams, "Optical frequency stabilization of a 10 GHz Ti:sapphire frequency comb by saturated absorption spectroscopy in **⁸⁷rubidium**," *Physical Review A* **80**, 053806 (2009).
89. J. Henningsen, J. Hald, and J. C. Petersen, "Saturated absorption in acetylene and hydrogen cyanide in hollow-core photonic bandgap fibers," *Opt. Express* **13**, 10475-10482 (2005).
90. W. Demtröder, *Laser Spectroscopy Basic Concepts and Instrumentation* (Springer, 2003).
91. R. A. Lane and T. J. Madden, "Numerical investigation of pulsed gas amplifiers operating in hollow-core optical fibers," *Opt. Express* **26**, 15693-15704 (2018).
92. M. Newville, Stensitzki, T., Allen, D. B., & Ingargiola, A, "LMFIT: Non-Linear Least-Square Minimization and Curve-Fitting for Python," <https://lmfit.github.io/lmfit-py/> (2014 September 21).
93. <http://doi.org/10.15125/BATH-00392>.
94. R. L. Sutherland, *Handbook of Nonlinear Optics* (Taylor & Francis, 2003).
95. P. A. Franken, A. E. Hill, C. W. Peters, and G. Weinreich, "Generation of Optical Harmonics," *Physical Review Letters* **7**, 118-119 (1961).
96. W. J. Tropf, *Temperature-dependent refractive index models for BaF₂, CaF₂, MgF₂, SrF₂, LiF, NaF, KCl, ZnS, and ZnSe* (SPIE, 1995), Vol. 34, p. 5.

97. D. H. Jundt, "Temperature-dependent Sellmeier equation for the index of refraction, n_e , in congruent lithium niobate," *Opt. Lett.* **22**, 1553-1555 (1997).
98. K. L. Vodopyanov, O. Levi, P. S. Kuo, T. J. Pinguet, J. S. Harris, M. M. Fejer, B. Gerard, L. Becouarn, and E. Lallier, "Optical parametric oscillation in quasi-phase-matched GaAs," *Opt. Lett.* **29**, 1912-1914 (2004).
99. H. Jhans, J. M. Honig, and C. N. R. Rao, "Optical properties of reduced LiNbO_3 ," *Journal of Physics C: Solid State Physics* **19**, 3649-3658 (1986).
100. J. A. Armstrong, N. Bloembergen, J. Ducuing, and P. S. Pershan, "Interactions between Light Waves in a Nonlinear Dielectric," *Physical Review* **127**, 1918-1939 (1962).
101. K. Finsterbusch, R. Urschel, and H. Zacharias, "Tunable, high-power, narrow-band picosecond IR radiation by optical parametric amplification in KTP," *Applied Physics B* **74**, 319-322 (2002).
102. J. D. Bierlein and C. B. Arweiler, "Electro-optic and dielectric properties of KTiOPO_4 ," *Applied Physics Letters* **49**, 917-919 (1986).
103. J. D. Bierlein and H. Vanherzeele, "Potassium titanyl phosphate: properties and new applications," *J. Opt. Soc. Am. B* **6**, 622-633 (1989).
104. O. Isaienko and E. Borguet, "Generation of ultra-broadband pulses in the near-IR by non-collinear optical parametric amplification in potassium titanyl phosphate," *Opt. Express* **16**, 3949-3954 (2008).
105. A. V. Smith, W. J. Alford, T. D. Raymond, and M. S. Bowers, "Comparison of a numerical model with measured performance of a seeded, nanosecond KTP optical parametric oscillator," *J. Opt. Soc. Am. B* **12**, 2253-2267 (1995).
106. K. Kato, "Parametric oscillation at $3.2 \mu\text{m}$ in KTP pumped at $1.064 \mu\text{m}$," *IEEE Journal of Quantum Electronics* **27**, 1137-1140 (1991).
107. "<http://www.as-photonics.com/snlo>."
108. "<http://eksmaoptics.com/out/media/Crystals%202013%20EUR.pdf>."
109. F. Zhu, A. Bicer, R. Askar, J. Bounds, A. A. Kolomenskii, V. Kelessides, M. Amani, and H. A. Schuessler, "Mid-infrared dual frequency comb spectroscopy based on fiber lasers for the detection of methane in ambient air," *Laser Physics Letters* **12**, 095701 (2015).
110. Z. Zhang, T. Gardiner, and D. T. Reid, "Mid-infrared dual-comb spectroscopy with an optical parametric oscillator," *Opt. Lett.* **38**, 3148-3150 (2013).
111. M. Yan, P.-L. Luo, K. Iwakuni, G. Millot, T. W. Hänsch, and N. Picqué, "Mid-infrared dual-comb spectroscopy with electro-optic modulators," *Light: Science & Applications* **6**, e17076 (2017).

112. M. Yu, Y. Okawachi, A. G. Griffith, N. Picqué, M. Lipson, and A. L. Gaeta, "Silicon-chip-based mid-infrared dual-comb spectroscopy," *Nature Communications* **9**, 1869 (2018).
113. A. Weiner, *Ultrafast Optics* (Wiley, 2011).
114. X. Jiang, N. Y. Joly, M. A. Finger, F. Babic, G. K. L. Wong, J. C. Travers, and P. S. J. Russell, "Deep-ultraviolet to mid-infrared supercontinuum generated in solid-core ZBLAN photonic crystal fibre," *Nature Photonics* **9**, 133 (2015).
115. W. Yuan, "2–10 μm mid-infrared supercontinuum generation in As_2Se_3 photonic crystal fiber," *Laser Physics Letters* **10**, 095107 (2013).
116. T. S. Saini, A. Kumar, and R. K. Sinha, "Broadband Mid-Infrared Supercontinuum Spectra Spanning 2–15 μm Using As_2Se_3 Chalcogenide Glass Triangular-Core Graded-Index Photonic Crystal Fiber," *Journal of Lightwave Technology* **33**, 3914-3920 (2015).
117. F. Désévéday, G. Renversez, J. Troles, P. Houizot, L. Brilland, I. Vasilief, Q. Coulombier, N. Traynor, F. Smektala, and J.-L. Adam, "Chalcogenide glass hollow core photonic crystal fibers," *Optical Materials* **32**, 1532-1539 (2010).
118. C. Wei, C. R. Menyuk, and J. Hu, "Geometry of Chalcogenide Negative Curvature Fibers for CO_2 Laser Transmission," *Fibers* **6**, 74 (2018).
119. J. M. Pottage, D. M. Bird, T. D. Hedley, T. A. Birks, J. C. Knight, P. S. J. Russell, and P. J. Roberts, "Robust photonic band gaps for hollow core guidance in PCF made from high index glass," *Opt. Express* **11**, 2854-2861 (2003).
120. A. F. Kosolapov, A. D. Pryamikov, A. S. Biriukov, V. S. Shiryaev, M. S. Astapovich, G. E. Snopatin, V. G. Plotnichenko, M. F. Churbanov, and E. M. Dianov, "Demonstration of CO_2 -laser power delivery through chalcogenide-glass fiber with negative-curvature hollow core," *Opt. Express* **19**, 25723-25728 (2011).
121. C. R. Menyuk, C. Wei, R. J. Weiblen, J. Hu, R. R. Gattass, L. B. Shaw, and J. S. Sanghera, *Chalcogenide negative curvature fibers*, SPIE Security + Defence (SPIE, 2017), Vol. 10435.

Appendix A - Abbreviations

AOM	Acousto-optic-modulator
AR	Anti-reflection
CPM	Critical phase matching
CW	Continuous wave
DFG	Difference frequency generation
EDFA	Erbium doped fiber amplifier
FWHM	Full width half maximum
HC-PCF	Hollow-core photonic crystal fiber
HOFGLAS	Hollow-core optically pumped fiber gas laser
IR	Infrared
KTP	Potassium titanyl phosphate
LP	Linearly polarized
MFP	Mean free path
NCPM	Noncritical phase matching
OPA	Optical parametric amplifier
OPO	Optical parametric oscillator
PBGF	Photonic band gap fiber
PD	Photo diode
PM	Polarization maintain
PPLN	Periodically poled lithium niobate
QCL	Quantum cascade laser
QPM	Quasi-phase matching

SAS	Saturated absorption spectroscopy
SFG	Sum frequency generation
SHG	Second harmonic generation
SMF	Single mode fiber
TE	Transvers electric
TEM	Transverse electromagnetic
TIR	Total internal reflection
TM	Transverse magnetic
UV	Ultraviolet

Appendix B - Python codes

B.1 Python code to check the validity of saturation power of 23 mW for acetylene

The following python code is originally written by Dr. Brian Washburn. I edited it accordingly to test the validity of saturation power of acetylene (23 mW) which was reported in Ref. [89].

Note that this Python code will work only in Python 2.0.

```
# -*- coding: utf-8 -*-
"""
acetylene_laser_absorption.py
12/12/2018

Created on Mon Feb 08 08:52:53 2016
Brian Washburn

Edited by Kushan Weerasinghe

Solves first order differential equation for saturated loss and linear loss
 $dP/dz = - (ag/\sqrt{1+P/Ps}) P - a_l P$ 

1st RHS term: saturated loss due to gas
2nd RHS term: loss due to fiber absorption

The program then computes the total absorbed power, and the amount of power
absorbed by the gas and fiber separately

And this program is written to check the validity of Saturation power given in
Ref. [6].

References
[1] Swann et al., JOSAB vol 17, (2000)
[2] NIST special publication 260-133, 2001 edition
[3] Jun Ye Ph.D. thesis
[4] Corwin's brain
[5] Thapa OL vol 31, 16 (2006)
[6] Henningsen et al, Opt. Express Vol. 13, Issue 26, pp. 10475-10482 (2005)
[7] HITRAN database

All units in meters, kilograms, seconds, except pressure in units of torr
"""
import numpy as np
from matplotlib import pyplot as plt
import time, os
from scipy.integrate import ode
from lmfit.models import VoigtModel
```



```

start=time.time() # for cpu timing
plt.close('all')
os.system('cls')
print 'Running%s ...'% os.path.basename(__file__),
print ' '

# universal constants
kb = 1.3806503*1e-23 # J/K, Boltzmann constant
amu=1.66054e-27 # atomic mass unit in kg
c = 2.99792458*1e8 # m/s, speed of light

#-----
# Define functions

# Lorentian width as a function of pressure (in torr)
# Note: need to be careful here. The 11.4 MHz/torr is slope and not a
# direct conversion from pressure to width. Need to verify the dependence
# at low pressures (<50 torr). The lorentzian widths in Table 4 are FWHM
# Return value of gamma (lorentzian fwhm/2)
# Lorentian gamma as a function of pressure (in torr)
def gL(p):
    a=12.46 #HITRAN DATA base
    b=0 # 58.529 MHz comes from intercept of linear fit to data from Ref[1]
    return (a*p+b)/2 #

# Gaussian width sigma as a function of temperature (in Kelvin)
def sigmaG(T,m,f0):
    # gaussian fwhm is equal to 2*Sqrt(2*ln(2))*sigma = 2.355 Sigma
    return f0*np.sqrt(kb*T/(m*c**2)) # error here fixed on 4/2017

def avHITRAN(p,T,f,f0):
    # determine frequency dependent absorption based on a Voigt profile
    # Functional form: absorption(v)=S*(p/(kb*T))*Voigt(v) (see Ref. [6])
    # use HITRAN [7] to determine line strength S
    c = 2.99792458*1e8 # m/s, speed of light

    # HITRAN database spectral line strength
    S = 1.024e-20 # in units of cm-1/(molecules 1/cm2) taken from HITRAN database
    S = S/100**2 # convert to cm-1/(molecules 1/m2)
    S = S*(c*100) # convert to Hz/(molecules 1/m2) using 1 cm-1 is equal to 29.97 GHz

    m=26*amu # molecular mass
    mod = VoigtModel() # create model class

    # create absorption as a function of pressure and temperature
    sig=sigmaG(T,m,f0) # gaussian width at given temperature
    gam=gL(p) # lorentzian width at given pressure
    y=mod.eval(x=f, amplitude=1, center=f0, sigma=sig, gamma=gam) # evaluate model
    return S*(p*133.32)/(kb*T)*y

def torr2pascal(ptorr) :
    return ptorr*133.32

#-----

```

```

# system parameters
l0=1530.37095e-9          # center wavelength fpr P9 in m
f0=c/l0                  # center frequency in Hz
m=26*amu                 # mass in kg of acetylene molecule
T=296.0                  # temperature in Kelvin
p=0.075                  # pressure in torr (10 Pa)
r=10e-6/2                # fiber radius

al_dB=0.2                # fiber absorption coefficient (0.2 dB/m)
L=6.35                   # fiber length (6.35 m)
al=-(1/L)*np.log(10**(-al_dB*L/10)) # fiber loss in 1/m

# define frequency array for absorption feature
numf=10000               # number of frequency points
ran=1.0e11               # frequency range about center frequency
df=ran/numf
f=(np.linspace(1,numf,numf)-numf/2-1)*df+f0

sig=sigmaG(T,m,f0)      # gaussian width at given temperature
gam=gl(p)               # lorentzian width at given pressure

ab=avHITRAN(p,T,f,f0)  # Voigt absorption as a function of frequency
ag=ab[(f==f0)][0]      # peak absorption at line center
#ag=0.1642
# set up input pulse properties
# 7.55 uJ Gaussian pulse, 1 ns duration at 30 Hz (toptica)
En = 7.55e-6           # 7.55 uJ pulse energy
Dt = 1e-9              # 1 ns pulse duration
F = 30.0               # rep rate of 30 Hz
#P0 = En2PG(En,Dt,1/F) # peak power of 7092 W
#P0=2.5e-3 # cw power
#P0=P0 * (100.0/84.0)
#P0=P0*np.exp(al*L)

P0=np.linspace(0.1e-3,30.0e-3,50)
P0=(P0)*np.exp(al*L) # input power = output power * exp (alpha * L)
#P0=np.array(P0)*1.16

# saturation power

Ps=23.0e-3             # saturation power from ref 6

#-----
# set up DE to solve
def de(z,Y):
    return -1*ag*Y[0]/np.sqrt(1+Y[0]/Ps) - al*Y[0]
#-----

# set space array
numz=1000
dz=L/numz
z=(np.linspace(0,L,numz))

absor=[]

for P00 in P0[0:]:

```

```

# set initial values
y0= []
Y00=P00
y0.append(Y00) # set first value

# setup ode integrator
backend='vode' # set type of ode solver
rsol = ode(de) # define ode element
rsol.set_integrator(backend) # set type of ode solver
rsol.set_initial_value(Y00, z[0]) # set initial values

for zz in z[1:]:
    sol=rsol.integrate(zz) # solution from ode solver
    y0.append(sol[0])
    if not rsol.successful():
        print "Warning: integration not sucessfull!"

# convert result to np type arrays for plotting
Pz=np.array(y0)

# compute transmitted and absorbed power
Pt=Pz[-1] # transmitted power at fiber end
Pabs=P0-Pt # total power absorbed
Pabsl=np.trapz(al*Pz,dx=dz) # power absorbed by fiber loss
Pabsg=np.trapz(ag*Pz/np.sqrt(1+Pz/Ps),dx=dz) # power absorbed by the gas

Pabsg_nd=Pabs+Pz[0]*(np.exp(-al*L)-1) # power absorbed by gas using Neda's method
Pabsg_kc=Pz[0]-Pz[1]*np.exp(al*L) # power absorbed by gas using Kristan's method

runtime=(time.time() - start)

absorbance= np.log(((P00))/(Pt))-al*L # calculating absorbance for gas
absor.append(absorbance)
P_in.append(P0[b])
b=b+1
#
# plotting results

plt.plot(P0,absor,'ko')
plt.ylim(0,1.2)
x=[0e-3,5e-3,10e-3,15e-3,20e-3,25e-3,30e-3]
x_xticks=['0','5','10','15','20','25','30']
x_minor=np.array(x)/2
plt.xticks(x,x_xticks,fontsize=16)
plt.yticks(fontsize=16)
plt.minorticks_on()
plt.grid()
plt.xlim(0,32.5e-3)
plt.xlabel('Power(mW)', fontsize= 16,fontweight= 'bold')
plt.ylabel('Optical depth',fontsize=16,fontweight= 'bold')

```

B.2 Python code to calculate absorbed near-IR pump power by acetylene gas in CW HOFGLAS system

Note that this will work only with Python 2.0

```
# -*- coding: utf-8 -*-
"""
acetylene_laser_absorption.py
12/13/208

Created on Mon Feb 08 08:52:53 2016
Brian Washburn
Edited by Kushan Weerasinghe
Solves first order differential equation for saturated loss and linear loss


$$dP/dz = - (ag/\sqrt{1+P/Ps}) P - a_l P$$


1st RHS term: saturated loss due to gas
2nd RHS term: loss due to fiber absorption

The program then computes the total absorbed power, and the amount of power
absorbed by the gas and fiber separately

References
[1] Swann et al., JOSAB vol 17, (2000)
[2] NIST special publication 260-133, 2001 edition
[3] Jun Ye Ph.D. thesis
[4] Corwin's brain
[5] Thapa OL vol 31, 16 (2006)
[6] Henningsen et al, Opt. Express Vol. 13, Issue 26, pp. 10475-10482 (2005)
[7] HITRAN database
[8]

All units in meters, kilograms, seconds, except pressure in units of torr
"""
import numpy as np
from matplotlib import pyplot as plt
import time, os
from scipy.integrate import ode
from lmfit.models import VoigtModel

plt.close()
# universal constants
kb = 1.3806503*1e-23 # J/K, Boltzmann constant
amu=1.66054e-27 # atomic mass unit in kg
c = 2.99792458*1e8 # m/s, speed of light
```

```

#-----
# Define functions

# Lorentian width as a function of pressure (in torr)
# Note: need to be careful here. The 11.4 MHz/torr is slope and not a
# direct conversion from pressure to width. Need to verify the dependence
# at low pressures (<50 torr). The lorentzian widths in Table 4 are FWHM
# Return value of gamma (lorentzian fwhm/2)
# Lorentian gamma as a function of pressure (in torr)
def gL(p):
    a=12.46 #HITRAN DATA base for P9
    b=0 # 58.529 MHz comes from intercept of linear fit to data from Ref[1]
    return (a*p+b)/2 #

# Gaussian width sigma as a function of temperature (in Kelvin)
def sigmaG(T,m,f0):
    # gaussian fwhm is equal to 2*Sqrt(2*ln(2))*sigma = 2.355 Sigma
    return f0*np.sqrt(kb*T/(m*c**2)) # error here fixed on 4/2017

def avHITRAN(p,T,f,f0):
    # determine frequency dependent absorption based on a Voigt profile
    # Functional form: absorption(v)=S*(p/(kb*T))*Voigt(v) (see Ref. [6])
    # use HITRAN [7] to determine line strength S
    c = 2.99792458*1e8 # m/s, speed of light

    # HITRAN database spectral line strength
    S = 1.211e-20 # in units of cm-1/(molecules 1/cm2) taken from HITRAN database
    S = S/100**2 # convert to cm-1/(molecules 1/m2)
    #S=S*29.97e9
    S = S*(c*100) # convert to Hz/(molecules 1/m2) using 1 cm-1 is equal to 29.97 GHz

    m=26*amu # molecular mass
    mod = VoigtModel() # create model class

    # create absorption as a function of pressure and temperature
    sig=sigmaG(T,m,f0) # gaussian width at given temperature
    gam=gL(p) # lorentzian width at given pressure
    y=mod.eval(x=f, amplitude=1, center=f0, sigma=sig, gamma=gam) # evaluate model
    return S*(p*133.32)/(kb*T)*y

def torr2pascal(ptorr) :
    return ptorr*133.32

def En2PG(En,Dt,T):
    # compute the peak and average power from pulse energy for gaussian pulse of period T a
nd fwhm Dt
    eta = 1.06447 # gaussian factor
    Pp = En/(eta*Dt)
    return Pp

def Pave2Ppg(Pave,Dt,T) :
    eta = 1.06447 # gaussian factor
    return Pave*T/(eta*Dt)

#-----

# system parameters
l0=1530.37095e-9 # center wavelength fpr P9 in m
f0=c/l0 # center frequency in Hz

```

```

m=26*amu          # mass in kg of acetylene molecule
T=296.0           # temperature in Kelvin
p=0.4350358      # pressure in torr (0.6 mbar)
r=75e-6/2        # fiber mode field radius

al_dB=37.0/1000.0 # fiber absorption coefficient (0.2 dB/m)
L=15.0           # fiber length (15 m)
al=-(1/L)*np.log(10**(-al_dB*L/10)) # fiber loss in 1/m

# define frequency array for absorption feature
numf=10000       # number of frequency points
ran=1.0e11       # frequency range about center frequency
df=ran/numf
f=(np.linspace(1,numf,numf)-numf/2-1)*df+f0

sig=sigmaG(T,m,f0) # gaussian width at given temperature
gam=gl(p)         # lorentzian width at given pressure

ab=avHITRAN(p,T,f,f0) # Voigt absorption as a function of frequency
ag=ab[(f==f0)][0]    # peak absorption at line center
P0 = [0.1233232, 0.1560944, 0.1957648, 0.2466464, 0.310464, 0.3906672, 0.4924304,
0.6217904, 0.8054816,\
0.9805488, 1.2349568, 1.556632, 1.9541984, 2.4543904, 2.7519184, 3.0865296, 3.4
616736, 3.8920112,\
4.372368, 4.932928, 5.596976, 6.407632, 7.442512, 8.382528] # incident power

P0=np.array(P0)*0.50 # coupled power

Ps=23.0e-3 # from ref4
#Ps=Ps*(10.0/75.0)**0.5
#Ps=Ps*np.log((15.0/2.0)**.15)
#-----
# set up DE to solve
def de(z,Y):
    return -1*ag*Y[0]/np.sqrt(1+Y[0]/Ps) - al*Y[0]
#-----

# set space array
numz=1000
dz=L/numz
z=(np.linspace(0,L,numz))

absorb_by_gas=[]
for P00 in P0[0:]:
    # set initial values
    y0= []
    Y00=P00
    y0.append(Y00) # set first value

# setup ode integrator
    backend='vode' # set type of ode solver
    rsol = ode(de) # define ode element
    rsol.set_integrator(backend) # set type of ode solver
    rsol.set_initial_value(Y00, z[0]) # set initial values

    for zz in z[1:]:
        sol=rsol.integrate(zz) # solution from ode solver
        y0.append(sol[0])
        if not rsol.successful():
            print "Warning: integration not sucessfull!"

```

```

# convert result to np type arrays for plotting
Pz=np.array(y0)

# compute transmitted and absorbed power
Pt=Pz[-1] # transmitted power at fiber end
Pabs=P0-Pt # total power absorbed
Pabsl=np.trapz(al*Pz,dx=dz) # power absorbed by fiber loss
Pabsg=np.trapz(ag*Pz/np.sqrt(1+Pz/Ps),dx=dz) # power absorbed by the gas

Pabsg_nd=Pabs+Pz[0]*(np.exp(-al*L)-1) # power absorbed by gas using Neda's method
Pabsg_kc=Pz[0]-Pz[-1]*np.exp(al*L) # power absorbed by gas using Kristan's method

absorb_by_gas.append(Pabsg) # absorb energy by gas

# experimental values
Pabsg_exp=[0.082607002, 0.101909217, 0.121896691, 0.147958486, 0.179506745,\
0.218402442, 0.266574514, 0.32632209, 0.417150331, 0.48852039, 0.602764286,\
0.74225537, 0.912629811, 1.125886545, 1.250796755, 1.389199504, 1.544405213,\
1.72210611, 1.917871182, 2.142005634, 2.404509626, 2.722916475, 3.137116569,\
3.472631115]

plt.figure(100)
plt.plot(P0,Pabsg_exp,'bo',label='Experiment')
plt.plot(P0,absorb_by_gas,'r*',label='Numerical')
plt.legend(loc='best',borderaxespad=1, frameon=True,fontsize=12)
plt.xticks(fontsize=16)
plt.yticks(fontsize=16)
plt.minorticks_on()
plt.grid()
plt.xlabel('Coupled power (W)',fontsize= 16,fontweight= 'bold')
plt.ylabel('Absorbed power only by gas (W)',fontsize= 16,fontweight= 'bold')

```

B.3 Python code to calculate absorbed near-IR energy by acetylene gas in HOFGLAS system

Note: Use only Python 2.0 for this code.

```
# -*- coding: utf-8 -*-
"""
acetylene_HOFGLAS(pulsed)_absorption.py
12/19/2018

Created on Mon Feb 08 08:52:53 2016
Brian Washburn

Solves first order differential equation for saturated loss and linear loss


$$dP/dz = - (ag/\sqrt{1+P/Ps}) P - a_l P$$


1st RHS term: saturated loss due to gas
2nd RHS term: loss due to fiber absorption

The program then computes the total absorbed power, and the amount of power
absorbed by the gas and fiber separately

References
[1] Swann et al., JOSAB vol 17, (2000)
[2] NIST special publication 260-133, 2001 edition
[3] Jun Ye Ph.D. thesis
[4] Corwin's brain
[5] Thapa OL vol 31, 16 (2006)
[6] Henningsen et al, Opt. Express Vol. 13, Issue 26, pp. 10475-10482 (2005)
[7] HITRAN database

This program is used to calculate the absorbed near-IR pump energy only by gas
for pulsed HOFGLAS system

All units in meters, kilograms, seconds, except pressure in units of torr
"""
import numpy as np
from matplotlib import pyplot as plt
import time, os
from scipy.integrate import ode
from lmfit.models import VoigtModel

start=time.time() # for cpu timing
plt.close('all')
os.system('cls')
print 'Running%s ...'% os.path.basename(__file__),
print ' '

# universal constants
kb = 1.3806503*1e-23 # J/K, Boltzmann constant
```



```

amu=1.66054e-27      # atomic mass unit in kg
c = 2.99792458*1e8   # m/s, speed of light

#-----
# Define functions

# Lorentian width as a function of pressure (in torr)
# Note: need to be careful here. The 11.4 MHz/torr is slope and not a
# direct conversion from pressure to width. Need to verify the dependence
# at low pressures (<50 torr). The lorentzian widths in Table 4 are FWHM
# Return value of gamma (lorentzian fwhm/2)
# Lorentian gamma as a function of pressure (in torr)
def gl(p):
    a=11.479e6 # 11.4 MHz per torr, from Ref [1], Table 4
    b=0 # 58.529 MHz comes from intercept of linear fit to data from Ref[1]
    return (a*p+b)/2 #

# Gaussian width sigma as a function of temperature (in Kelvin)
def sigmaG(T,m,f0):
    # gaussian fwhm is equal to 2*Sqrt(2*ln(2))*sigma = 2.355 Sigma
    return f0*np.sqrt(kb*T/(m*c**2)) # error here fixed on 4/2017

# Voigt absorption profile of acetylene

def avHITRAN(p,T,f,f0):
    # determine frequency dependent absorption based on a Voigt profile
    # Functional form: absorption(v)=S*(p/(kb*T))*Voigt(v) (see Ref. [6])
    # use HITRAN [7] to determine line strength S
    c = 2.99792458*1e8 # m/s, speed of light

    # HITRAN database spectral line strength
    S = 1.035e-20 # in units of cm-1/(molecules 1/cm2) taken from HITRAN database
    S = S/100**2 # convert to cm-1/(molecules 1/m2)
    S = S*(c*100) # convert to Hz/(molecules 1/m2) using 1 cm-1 is equal to 29.97 GHz

    m=26*amu # molecular mass
    mod = VoigtModel() # create model class

    # create absorption as a function of pressure and temperature
    sig=sigmaG(T,m,f0) # gaussian width at given temperature
    gam=gl(p) # lorentzian width at given pressure
    y=mod.eval(x=f, amplitude=1, center=f0, sigma=sig, gamma=gam) # evaluate model
    return S*(p*133.32)/(kb*T)*y

def torr2pascal(ptorr) :
    return ptorr*133.32

def En2PG(En,Dt,T):
    # compute the peak and average power from pulse energy for gaussian pulse of period T and fwhm Dt
    eta = 1.06447 # gaussian factor
    Pp = En/(eta*Dt)
    return Pp

def Pave2Ppg(Pave,Dt,T) :
    eta = 1.06447 # gaussian factor
    return Pave*T/(eta*Dt)

```

```

#-----
# system parameters
l0=1532.83042e-9      # center wavelength in m
f0=c/l0              # center frequency in Hz
m=26*amu             # mass in kg of acetylene molecule
T=298.0              # temperature in Kelvin
p=14.0               # pressure in torr
r=42e-6/2            # fiber mode field radius

a1_dB=0.08           # fiber absorption coefficient (0.08 dB/m)
L=10.9               # fiber length (10.9 m)
a1=-(1/L)*np.log(10**(-a1_dB*L/10)) # fiber loss in 1/m

# define frequency array for absorption feature
numf=10000           # number of frequency points
ran=1.0e11           # frequency range about center frequency
df=ran/numf
f=(np.linspace(1,numf,numf)-numf/2-1)*df+f0

sig=sigmaG(T,m,f0)   # gaussian width at given temperature
gam=gl(p)            # lorentzian width at given pressure

ab=avHITRAN(p,T,f,f0) # Voigt absorption as a function of frequency
ag=ab[(f==f0)][0]    # peak absorption at line center
#ag=0.1642

# set up input pulse properties
# 7.55 uJ Gaussian pulse, 1 ns duration at 30 Hz (toptica)
En = 7.76e-6        # 7.55 uJ pulse energy
Dt = 1e-9           # 1 ns pulse duration
F = 30.0            # rep rate of 30 Hz
P0 = En2PG(En,Dt,1/F) # peak power of 7092 W
#P0=7.51e-6

# saturation power
Ps= 23e-3           # saturation power average power

#Ps=24.48e-12
Ps=Ps*25           # scale by factor 5.2

#-----
# set up DE to solve
def de(z,Y):
    return -1*ag*Y[0]/np.sqrt(1+Y[0]/Ps) - a1*Y[0]
#-----

# set space array
numz=1000
dz=L/numz
z=(np.linspace(0,L,numz))

# set initial values
y0= []
Y00=P0
y0.append(Y00) # set first value

# setup ode integrator
backend='vode'      # set type of ode solver
rsol = ode(de)      # define ode element

```

```

rsol.set_integrator(backend)          # set type of ode solver
rsol.set_initial_value(Y00, z[0])    # set initial values

for zz in z[1:]:
    sol=rsol.integrate(zz)           # solution from ode solver
    y0.append(sol[0])
    if not rsol.successful():
        print "Warning: integration not sucessfull!"

# convert result to np type arrays for plotting
Pz=np.array(y0)

# compute transmitted and absorbed power
Pt=Pz[-1]                            # transmitted power at fiber end
Pabs=P0-Pt                            # total power absorbed
Pabsl=np.trapz(al*Pz,dx=dz)           # power absorbed by fiber loss
Pabsg=np.trapz(ag*Pz/np.sqrt(1+Pz/Ps),dx=dz) # power absorbed by the gas

Pabsg_nd=Pabs+Pz[0]*(np.exp(-al*L)-1) # power absorbed by gas using Neda's method
Pabsg_kc=Pz[0]-Pz[-1]*np.exp(al*L)   # power absorbed by gas using Kristan's method

runtime=(time.time() - start)
print '_____ '
print '%s Runtime of%.2f seconds'%(os.path.basename(__file__), runtime)
print '# space steps:%d'% numz
print ' '
print 'Pressure =%.3f torr'% p
print 'Fiber mode field radius =%.3f um'% (r*1e6)
print ' '
print 'Gaussian sigma =%.3f MHz'% (sig/1e6)
print 'Lorentzian gamma =%.3f MHz'% (gam/1e6)
#print 'Transit time broadening =%.3f MHz'% (gtt/1e6)
print ' '
print 'Saturation power =%.3e W'% Ps
print 'Gas absorption =%.3f 1/m'% ag
print 'Fiber absorption =%.3f 1/m'% al
print 'Fiber length =%.3f m'% L
print ' '
print 'Input power =%.3f W'% P0
print 'Transmitted power =%.3e W or%.3f percent of total input power'% (Pt, Pt/P0*100)
print 'Absorbed power =%.3e W or%.3f percent of total input power'% (Pabs, Pabs/P0*100)

print ' '
print 'Power absorbed by fiber =%.3e W or%.3f percent of total absorbed power'% (Pabsl, Pabsl/Pabs*100)
print 'Power absorbed by gas =%.3e W or%.3f percent of total absorbed power or%.3f percent of total power'% (Pabsg, Pabsg/Pabs*100, Pabsg/P0*100)
print ' '
print 'Power absorbed by gas (Neda) =%.3f W'% Pabsg_nd
print 'Power absorbed by gas (Kristan) =%.3f W'% Pabsg_kc
print 'Average between two methods =%.3f W'% ((Pabsg_nd+Pabsg_kc)/2)
print ' '
print 'Total absorbed energy =%.5g uJ at%.3g torr'%(En*Pabsg/P0*1e6, p)

print '_____ '

plt.figure(1)
plt.plot(z,Pz,'r',label='P(z)')
plt.xlabel('fiber position (m)')
plt.ylabel('Power (W)')
plt.grid(True)

```

```

plt.legend()
#
#plt.legend()
# plot the calculated absorbed energy vs pressure
ps = np.array([1.2,3.6,4.8,7.5,9.8,14.0])
exp_ens = np.array([2.15,3.56,4.19,5.2,5.68,6.36])
nu_ens_23=np.array([0.32645,0.89,1.1297,1.6596,2.021,2.667])
nu_ens_23_scaled_50=np.array([2.1449,5.035,5.75,6.871,6.91,7.4])
nu_ens_23_scaled_25=np.array([1.5561,3.8793,4.6089,6.032,6.5821,7.2732])
nu_ens_pw=np.array([0.719,1.9252,2.3825,3.4,4.0323,5.12])
plt.figure(4)
#plt.plot(ps,exp_ens,'bx',ps,nu_ens_23,'rx',ps,nu_ens_23_scaled,'kx')
#plt.plot(ps,nu_ens_pw,'gx')
plt.plot(ps,exp_ens,'bx',label='Experiment')
plt.plot(ps,nu_ens_23,'rx',label='Numerical')
plt.legend(loc='best',borderaxespad=1, frameon=True,fontsize=12,shadow=True)
plt.xticks(fontsize=16)
plt.yticks(fontsize=16)
plt.minorticks_on()
plt.grid(ls='--')
plt.xlabel('Acetylene gas pressure (torr)',fontsize= 12,fontweight= 'bold')

plt.ylabel(r'Absorbed energy only by gas ( $\mu\text{J}$ )',fontsize= 12,fontweight= 'bold')
#plt.xlabel('pressure (torr)')
#plt.ylabel('absorbed energy (uJ)')
plt.grid(True)
plt.xlim(0,15)
plt.ylim(0,7)

plt.figure(10)
plt.plot(z,a1*Pz)

```

B.4 Python code to calculate phase matching angles for KTP crystal

```
# -*- coding: utf-8 -*-
"""
Created on Wed Jun 27 12:47:53 2018
This is written to calculate the phase matching angle of KTP crystal and calculate t
the deff of KTP for OPA operation of 1064-1532= 3483

references

(1)Handbook of nonlinear optics by sutherkand (2nd edition)
(2)http://eksmaoptics.com/out/media/Crystals%202013%20EUR.pdf

@author: kweera
"""
import numpy as np
from matplotlib import pyplot as plt

ls=1.532 # signal wavelength in um
lp=1.064 # pump wavelength in um

ld=lp*ls/(ls-lp)
#wavelength dependent refractive indices from ref (2)

def refnx(l):
    nx = np.sqrt (3.0067 + 0.0395 / (l**2 - 0.044251) - (0.01247*l**2))
    return nx
def refny(l):
    ny = np.sqrt (3.0319 + 0.04152 / (l**2 - 0.04586) - (0.01337*l**2))
    return ny
def refnz(l):
    nz = np.sqrt (3.3134 + 0.05694 / (l**2 - 0.05941) - (0.016713*l**2))
    return nz

# calculatng phase matching angle look table 16 of ref 1 at page 68
# propagation plane XZ

A= refnx(ld)/ld # A= nd;x / ld
B= refny(ls)/ls # B = np2;y/lp2
C= refny(lp)/lp # C= np1;y/lp1
E= refnz(ls)/ls # E= np2;z/lp2

V= B**2 / (C-A)**2

Y = (B/E)**2

tan_theta_2 = (1-V)/(V-Y)

tan_theta=np.sqrt (tan_theta_2)
```

```

theta_radi = np.arctan (tan_theta) # angle in radians
theta_degree= theta_radi * 180 / np.pi #angle in degree
print 'phase matching angle =%0.3f degrees'% theta_degree

#
# calculating deff
# since nx < ny < nz Sin omega = nZ/nY ( (nY^2 - nX^2) / (nZ^2 - nX^2) ) ^ (1/2) from page
61 of ref 1
# calculating annle delta # cot 2delta = (cot^2 omega sin^ theta - cos ^ theta cos ^ phi +
sin^ phi) / cos theta sin 2 phi
phi = 0 # since propagation is in XZ plane

#finding omega
sin_omega = (refnz(ls)/refny(ls)) * np.sqrt ((refny(ls)**2 - refnx(ls)**2) / ( refnz(ls)**2
- refnx(ls)**2) )
omega= np.arcsin(sin_omega)
cot_2delta = (((1/np.tan(omega)**2) *np.sin(theta_radi)**2) - (np.cos(theta_radi)**2 * np.c
os(phi)**2) + np.sin(phi)**2) / (np.cos(2*theta_radi)*np.sin(2*phi))

tan_2delta = 1/cot_2delta

two_delta = np.arctan(tan_2delta)
delta= two_delta/2

print 'delta =%0.3f radians'% delta
#
# calcul;ting deff
# these d values are from ref 2 and in pm/V
d32 = 3.9
d31 = 1.95
d33 = 15.3

# I split the deff equation in to three parts in order to make it easy
# equation for deff can be found in table 21 in page 73 of ref 1
# use type ii phase matching for mm2 crystal class

deff1 = (d32-d31)* (3*np.cos(delta)**2 -
1) * (np.sin(theta_radi)*np.cos(theta_radi)*np.sin(2*phi)*np.sin(delta))
deff2 = -
3* (d31*np.sin(phi)**2 + d32 * np.cos(phi)**2) * (np.sin(theta_radi)*np.cos(theta_radi)**2
* np.sin(delta)**2 *np.cos(delta))
deff3 = - (d31*np.sin(phi)**2 + d32*np.cos(phi)**2)* (np.sin(theta_radi)*np.cos(delta)*(3*n
p.cos(delta)**2 - 2)) - d33 * np.sin(theta_radi)**3 *np.sin(delta)**2 * np.cos(delta)

deff= deff1 + deff2 + deff3

print 'deff =%0.3f pm/V'% deff

```

Appendix C - Copyright permissions

C.1 From The Optical Society

Dear Kushan Weerasinghe,

Thank you for contacting The Optical Society.

For the use of figure 1 from F. Couny, F. Benabid, and P. S. Light, "Large-pitch kagome-structured hollow-core photonic crystal fiber," Opt. Lett. 31, 3574-3576 (2006):

OSA considers your requested use of its copyrighted material to be Fair Use under United States Copyright Law. It is requested that a complete citation of the original material be included in any publication.

While your publisher should be able to provide additional guidance, OSA prefers the below citation formats:

For citations in figure captions:

[Reprinted/Adapted] with permission from ref [x], [Publisher]. (with full citation in reference list)

For images without captions:

Journal Vol. #, first page (year published) An example: Opt. Lett. 31, 3574 (2006)

Please let me know if you have any questions.

Kind Regards,

Rebecca Robinson

Rebecca Robinson

February 20, 2019

Authorized Agent, The Optical Society

The Optical Society (OSA)

2010 Massachusetts Ave., NW

Washington, DC 20036 USA

www.osa.org

Reflecting a Century of Innovation

Dear H W Kushan M Weerasinghe,

Thank you for contacting The Optical Society.

For the use of figure 4 from Jes Henningsen, Jan Hald, and Jan C. Petersen, "Saturated absorption in acetylene and hydrogen cyanide in hollow-core photonic bandgap fibers," Opt. Express 13, 10475-10482 (2005):

OSA considers your requested use of its copyrighted material to be Fair Use under United States Copyright Law. It is requested that a complete citation of the original material be included in any publication.

While your publisher should be able to provide additional guidance, OSA prefers the below citation formats:

For citations in figure captions:

[Reprinted/Adapted] with permission from ref [x], [Publisher]. (with full citation in reference list)

For images without captions:

Journal Vol. #, first page (year published) An example: , " Opt. Express 13, 10475 (2005)

Please let me know if you have any questions.

Kind Regards,

Rebecca Robinson

Rebecca Robinson

January 14, 2019

Authorized Agent, The Optical Society

The Optical Society (OSA)
2010 Massachusetts Ave., NW
Washington, DC 20036 USA
www.osa.org

Reflecting a Century of Innovation

Dear Kushan Weerasinghe,

Thank you for contacting The Optical Society.

For the use of figure 2 from [1] Zefeng Wang, Walter Belardi, Fei Yu, William J. Wadsworth, and Jonathan C. Knight, "Efficient diode-pumped mid-infrared emission from acetylene-filled hollow-core fiber," *Opt. Express* 22, 21872-21878 (2014):

OSA considers your requested use of its copyrighted material to be Fair Use under United States Copyright Law. It is requested that a complete citation of the original material be included in any publication.

For the use of figure 2 from [2] Muhammad Rosdi Abu Hassan, Fei Yu, William J. Wadsworth, and Jonathan C. Knight, "Cavity-based mid-IR fiber gas laser pumped by a diode laser," *Optica* 3, 218-221 (2016):

This article is published by The Optical Society under the terms of the Creative Commons Attribution 4.0 License. Further distribution of this work must maintain attribution to the author(s) and the published article's title, journal citation, and DOI.

While your publisher should be able to provide additional guidance, OSA prefers the below citation formats:

For citations in figure captions:

[Reprinted/Adapted] with permission from ref [x], [Publisher]. (with full citation in reference list)

For images without captions:

Journal Vol. #, first page (year published) An example: *Opt. Express* 22, 21872 (2014)

Please let me know if you have any questions.

Kind Regards,

Rebecca Robinson

Rebecca Robinson

March 26, 2019

Authorized Agent, The Optical Society

The Optical Society (OSA)
2010 Massachusetts Ave., NW
Washington, DC 20036 USA
www.osa.org

C.2 From the AAAS

THE AMERICAN ASSOCIATION FOR THE ADVANCEMENT OF SCIENCE LICENSE

TERMS AND CONDITIONS

Mar 22, 2019

This Agreement between Kansas State University -- H W Kushan Weerasinghe ("You") and The American Association for the Advancement of Science ("The American Association for the Advancement of Science") consists of your license details and the terms and conditions provided by The American Association for the Advancement of Science and Copyright Clearance Center.

License Number	4523440507023
License date	Feb 07, 2019
Licensed Content Publisher	The American Association for the Advancement of Science
Licensed Content Publication	Science
Licensed Content Title	Single-Mode Photonic Band Gap Guidance of Light in Air
Licensed Content Author	R. F. Cregan,B. J. Mangan,J. C. Knight,T. A. Birks,P. St. J. Russell,P. J. Roberts,D. C. Allan
Licensed Content Date	Sep 3, 1999
Licensed Content Volume	285
Licensed Content Issue	5433
Volume number	285
Issue number	5433
Type of Use	Thesis / Dissertation
Requestor type	Scientist/individual at a research institution
Format	Electronic
Portion	Text Excerpt
Number of pages requested	1
Order reference number	
Title of your thesis / dissertation	Power scaling an acetylene filled hollow-core optical fiber gas laser
Expected completion date	May 2019
Estimated size(pages)	120
Requestor Location	Kansas State University 2050 Jardine Dr Apt 04 MANHATTAN, KS 66502

	United States
	Attn: Kansas State University
Billing Type	Invoice
	Kansas State University
	2050 Jardine Dr
	Apt 04
Billing Address	
	MANHATTAN, KS 66502
	United States
	Attn: Kansas State University
Total	0.00 USD

C.3 From the SPIE

Dear Mr. Weerasinghe,

Thank you for seeking permission from SPIE to reprint material from our publications. SPIE shares the copyright with you, so as author you retain the right to reproduce your paper in part or in whole.

Publisher's permission is hereby granted under the following conditions:

- (1) the material to be used has appeared in our publication without credit or acknowledgment to another source; and
- (2) you credit the original SPIE publication. Include the authors' names, title of paper, volume title, SPIE volume number, and year of publication in your credit statement.

Best,
Katie Sinclair
Editorial Assistant, Publications
SPIE
+1 360 685 5436
katies@spie.org

SPIE is the international society for optics and photonics
<http://SPIE.org>

-----Original Message-----

From: Weerasinghe, Kushan <kweera@phys.ksu.edu>
Sent: Wednesday, February 6, 2019 10:34 PM
To: reprint_permission <reprint_permission@spie.org>
Subject: Reprint permission

Hello,

I am writing my Ph.D. thesis and would like to use the contents of the following article. However, I am the first author of the following article and I am going to discuss the contents in detail in my thesis. Could you please grant me permission to use it?
"Toward power scaling in an acetylene mid-infrared hollow-core optical fiber gas laser: effects of pressure, fiber length, and pump power" H W Kushan Weerasinghe. Proc. SPIE 10512, Fiber Lasers XV: Technology and Systems, 105121O (26 February 2018)

And the content of the above article will be used in my Ph.D. thesis titled "Power scaling an acetylene mid-infrared hollow-core optical fiber gas laser".

Thank you,

H W Kushan Weerasinghe.